Summer 2019

Computational Analysis and Design Optimization of Convective PCR Devices

Jung Il Shu
Old Dominion University, jshu004@yahoo.com

COMPUTATIONAL ANALYSIS

AND DESIGN OPTIMIZATION OF CONVECTIVE PCR DEVICES

by

Jung Il Shu
B.S.A.E. February 2011, Inha University, South Korea
M.S.A.E. February 2014, Konkuk University, South Korea

A Dissertation Submitted to the Faculty of
Old Dominion University in Partial Fulfillment of the
Requirements for the Degree of

DOCTOR OF PHILOSOPHY IN ENGINEERING

AEROSPACE ENGINEERING

OLD DOMINION UNIVERSITY
August 2019

Approved by:

Oktay Baysal (Director)

Shizhi Qian (Member)

Miltos Kotinis (Member)

Richard Gregory (Member)

(This page is intentionally left blank)

ABSTRACT

COMPUTATIONAL ANALYSIS
AND DESIGN OPTIMIZATION OF CONVECTIVE PCR DEVICES

Jung Il Shu
Old Dominion University, 2019
Director: Dr. Oktay Baysal

Polymerase Chain Reaction (PCR) is a relatively novel technique to amplify a few copies of DNA to a detectable level. PCR has already become common in biomedical research, criminal forensics, molecular archaeology, and so on. Many have attempted to develop PCR devices in numerous types for the purpose of the lab-on-chip (LOC) or point-of-care (POC). To use PCR devices for POC lab testing, the price must be lower, and the performance should be comparable to the lab devices. For current practices with the existing methods, the price is pushed up higher partially due to too much dependence on numerous developmental experiments. Our proposition herein is that the computational methods can make it possible to design the device at lower cost and less time, and even improved performance.

In the present dissertation, a convective PCR, that is the required flow circulation is driven by the buoyancy forces, is researched towards the use in POC testing. Computational Fluid Dynamics (CFD) is employed to solve the nonlinear equations for the conjugate momentum and heat transfer model and the species transport model. The first application of the models considers four reactors in contact with two separate heaters, but with different heights. Computational analyses are carried out to study the nature of buoyancy-driven flow for DNA amplification and the effect of the capillary heights on the performance. The reactor performance is quantified by the doubling time of DNA and the results are experimentally verified. The second application includes a novel design wherein a reactor is heated up by a

single heater. A process is established for low-developmental cost and high-performance design. The best is searched for and found by evaluating the performance for all possible candidates. The third application focuses on the analysis of the performance of single-heater reactors affected by positions of a capillary tube: (1) horizontal, and (2) vertical. In the last application, numerous double-heater reactor designs are considered to find the one that assure the optimal performance. Artificial Neural Network (ANN) is employed to approximate the CFD results for optimization.

In summary, through the four segments of our studies, the results show significant possibilities of increasing the performance and reducing the developmental cost and time. It is also demonstrated that the proposed methodology is advantageous for the development of cPCR reactors for the purpose of POC applications.

(This page is intentionally left blank)

This dissertation is dedicated to:

those who are interested in, want to learn, and need to research this topic

(This page is intentionally left blank)

ACKNOWLEDGEMENTS

I would like to express the deepest appreciation to my advisor, Dr. Oktay Baysal, who has given me consistent support, knowledge, and advice on my research. He has inspired me to be a highly motivated scientist with enthusiasm. His meaningful assistance and tireless guideline have helped me concentrate solely on the research.

I would like to thank my co-advisor, Dr. Shizhi Qian, for his advice on the Biomechanical/Medical research. He has led me to the new research fields and given me a thousand bits of help in reviewing my research topics and papers.

I am pleased to have collaborated with Dr. Xianbo Qiu and have a research paper published together. I would like to thank him for giving me permission to cite his research data in my dissertation as well.

I would like to thank the committee members, Drs. Miltos Kotinis and Richard Gregory, for contributing their time and expertise to writing the strong dissertation.

It was a great opportunity for me to collaborate with Varun for Neural Network. Thank you to my colleagues/friends, Omur and Jinhyuk for being good competitors that have motivated me to work/study/research hard.

(This page is intentionally left blank)

NOMENCLATURE

Acronyms

aDNA	Annealed DNA
ANN	Artificial Neural Network
BioMEMS	Bio-Micro-Electro-Mechanical System
CCD	Charged Coupled Device
CFD	Computational Fluid Dynamics
CF-PCR	Continous Flow Polymerase Chain Reaction
cPCR	Convective Polymerase Chain Reaction
dsDNA	Double-Stranded DNA
DOE	Design-of-Experiments
GA	Genetic Algorithm
LAMP	Loop Mediated Isothermal Amplification
LOC	Lab-On-a-Chip
MSE	Mean Square Error
NC	Negative Control
PCR	Polymerase Chain Reaction
PMMA	Polymethylemethacrylate
POC	Point-of-Care
QP	Quadratic Programming
RFU	Relative Fluouscence Unit
SQP	Sequential Quadratic Programming
ssDNA	Single-Stranded DNA

Greek Symbols

α	Thermal Diffusivity, m^2/s; Search Length
β	Thermal Expansion Coefficient, K^{-1}
κ	Thermal Conductivity, $W/(m{\cdot}K)$
$\boldsymbol{\lambda}$	Vector of Multipliers
λ	Lagrange Multipliers
μ	Dynamic Viscosity of a Fluid, $Pa{\cdot}s$
ν	Kinematic Viscosity, m^2/s
ρ	Fluid Density, kg/m^3
σ	Standard Deviation for Temperature, K

Alphabets

AR	Aspect Ratio (a ratio of height to diameter)
b	Bias
C_p	Isobaric Specific Heat, $J/(kg{\cdot}K)$
c	Species Concentrations
D	Diffusive Coefficient, m^2/s
$\mathbf{d}$	Vector of search direction
d	Diameter, mm
$f(\mathbf{x})$	Spatial Mapping Reaction Intensities; Objective Function
$\boldsymbol{\nabla} f(\mathbf{x})$	Gradient of Objective Function
$G(\mathbf{x})$	Constraint Function
$\boldsymbol{\nabla} G(\mathbf{x})$	Gradient of Constraint Function, Jacobian of Constraints Function (if it is a vector)
$\mathbf{g}$	Gravitational Acceleration Vector, m/s^2

g	Gravitational Acceleration, m/s^2
$\mathbf{H}$	Hessian Matrix of Lagrangian Function
h	Characteristic Length, m
$h_{\mathrm{rt,b}}$	Bottom Heater Height, %
$h_{\mathrm{rt,t}}$	Top Heater Height, %
k	Rate Constant, s
$L(\mathbf{x}, \boldsymbol{\lambda})$	Lagrangian Function
$\boldsymbol{\nabla} L(\mathbf{x}, \boldsymbol{\lambda})$	Gradient of Lagrangian Function
Nu	Nusselt Number
$\hat{\mathbf{n}}$	Normal Unit Vector
n	Number of DNAs
p	Flow Pressure, Pa; Vector of Inputs
Ra	Rayleigh Number
S	Surface Area, m^2
T	Temperature, K
t_d	DNA Doubling Time, s
$\mathbf{u}$	Fluid Velocity Vector, m/s
w	Weighted Value
$\mathbf{x}$	Spatial Vector, m; Vector of Design Variables
z_{cr}	Certain point along the z-direction, m

Subscripts

a	Annealing Process; Annealed DNA
avr	Average

d	Denaturation Process
ds	Double-Stranded DNA
e	Extension Process
f	Fluid
i	DNA Species Concentrations; PCR Thermal Cycling Process; i-th Constraint
ini	Initial
k	k-th Iteration
s	Solid

TABLE OF CONTENTS

Page

LIST OF TABLES

(This page is intentionally left blank)

LIST OF FIGURES

Figure Page

CHAPTER 1

INTRODUCTION

1.1 Background

The public has been getting more concerned about health care and taking benefits from technical innovation in relevant fields. Biomedical devices have been becoming more diminished in size and compact to enhance the device portability for lab-on-a-chip (LOC) or point-of-care (POC), a system which performs in vitro analysis by unskilled personnel near the patient with rapid answers and low cost [1, 3-5]. Individuals could examine his or her body conditions or be diagnosed anywhere by medical doctors, and low- and middle-income countries could aggrandize the national health on a low budget as well [6-8]. The public could enjoy better health and longer life than before, and thus, the market growth is burgeoning with a demand for higher-performing and lower-priced biomedical devices [7, 8].

Polymerase Chain Reaction, a technique that enables a few copies of DNA/RNA to be amplified up to detectable level, is the one having been developing in various ways to satisfy the needs [1, 2]. The use of PCR has already become common in numerous and diverse fields, such as biomedical research, criminal forensics, and molecular archaeology [9]. The representative application is expanded to intensive research which identifies a small amount of bacterial/viral DNA/RNA, diagnosis and monitoring of hereditary diseases, and DNA profiling for forensic science and parentage tests. Due to the growing number of applications and advances in development, it has been considered indispensable for studies of gene patterns and organisms since it enables DNA cloning and analysis to be faster, simpler, and more flexible [10, 11].

Many scientists and researchers have been attempting to develop PCR devices in numerous types for the purpose of LOC or POC owing to its expanding utilization and social needs. There are three different representatives: (1) Continuous flow polymerase chain reactor (CF-PCR) is a bio-micro-electro-mechanical system (BioMEMS) device for an ultra-fast DNA amplification using repeated thermal cycling [12]. DNA cocktail is pumped through the constant temperature zones, and it reaches thermal equilibrium with the channel walls quickly due to its low thermal capacitance [13]. However, a high manufacturing cost is required on account of its complexity and the use of MEMS technology [1, 14]. (2) Loop-mediated isothermal amplification (LAMP) is a DNA amplification technique, carrying out at a constant temperature; a thermal cycler is unnecessary [1, 14]. It features reaction simplicity and higher amplification efficiency [1, 14]. Nevertheless, it may produce false-positive with high frequency [1, 14]. (3) Convective-PCR (cPCR) is a DNA amplification technique using flow convection driven by a buoyancy force [15, 16]. Most cPCR reactors are equipped with two heating system, one on the top and the other on the bottom, and a temperature control system for stability. An external force is not required to drive the fluid through the different temperature zones; the temperature transferring speed is very fast [14]. It could be developed at a lower cost than any others on account of its simplicity in design and mechanism, and thus, has a great potential to be more popular.

Although some PCR devices are very successful as LOC applications, researchers and engineers have a long way to go before achieving them as a POC device [11]. The size, performance, cost, and difficulty of operating the device are the prerequisite of medical devices as POC applications [8]. A systematic design approach is required; computational methods are the one which has the potential to meet the matters as aforementioned [17, 18].

Computational fluid dynamics (CFD) belongs to the computational methods used for analysis or design for PCR reactors. Krishnan et al. (2002), and Chen et al. (2004) adopted CFD and provided an insight into flow convection inside the capillaries [19, 20]. Li et al. (2016) used CFD to investigate the flow attributes varying depending on various capillary geometries [14]. Qui et al. (2019) analyzed the flow conditions inside the PCR reactor in the vertical and horizontal positions [2]. Dissimilar to the research as aforementioned, Yariv et al. (2005) applied the convection-diffusion-reaction equation to a very simple nondimensional geometry, solving for DNA concentrations, and presenting the potential of the computational method to be used for the performance evaluation of cPCR reactors [21]. Allen et al. (2009), Muddu et al. (2011), and Shu et al. (2019) improved Yariv's mathematical model and applied it to more practical problems for DNA amplification [1, 22, 23].

1.2 Principles of DNA amplification

As of now, various techniques have been revolutionized for DNA amplification. PCR is the most common technique utilized for DNA amplification in molecular biology. It amplifies copies of DNAs by altering the sequence of individual DNA fragments [9]. Most PCR techniques depend on thermal cycling processes.

As shown in Fig. 1, the standard PCR thermal cycler includes repetitive three distinctive reactions processes, such as denaturation (95-97 °C), annealing (50-60 °C), and extension (72-77 °C) [24, 25]. In the denaturation step, the double-stranded DNA (dsDNA) is separated into two single-stranded (ssDNA) due to the high temperature [26]. The annealing step enables the primers to stay cooled and bind them to the ends of the ssDNA [1, 9]. In the extension step, the annealed DNA (aDNA) is heated to 72-77 °C at which the polymerase enzyme (e.g., Taq polymerase) boosts the DNA synthesis at most; then, new two dsDNAs are created from the

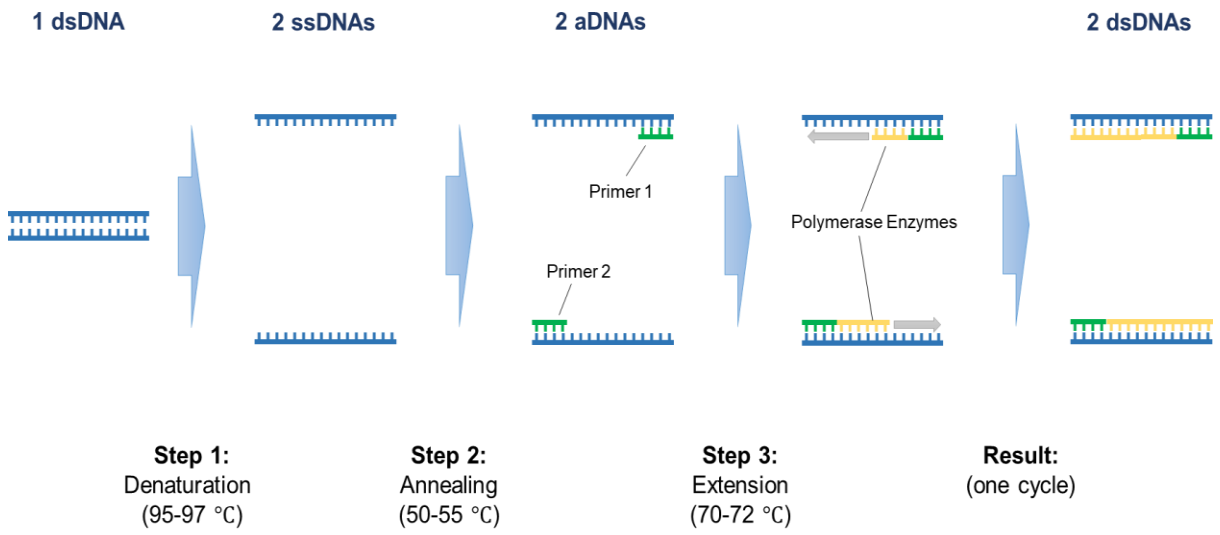

Fig. 1. Thermal cycling processes for DNA amplification

aDNA [1, 9]. As a result of the repetitive thermal process, numerous copies of DNA templates are produced at an exponential growth rate by repeating the processes.

1.3 DNA Detection and Quantification

The number of copies of DNAs gets doubled whenever the cycle is repeated. Specific methods are utilized to detect the increasing number of DNAs. One of the representative methods in experimentations is the utilization of fluorescent light. A substance marked with a fluorophore is added to PCR reagents in a reactor, binding to all dsDNAs [27]. Sensors are used to measure the fluorescence of the fluorophore; the substance is excited at the specific range of wavelength by the fluorescent light emitted from the external source [28]. This method enables to detect dsDNAs amplified at every cycle.

The magnitude of fluorescence can be monitored using electrophoresis techniques to demonstrate the result of the amplified DNAs. A charged coupled device (CCD) array is placed away from a capillary tube, detecting the fluorescence signal when the labeled DNA fragments

of the solutions in the capillary tube are energized by laser light [29]. Then, a computer reads the signal and displays the quantity or size of the DNA fragments from the level of fluorescence intensity [28, 29]. Based on this process, the reaction intensity can be plotted, as shown in Fig. 2. In the graph, the relative fluorescence unit (RFU), which is a unit of measurement used for fluorescence detection, is related to the strength of DNA amplification. The region of the DNA amplification curve can be categorized by a growth rate as four different phases: (1) linear-ground, (2) exponential, (3) log-linear, and (4) plateau [30]. The linear-ground is the earliest phase of the amplification; the strength of the fluorescence intensity is almost constant since the number of DNAs is not sufficient to make the fluorescence signal jump over a critical number required for measurement. Once the strength of the fluorescence signal is larger than a critical number, the fluorescence intensity increases at an exponential growth rate. In the log-linear

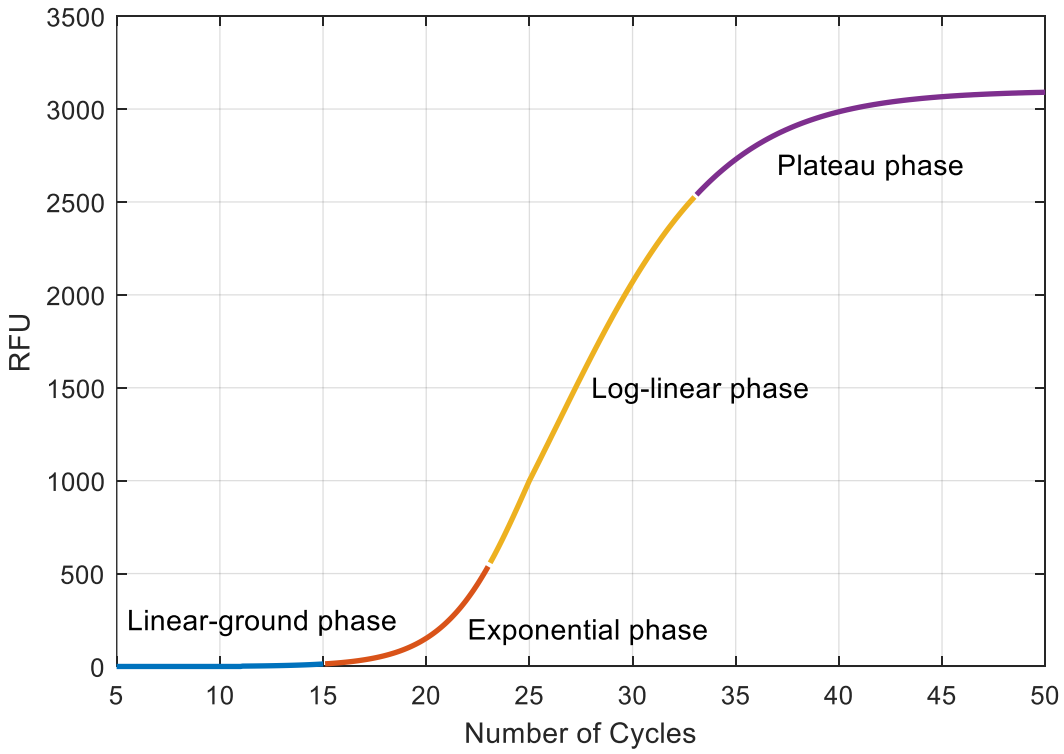

Fig. 2. Example of curves for relative fluorescence unit versus the number of cycles

phase, the signal is directly proportional to the increase of DNAs through the PCR amplification [31]. Finally, the strength of amplification significantly decreases and stops in the plateau phase [32, 33]. No more DNAs are amplified at all in this phase since the primers to be used for the amplification are not in the infinite amount.

1.4 Scope and Outlines

This study aims to establish computational methods for the development of portable, cost-effective, rapid cPCR reactors so that people can take advantages of POC in normal life. Design methodologies are introduced in an aspect of POC, and multiple types of cPCR reactors are covered: (1) reactors with double-heating plates in both-end; (2) reactors with a one-end single-heater; (3) reactors with double heaters in both-end. In Chapter 1, the research background is introduced to explain the concept of POC, the reason for study, the principle of DNA amplification, and DNA detection and quantification. In Chapter 2, we introduce mathematical models that render natural convection and DNA species transport. The verification of the mathematical models is carried out in the computational and experimental ways. Chapter 3 describes the application of the mathematical models to the first reactor type as aforementioned. It shows how to quantify the performance of the first reactor type using a computational method. Chapter 4 deals with the design methodology for the second reactor type toward POC applications. It gives the best design for a single-heater reactor that satisfies the use of POC. In Chapter 5, analysis is conducted for the second-typed reactor operated in a horizontally lied position. It proves the possibility of the operation of cPCR devices in an unusual position using both computational and experimental methods. In Chapter 6, the third typed reactors are optimally designed using Artificial Neural Network (ANN). The performance

of numerous reactor designs is estimated using CFD simulations and used to train neural networks based on the process established for the development of surrogate models. The optimal size of reactors is determined using the hybrid algorithm combined with the genetic algorithm and the sequential quadratic programming. In Chapter 7, conclusions are made for the proposed methodologies in the aspect of POC utilization, and future work is suggested to improve the solutions near future. In Appendices, we attach the codes and data used for the studies. Appendix A presents C++ codes for the user-defined CFD solver that uses OpenFOAM libraries. In Appendix B, we include the contour plots of the velocity and temperature fields of all possible reactor designs, which is covered in Chapter 4. In Appendix C, the performance of the numerous reactor designs (Chapter 6) is listed in Tables. Lastly, we attach the MATLAB codes used for network training, which is covered in Chapter 6.

(This page is intentionally left blank)

CHAPTER 2

MATHEMATICAL MODELING

2.1 Overview

DNA amplification can be mimicked using computational methods. The first step of the modeling is to simplify the problem by assuming attributes. The fluid in a capillary is assumed to be pure water as Newtonian, incompressible, and laminar since Li et al. (2016) utilized PCR reagents as distilled water basis [14]. It is assumed that the material of a capillary is polymethylmethacrylate (PMMA). PMMA is good for diathermancy and surface smoothness, and hence, it is beneficial for flow to be laminar [1, 14].

The mathematical models can be considered in an aspect of a heat transfer problem as well. High temperature is applied by resistive heaters (i.e., heat sources). Then, heat transfer occurs in two different forms: (1) thermal conduction between the heaters and the capillary, (2) flow convection inside the capillary. Conduction enables heat to spread from the heat source to the entire region. It provokes the heat transfer from the capillary to the fluid, resulting in buoyancy-driven flow convection due to the density variation, which depends on temperature [16]. This is a type of Rayleigh-Bénard convection problems and a pre-requisite for the effective DNA amplification via the convective PCR.

Once a flow convection loop is made and the appropriate temperature is formed over the entire capillary, the kinetic model of the DNA amplification should be considered in the aspect of molecules, which is the Lagrangian approach [22]. However, the description of the motion of DNA molecules is very complicated and difficult to solve it. For this reason, the Eulerian approach could be the best option since molecules are described as species concentrations [22].

Based on the principles, two different mathematical models are developed: (1) steady-state conjugate momentum heat transfer, and (2) transient species transport. The conjugate momentum heat transfer solves the steady-state continuity, momentum (Navier-Stokes), and energy equations. After the solution is converged, the velocity and temperature fields of the fluid domains are obtained and used for the transient species transport equations. The second mathematical model is also known as convection-diffusion-reaction equations. It describes how molecules are transferred inside a system by convection, diffusion, and reaction. The variation of DNA concentrations can be tracked over time by adopting the transient species transport model; it enables to compute the DNA doubling time.

2.2 Conjugate Momentum and Heat Transfer Model (Phase I)

The steady-state conjugate momentum and heat transfer model is developed to investigate flow convection due to heat transfer. Eqs. (1) to (3) are the continuity, momentum, and energy equations, respectively, and they are adapted to solve for the fluid domains [1, 2, 34, 35].

$$\boldsymbol{\nabla} \cdot (\rho \mathbf{u}) = 0 \tag{1}$$

$$\rho(\mathbf{u} \cdot \boldsymbol{\nabla})\mathbf{u} = -\boldsymbol{\nabla} p + \rho \mathbf{g} + \mu \boldsymbol{\nabla}^2 \mathbf{u} \tag{2}$$

$$\rho C_p \left(\mathbf{u} \cdot \boldsymbol{\nabla} T_f\right) = \boldsymbol{\nabla} \cdot \left(\kappa_f \boldsymbol{\nabla} T_f\right) \tag{3}$$

where, ρ is the fluid density, varying depending upon temperature, $\mathbf{u}$ is the fluid velocity; p denotes the pressure, $\mathbf{g}$ is the gravitational acceleration in a vector form, μ and C_p are the dynamic viscosity and the isobaric specific heat as a function of temperature, respectively; T_f is the fluid temperature, and κ_f denotes the fluid thermal conductivity. The energy equation solves for the temperature of the solid domains, defined as follows [1, 34]:

$$\nabla \cdot (\kappa_s \nabla T_s) = 0 \quad (4)$$

where, κ_s is the solid thermal conductivity as a constant value, and T_s is the solid temperature. Eqs. (1) to (4) are simultaneously solved for the interaction of heat transfer between the fluid and solid domains.

To induce the flow convection using the conjugate momentum and heat transfer model, at least the fluid density should vary depending upon temperature. Boussinesq approximation could be a key solution; however, the thermal properties in the polynomial form are utilized for more accurate solutions. The least-square method is the best for curve-fit of the thermal properties. Çengel et al. (2015) provide the thermal data of pure water, such as density, specific heat, dynamic viscosity, and thermal conductivity; the polynomial coefficients are derived as seen in Table 1 [34, 36]:

TABLE 1

THERMAL PROPERTIES OF PURE WATER AS POLYNOMIAL COEFFICIENTS

Thermal properties	Unit	Polynomial coefficients				
		0^{th}	1^{st}	2^{nd}	3^{rd}	4^{th}
Density	kg/m^3	784.5000	1.6739	-0.0032	0.0000	0.0000
Specific heat	J/(kg K)	2.6551e+04	-256.6939	1.0994	-0.0021	1.5074e-6
Dynamic viscosity	Pa s	0.3393	-0.0038	1.5972e-05	-2.9948e-08	2.1072e-11
Thermal conductivity	W/(m K)	-6.792	0.0070	-8.972e-06	0.0000	0.0000

Note that the thermal properties in Table 1 are only valid when the range of temperature is from 273.15 K to 400 K. The thermal conductivity of PMMA is 0.22 W/(m K) as a constant value since the entire solid domains are dominated by linear heat conduction [1].

Boundary conditions are applied for the solution of the conjugate momentum and heat transfer model as follows:

1) No-slip velocity boundary condition ($\mathbf{u}_{\text{wall}} = 0$) is applied on the inner wall of a capillary (the outer surface of the fluid domains) [37].
2) The temperature boundary condition is applied on the specific outer surface of a capillary where the resistive heater is in contact (the solid domains).
3) The convective heat transfer between a capillary and the ambient air, $\dot{q} = h(T_\infty - T_s)$, may be considered if the reactor is not enclosed by insulators (the solid domains).
4) The temperature boundary condition, $T_f(\mathbf{x}_{interf}) = T_s(\mathbf{x}_{interf})$, is applied to the interfacial area between the solid and fluid domains [34, 38].

The boundary conditions will be covered detail in the next Chapters, which focus on the different cPCR analysis or design topics.

2.3 Species Transport Model (Phase II)

Yariv et al. (2005) introduced a simple kinetic process for DNA amplification in order to track the spatiotemporal evolution of the DNA components as follows [1, 21, 22, 39]:

$$\text{dsDNA} \xrightarrow{\text{denaturation}} 2\ \text{ssDNA} \xrightarrow{\text{annealing}} 2\ \text{aDNA} \xrightarrow{\text{extension}} 2\ \text{dsDNA}$$

This simple mechanism for DNA amplification well describes how a DNA gets doubled in repetitive thermal cycling processes, such as denaturation, annealing, and extension. Yariv et al. (2005) devised a DNA species transport model in the non-dimensional form based on the aforementioned kinetic process and solved for DNA concentrations in view of the Eulerian approach [21].

The transient species transport model is developed in the dimensional form to investigate the DNA species concentrations. Eqs. (5) to (7) are coupled together to delineate the kinetic process as follows [1, 21-23]:

$$\frac{\partial c_{\mathrm{ds}}}{\partial t} + \mathbf{u} \cdot \boldsymbol{\nabla} c_{\mathrm{ds}} = D \boldsymbol{\nabla}^2 c_{\mathrm{ds}} + 2\, k_{\mathrm{d}}\, f_{\mathrm{d}}(\mathbf{x})\, c_{\mathrm{ds}} - k_{\mathrm{a}} f_{\mathrm{a}}(\mathbf{x})\, c_{\mathrm{ss}} \tag{5}$$

$$\frac{\partial c_{\mathrm{ss}}}{\partial t} + \mathbf{u} \cdot \boldsymbol{\nabla} c_{\mathrm{ss}} = D \boldsymbol{\nabla}^2 c_{\mathrm{ss}} + k_{\mathrm{a}}\, f_{\mathrm{a}}(\mathbf{x})\, c_{\mathrm{ss}} - k_{\mathrm{e}} f_{\mathrm{e}}(\mathbf{x})\, c_{\mathrm{a}} \tag{6}$$

$$\frac{\partial c_{\mathrm{a}}}{\partial t} + \mathbf{u} \cdot \boldsymbol{\nabla} c_{\mathrm{a}} = D \boldsymbol{\nabla}^2 c_{\mathrm{a}} + k_{\mathrm{e}}\, f_{\mathrm{e}}(\mathbf{x})\, c_{\mathrm{a}} - k_{d} f_{d}(\mathbf{x})\, c_{\mathrm{ds}} \tag{7}$$

where, c_{ds}, c_{ss}, and c_{a} are the species concentrations of dsDNAs, ssDNAs, and aDNAs, respectively; t is the time, D is the diffusive coefficient; k_{d}, k_{a}, and k_{e} are the reaction rate of the denaturation, annealing, and extension processes, respectively [40]; and f_{d}, f_{a}, and f_{e} are the reaction intensities for the denaturation, annealing, and extension processes, respectively. Note that the flow velocity obtained from the conjugate momentum and heat transfer model is required for the convection terms in the species transport model. The reaction intensities of the denaturation, annealing, and extension processes are mapped with the standard Gaussian function to be coupled with the temperature field obtained from the conjugate momentum and heat transfer model [1, 22].

$$f_{\mathrm{d}}(\mathbf{x}) \sim \exp\left(-\frac{(T - T_{\mathrm{d}})^2}{2\sigma_{\mathrm{d}}^2}\right) \tag{8}$$

$$f_{\mathrm{a}}(\mathbf{x}) \sim \exp\left(-\frac{(T - T_{\mathrm{a}})^2}{2\sigma_{\mathrm{a}}^2}\right) \tag{9}$$

$$f_{\mathrm{e}}(\mathbf{x}) \sim \exp\left(-\frac{(T-T_{\mathrm{e}})^2}{2\sigma_{\mathrm{e}}^2}\right) \tag{10}$$

where, T_{d}, T_{a}, and T_{e} denote ideal reaction temperature for denaturation, annealing, and extension processes, respectively; σ_{d}, σ_{a}, and σ_{e} are the standard deviation for the corresponding processes, respectively. Fig. 3 shows an example of the standard Gaussian functions with the standard deviations of 5, 5, and 5℃ and the ideal reaction temperatures of 95, 72, and 55 ℃. The reaction intensities are proportional to the standard Gaussian function, and their magnitudes can be determined by empirical or experimental methods (e.g., reverse engineering). The higher the reaction intensities are, the stronger the activation of the DNA components gets.

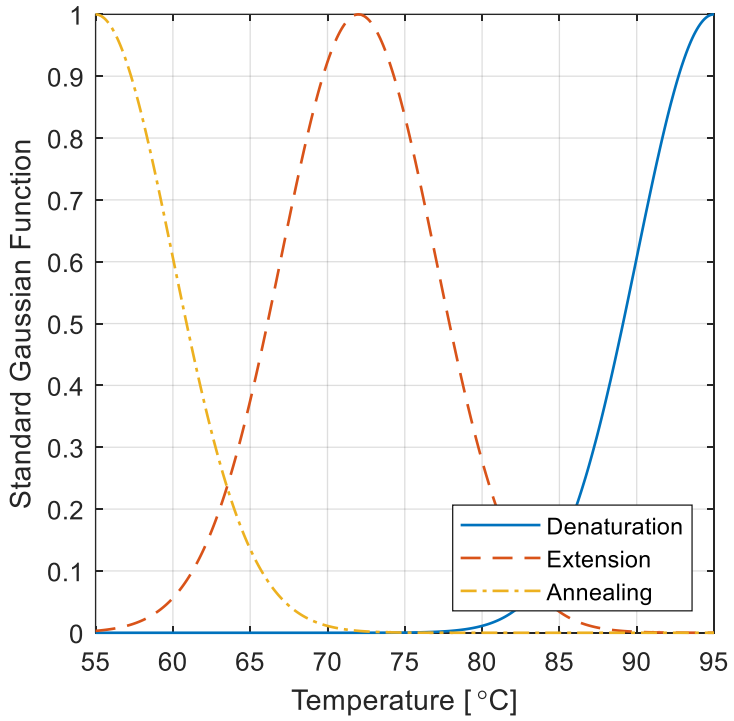

Fig. 3. Example of the standard Gaussian function for reaction intensities of denaturation, extension, and annealing.

The solution of the species transport model can be obtained by providing initial and boundary conditions. The initial conditions correspond to the species concentrations of various DNAs: (1) the concentration of the dsDNA determined by the amount of DNAs, (2) the concentration of the aDNA initially given zero, (3) the concentration of the ssDNA initially given zero. Additionally, the respective DNA species are confined for the impenetrability on the boundary, represented by [1, 21-23]:

$$\hat{\mathbf{n}} \cdot \boldsymbol{\nabla} c_i = 0 \tag{11}$$

where, $\hat{\mathbf{n}}$ denotes the normal unit vector, and c_i is the species concentration of ds-, a-, or ssDNA. The volume-averaged concentration is utilized as the aforementioned initial conditions, especially, for the double-stranded DNA. The equation for the volume-averaged concentration is defined as follows:

$$\bar{c_i} = \left(\int c_i(\mathbf{x})\, d\mathbf{x} \right) / \left(\int d\mathbf{x} \right) \tag{12}$$

Once the solution is obtained, the species transport model computes the number of the respective DNAs if the concentrations are of the number basis. The number of ds-, a-, and ssDNA can be obtained, as seen in Eq (12):

$$n_i = \int c_i(\mathbf{x})\, d\mathbf{x} \tag{13}$$

The species transport model can estimate the performance of a cPCR reactor by the doubling time, Eq (14) [22]:

$$t_d = \frac{\ln 2}{\lim\limits_{t\to\infty} \frac{d}{dt} \ln \int c_{ds}(\mathbf{x}, t)\, d\mathbf{x}} \tag{14}$$

2.4 Verification of Mathematical Models

The standard OpenFOAM CFD code, `chtMultiRegionSimpleFoam` solves the equations of the conjugate momentum and heat transfer model. The classical Rayleigh-Bénard convection problem was solved to verify the first mathematical model. Rossby (1969) produced the experimental data that reveals the relation between the Nusselt and Rayleigh Numbers for pure water as follows [41]:

$$Nu = 0.131\, Ra^{0.3\pm0.005} \tag{15}$$

where, Nu is the Nusselt number, and Ra is the Rayleigh number. Eq. (15) was utilized as a reference for the verification. Note that Eq. (15) is valid only for $Ra > 34{,}000$ [1, 41].

The classical Rayleigh-Bénard convection can be analyzed by applying heat on the top and bottom of fluid. The magnitude of fluid convection depends on the fluid height, the difference of temperature applied on the top and bottom, and so on. It can be alternatively explained with the Rayleigh and Nusselt numbers. The Rayleigh number is a dimensionless number that describes the behavior of fluids with non-uniform density caused by temperature differences, mathematically defined as [16, 34]:

$$Ra = \frac{g\beta}{\nu\alpha}\Delta T h^3 \tag{16}$$

where, g is the gravitational acceleration (scalar), β is the thermal expansion coefficient, ν denotes the kinematic viscosity, α is the thermal diffusivity, ΔT indicates the difference of temperature between the top and bottom surfaces of fluid, and h is the characteristic length.

The Nusselt number is also a nondimensional ratio of convective to conductive heat transfer, describing a characteristic of convective heat transfer on a surface. The surface-averaged Nusselt number is computed using Eq. (17) as follows [34]:

$$\overline{Nu} = \frac{1}{S}\int_S \left(\frac{\left.\frac{\partial\left(T_s - T_f\right)}{\partial \hat{\mathbf{n}}}\right|_{n=0}}{\frac{(T_s - T_\infty)}{L}} \right) dS \tag{17}$$

where, S is the surface area, T_∞ is the ambient air, and L denotes the representative length.

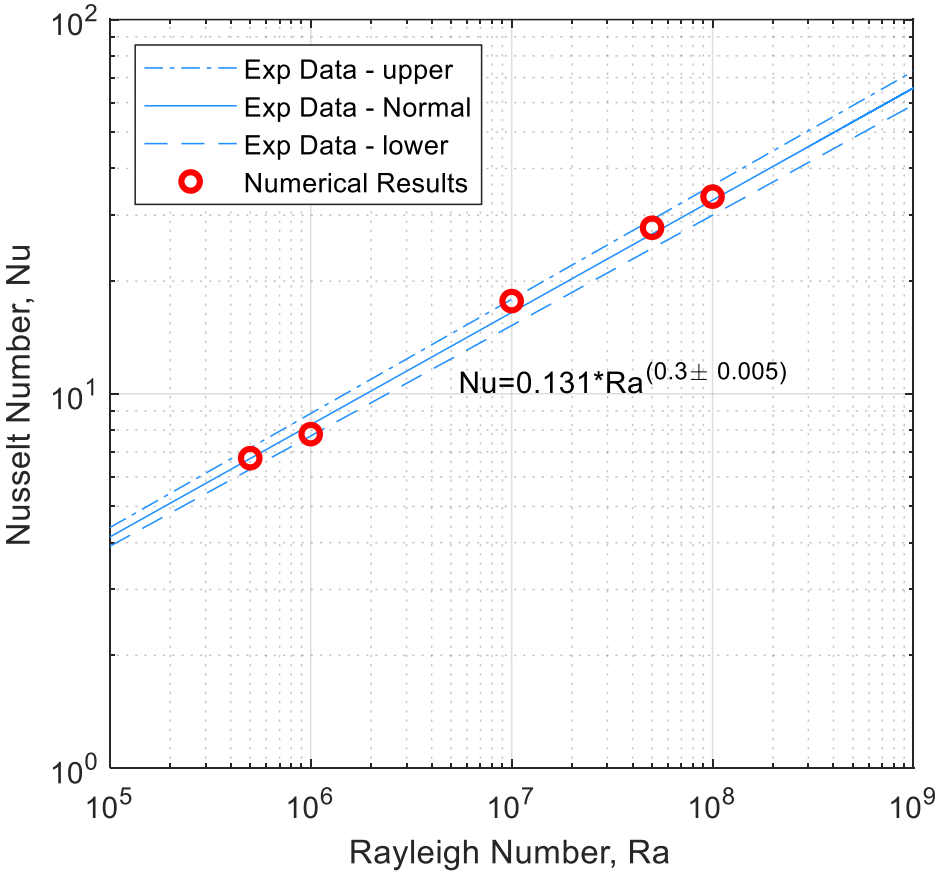

Fig. 4. Nusselt number vs Rayleigh number with five design points for the verification of the conjugate momentum and heat transfer model [1]

Hexahedral-shaped computational domains were created to compare the results with the one in Eq (15). Five design points were considered with target Rayleigh numbers: (1) Ra = 5e+5, (2) Ra = 1e+6, (3) Ra = 1e+7, (4) Ra = 5e+7, and (5) Ra = 1e+8. The characteristic length of the domains and the applied temperature were determined based on the target Rayleigh numbers as aforementioned. The surface-averaged Nusselt numbers were computed at those points using Eq. (17), and the results were obtained, as shown in Fig. 4. All five design points were in the range of the upper and lower limits of the feasible experimental region and showed in a good agreement with the experimental data (Rossby, 1969) [1, 41].

The species transport model was developed based on the OpenFOAM CFD libraries, named `convDiffFoam`. It was verified by comparing CFD data with experimental data of a single heater cPCR. The dimensions of a capillary tube used for the experiment were determined as 1.7 mm of the inner diameter, 17.7 mm of inner height, and 3.1 mm of outer diameter. The capillary tube was in contact with a height-adjustable resistive heater. Three cases for verification were considered as presented in Table 2:

TABLE 2

DIMENSIONS OF A CAPILLARY TUBE WITH A HEATER FOR VERIFICATION

Thermal properties	Unit	Case 1	Case 2	Case 3
Inner diameter	mm	1.7	1.7	1.7
Inner height	mm	17.7	17.7	17.7
Outer diameter	mm	3.1	3.1	3.1
Heater height	mm	2.76	4.40	7.36

It was considered the verification would be successful if the computational results were well-coordinated with the experimentation for all the three cases. The CFD simulation was also implemented to compare the results with the experimentations. As the first phase of analysis, the conjugate momentum and heat transfer model was solved. The boundary conditions in Chapter 2.2 were applied; especially, the constant temperature was considered to be 95 ℃ on the surface where the heater was in contact, and the convective heat transfer coefficient was assigned to be 10 $W/(m^2K)$ [36]. Fig. 5 shows the results of the three verification cases as the solutions of the conjugate momentum and heat transfer model. It was revealed that the velocity and temperature fields were affected by the height of the heater, and hence, the performance would differ from case to case. In the second phase of analysis, the species transport model was solved. The initial/boundary conditions were adopted as described in Chapter 2.3; especially, the initial condition of the concentration for the dsDNA was determined to be 100 as the number-base

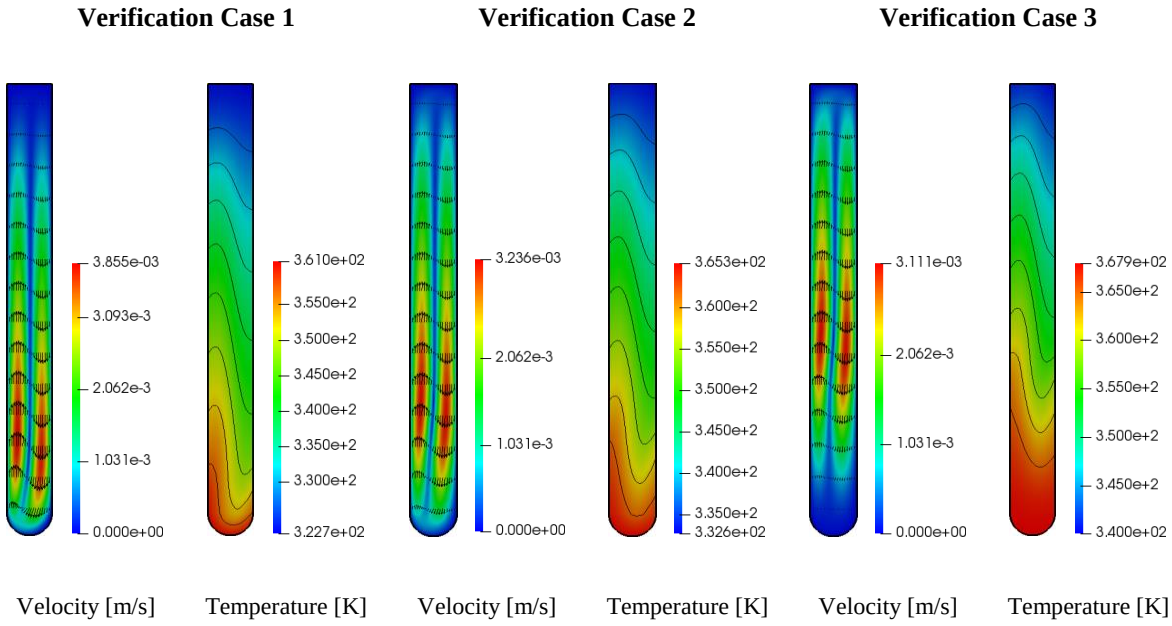

Fig. 5. Velocity and temperature contours of computational results for conjugate momentum and heat transfer model

concentration [1, 21]. The diffusivity of DNAs immersed in water was determined to be 1.0e-7 cm^2/s [1, 21]. The reaction rate for denaturation, annealing, and extension was 0.1 s^{-1}, 0.1 s^{-1}, and 0.05 s^{-1}, respectively [21]. Table 3 shows the performance estimated for the cPCR capillary tubes of the three verification cases as the solution of the species transport model.

TABLE 3

PERFORMANCE ESTIMATION OF THREE VERIFICATION CASES

Properties	Unit	Case 1	Case 2	Case 3
Doubling time	sec	165.72	28.23	78.25

In the experiment, the influenza A (H1N1) virus was utilized to amplify the RNA at a detectable level for the verification. The RNA sample was put into the capillary tube with PCR reagents. The mixture was heated by the resistive heater; the buoyancy-driven convection was made due to the temperature differences. The temperature in the vicinity of the bottom was expected to be approximately 95 ℃, near ideal for reaction, regardless of the cases for the verification. However, it was definite that temperature would be measured to be approximately 50-55 ℃ in the region of the top but vary depending on the height of the resistive heater due to the absence of a top heater. After a single convection loop had been developed in all three cases, the RNA was amplified for 30 min [42]. Fluorescent light was used to detect the RNA amplification, and the variation of the relative fluorescence unit (RFU) was monitored in real-time, as shown in Fig. 6 [1]. Recalling the computational results (Fig. 5), it was certain that the start of the exponential phase was affected by the flow velocity. The sufficient time for the reaction was required for the efficient DNA amplification. That is, the faster the velocity was,

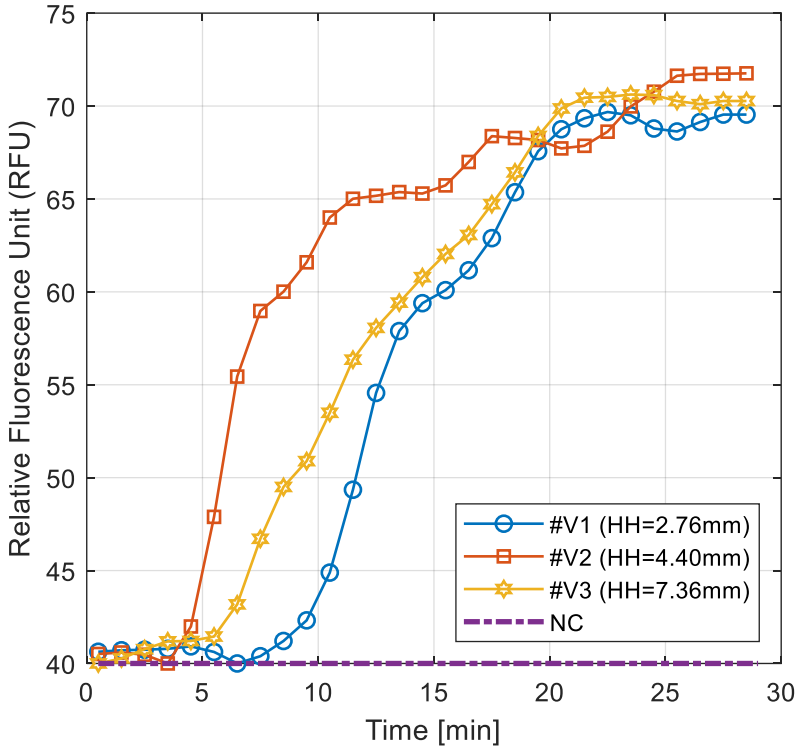

Fig. 6. Relative Fluorescence Unit as a function of real-time, obtained from the experiment in which influenza A (H1N1) virus RNA template is utilized (10.0 TCID50/mL)

the later the exponential phase began. It appeared that #V2 showed the most efficient performance since the exponential phase was made earlier and steeper than that of any other cases; the largest RFU was captured at a plateau as well.

An indirect comparison was made between the experimentation (RFU) and the computation (doubling time) as depicted in Fig. 7 [1]. The RFU which had been recorded at 10 min was selected to indirectly compare it with the doubling time to be obtained from the CFD simulation [1]. The parameters, such as RFU and doubling time, are the performance-related factors, but they have different units. Therefore, the trends of the three verification cases were deemed as the main factor for the comparison. The quantity of the experimentation can be read

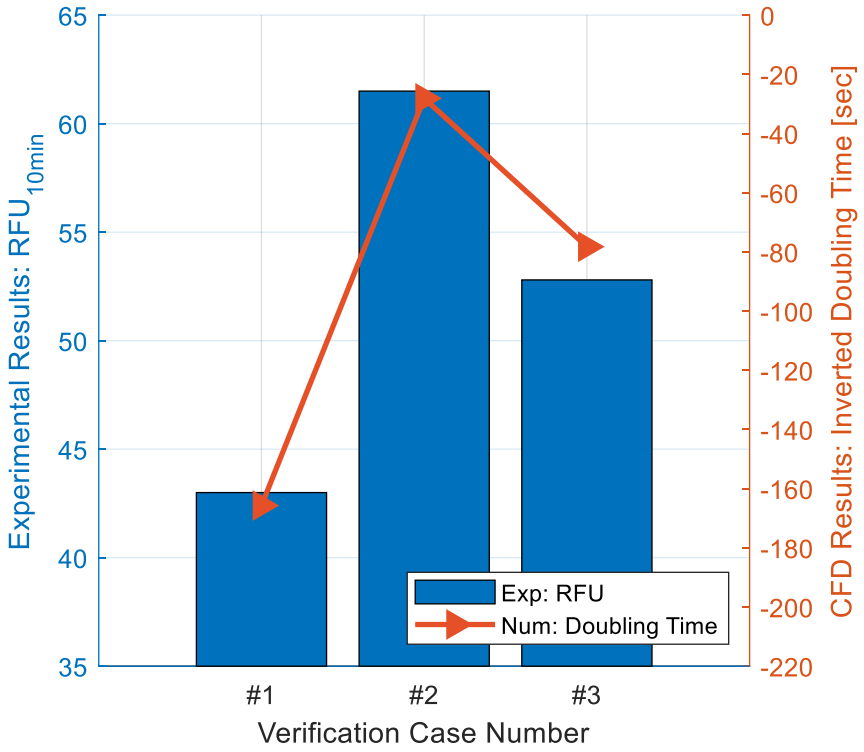

Fig. 7. A comparison of the trends of the three verification cases by the experimentation (left Y-axis) and the computation (right Y-axis)

from the left Y-axis, whereas the inverted quantity of the numerical results is presented on the right Y-axis. Note that better performance is indicated by a larger quantity of RFU (experimentation) or a larger negative quantity of the doubling time (simulation). It was considered the trends were in good agreement, and hence, the mathematical models were verified.

CHAPTER 3

COMPUTATIONAL METHOD FOR PERFORMANCE EVALUATION OF A DOUBLE-HEATER CPCR REACTOR BY DOUBLING TIME

3.1 Overview

In this chapter, a computational methodology is proposed to estimate the performance of cPCR reactors with two heaters. Fig. 8 shows a cPCR reactor with two heaters, which is used for the study in this chapter [1]. The interior of the tube is capillary-shaped, while the exterior has cylindrical geometry. The tube is enclosed by an insulator to block out the convective heat transfer between the capillary tube and the ambient air. The two resistive heaters are in contact

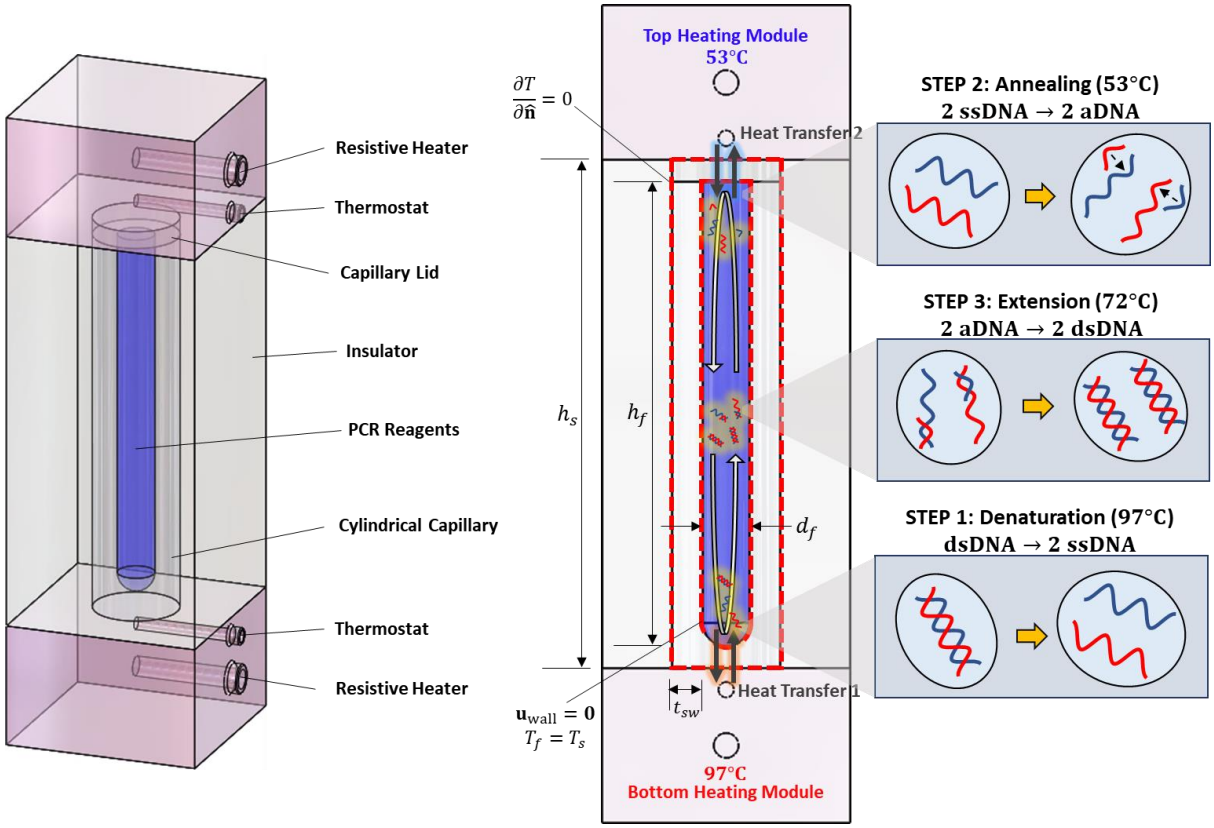

Fig. 8. Schematic of a multi-region thermal convection model for a double-heater cPCR reactor

with the top and bottom surfaces of the tube, respectively [42]. As thermal sources, the heat is transferred to the capillary tube to increase the temperature of PCR reagents. Thermostats are inserted into the tiny holes of the resistive heaters to measure and maintain the temperature to be constant.

This chapter mainly focuses on the validation of the computational codes in which the governing equations represented in Chapter 2 are utilized. Due to the contact method of the resistive heaters on the cylindrical capillary tube, it is expected that the DNA amplification is affected by the diameter and height of a capillary tube. For this reason, this chapter considers four cylindrical capillary tubes with different heights and shows how the shape parameter affects the performance as well.

3.2 Methodologies

DNA amplification is simulated based on the process, as presented in Fig. 9 [1]. The simulation is basically carried out using in-house codes that employ the conjugate momentum and heat transfer model and the species transport model: (1) `chtMultiRegionSimpleFoam`, and (2) `convDiffFoam`. Initially, the steady-state Rayleigh-Bénard problem is solved for the four cylindrical capillary tubes with different heights. The boundary conditions are employed as described in Chapter 2.2, and additionally considered as follows:

- **Temperature boundary conditions**
  - Top Resistive Heating Module: 53 ℃
  - Bottom Resistive Heater Module: 97 ℃
  - Outer Surface of the Cylindrical Capillary Tube: $\partial T/\partial \hat{\mathbf{n}} = 0$ [34]

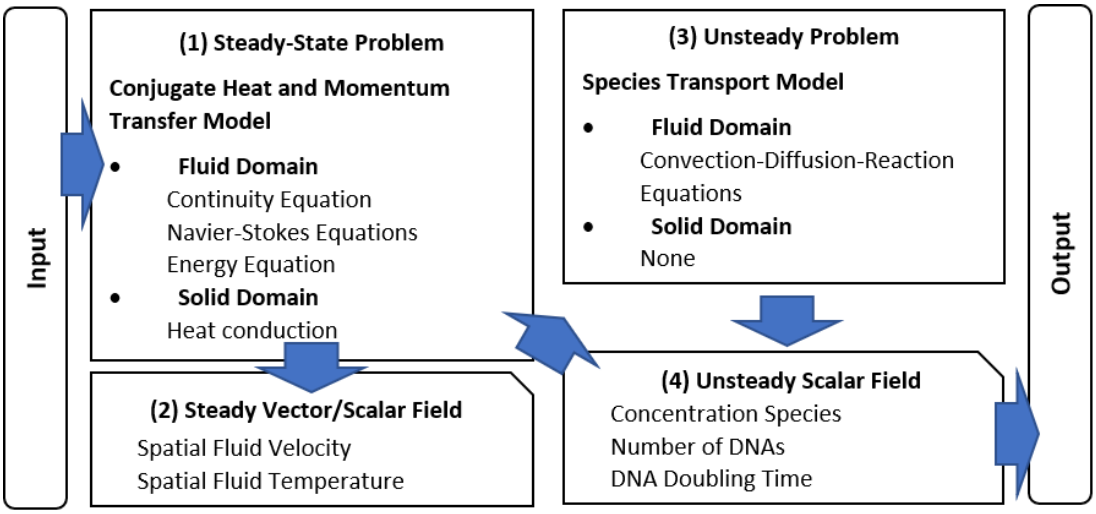

Fig. 9. Flowchart of the in-house developed code to compute DNA concentrations[1]

The temperature field on the solid domain is computed; then, the temperature and velocity fields on the fluid domain coupled with the solid are simultaneously obtained. The CFD solver is run until the residuals of velocity and temperature are less than and equal to the pre-specified tolerances [1]. If the problem is converged, a single convection loop is induced in stable condition, which is required for a stable reaction for DNA amplification. The velocity and temperature fields of the fluid domain are utilized as input for the unsteady species transport model. Concentrations of the respective DNA species are computed using the unsteady species transport model. The initial/boundary conditions are employed, as described in Chapter 2.3. Additional considerations are made as follows:

- **Initial conditions**
  - Concentrations for dsDNA: 100 (number basis)
- **Constant Parameters**
  - Diffusive Coefficient: $10^{-11}\ m^2/s$ [21]
  - Reaction Rate for Denaturation: $0.1\ s^{-1}$ [21, 40]

- Reaction Rate for Annealing: 0.1 s^{-1} [21, 40]
- Reaction Rate for Extension: 0.05 s^{-1} [21, 40]
- Standard Deviation for Denaturation: 5.0 ℃
- Standard Deviation for Annealing: 5.0 ℃
- Standard Deviation for Extension: 2.5 ℃
- Ideal Reaction Temperature for Denaturation: 97 ℃
- Ideal Reaction Temperature for Annealing: 53 ℃
- Ideal Reaction Temperature for Extension: 72 ℃

The DNA species concentration fields are volume-averaged using Eq. (12), varying with time. This volume-averaged concentration is deemed as the number of DNAs dissolved in the solution. Once the dsDNA concentration is computed via CFD simulation, the doubling time is estimated using Eq. (14). The CFD simulation is terminated if the amplification reaches the pre-specified termination time (1,800 s).

3.3 Consideration of capillaries with different heights

The effect of shape parameters on the performance is investigated. For the reactor used for this study, shape parameters are determined as diameter and height. In this study, the diameter is remained to be constant as 1.5 mm, sufficient size for the generation of natural convection, while the height varies with cases. The size of the capillary heights for the presented cases are selected to be 4.535, 8.035, 11.535, and 15.035 mm, respectively, as other published studies adopt the size as nominal [14, 23]. It is expected that the reactor performance will be affected solely by height.

TABLE 4

FOUR DIFFERENT CASES OF CAPILLARIES WITH VARIOUS HEIGHTS

Parameters	Unit	Case 1	Case 2	Case 3	Case 4
Diameter	mm	1.5	1.5	1.5	1.5
Height	mm	4.5	8.0	11.5	15.0
Thickness	mm	1.0	1.0	1.0	1.0
Total Height	mm	4.535	8.035	11.535	15.035

Multiblock meshes are generated as described in Table 4, consisting of a cylindrical block for the solid region and a capillary-shaped block for the fluid region. The solid block is, as a hybrid of structured and unstructured meshes, comprised of hexahedron and tetrahedron cells, whereas the fluid block is a fully structured mesh (hexahedron). Cylindrical capillary tubes with different heights are visualized based on Table 4, as presented in Fig. 10 [1].

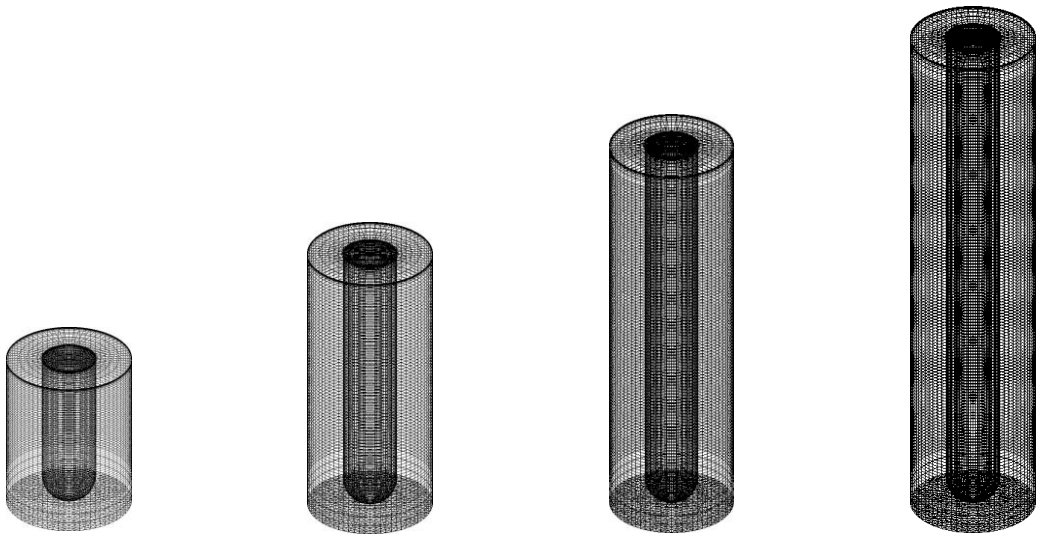

(a) (b) (c) (d)

Fig. 10. Computational domains for Case 1 (a), Case 2 (b), Case 3 (c), and Case 4 (d) [1]

3.4 Grid independent study

We implement a grid independent study to ensure the meshes are sufficiently refined. The parameter of interest is selected to be the volume-averaged velocity; the 3-D conjugate momentum and heat transfer model is used since the only interest is the fluid velocity. Convergence is assumed to be made if set to be the relative percentage error is less than or equal to 1.0 %, a value for which the solution is considered to be independent of the size of cells. As the height differs from case to case, the initial number of cells is assigned to be approximately 90,000, 90,000, 125,000, and 150,000, respectively. The number of cells is constantly increased as an attempt for the grid independent study is additionally made. Fig. 11 represents the results of the grid independent study. It depicts the volume-averaged velocities of Case 1, 2, 3, and 4 that converge at the 3rd, 4th, 5th, and 6th attempt, respectively.

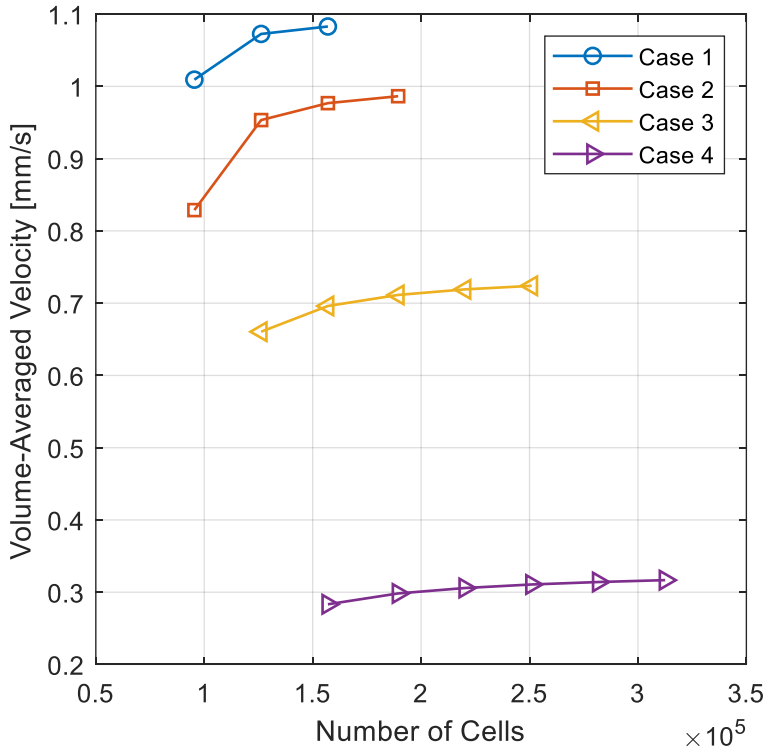

Fig. 11. The effect of the mesh refinement on the volume-averaged velocity

TABLE 5

ERRORS OF THE REFINED MEHSES AT CONVERGED POINTS

Items	Unit	Case 1	Case 2	Case 3	Case 4
Number of Cells	-	157,018	189,418	250,978	312,538
Error	%	0.96	0.98	0.68	0.83

The errors of the respective cases are represented in Table 5. For all the cases, the errors are less than 1 %. It turns out that the solutions are independent of the meshes when the number of cells is 157,018, 198,418, 250,978, and 312,538, respectively.

3.5 Results and discussion

The process was implemented to obtain the results for the aforementioned cPCR designs. Initially, the steady-state OpenFOAM CFD solver, `chtMultiRegionSimpleFoam`, was executed to obtain the velocity and the temperature fields. As presented in Fig. 12, a single convection loop was generated for all the cases, which was required for an efficient DNA amplification. The Rayleigh numbers of the cases were computed to be 3.1829e+05, 2.1423e+06, 6.3636e+06, and 1.4122e+07, respectively. Note that a large Rayleigh number indicates the sufficient strength of convection.

Presented in Table 6 are the maximum/minimum temperatures and velocities over the entire 3-D domains of all cases. It seems that the height of the capillary tube has low sensitivity

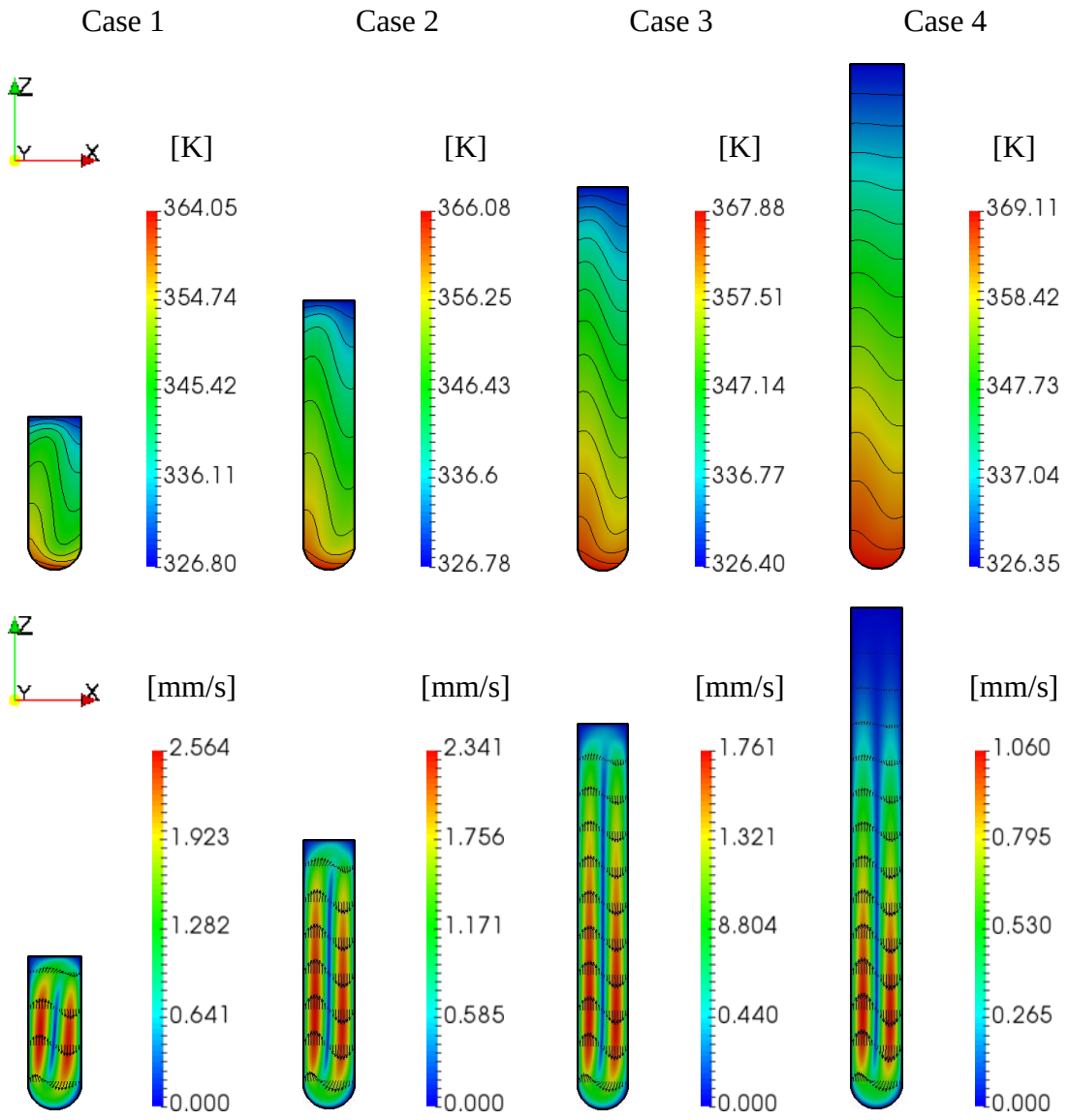

Fig. 12. Temperature (top) and velocity (bottom) contours on the XZ plane

to the maximum/minimum temperatures generated by the heaters in contact with the top and bottom surfaces. The maximum/minimum temperatures of all cases slightly deviate from the ideal temperature for the denaturation (97.0 °C) and annealing (53.0 °C) processes. For example, in Case 3, the temperature computed on the top and bottom regions of the domains are 94.7 °C and 53.3 °C, respectively; and the top region is slightly higher than the ideal temperature for the annealing, whereas the bottom region is slightly lower than the ideal temperature for the

denaturation. The convection cools down the hot surface near the bottom and heats up the cool surface near the top of the capillary tube. It appears that the flow velocity increases the heat transfer between the fluid and solid domains. For this reason, the maximum/minimum temperatures of Case 1 most deviate from the ideal temperature than any other cases owing to the fastest circulation rate. Consequently, it reveals that the capillary height affects the dramatic change of the volume-averaged velocity, but the volume-average temperature.

TABLE 6

MAXIMUM AND MINIMUM VALUES OF TEMPERATURE AND VELOCITY

Variables	Unit	Case 1	Case 2	Case 3	Case 4
Maximum Temperature	°C	91.04	93.05	94.79	95.99
Minimum Temperature	°C	53.52	53.36	53.23	53.13
Volume-Averaged Temperature	°C	71.85	73.55	75.05	75.55
Maximum Velocity	mm/s	3.1528	2.8248	2.1859	1.3214
Volume-Averaged Velocity	mm/s	1.0829	0.9864	0.7240	0.3167

The results also imply that the lower height induces the higher temperature gradient, which affects the velocity fields as well. As a higher temperature gradient produces stronger buoyancy force, it induces a faster flow. Therefore, the flow is found to be slow as the height is increased. Next, the results were obtained by running the unsteady species transport model, `confDiffFoam`. The reaction intensity fields, coupled with the temperature fields, were mapped using Eqs. (8) to (10), as presented in Fig 13. Based upon the verification results in Ch

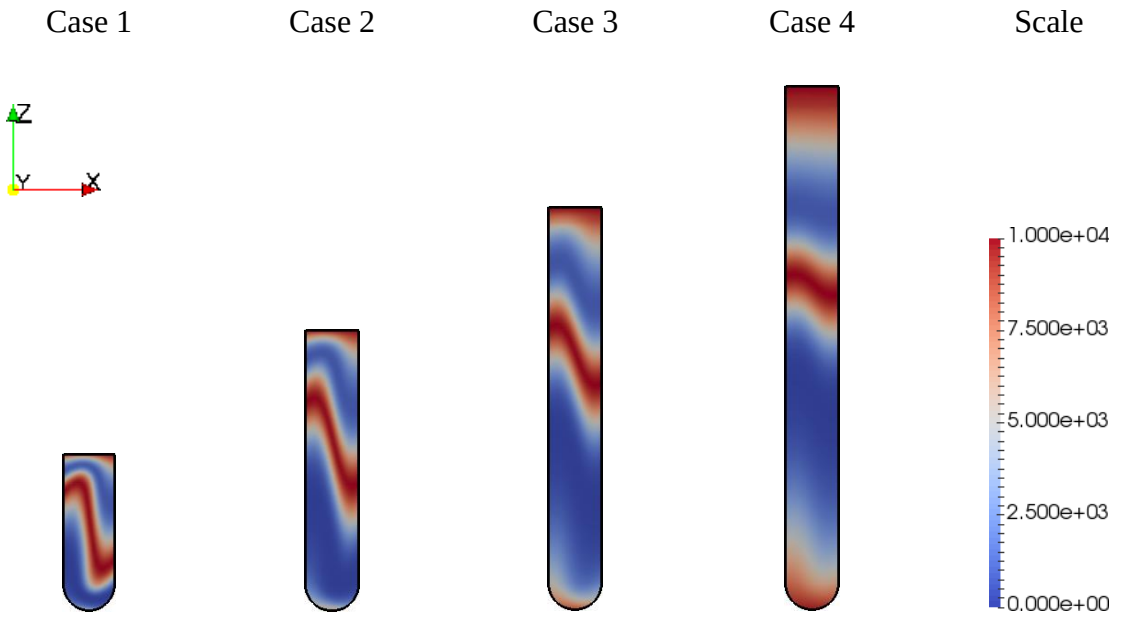

Fig. 13. Reaction intensities coupled with temperature fields

2.4, the reaction intensities were roughly scaled up from 1 to 10,000. As seen in the figure, the red zones are engaged in the annealing, extension, and denaturation processes, strongly affecting the DNA species concentrations and the doubling time [1].

Through the CFD simulation, DNA amplification curves were obtained. The simulation was terminated as the elapsed time for the DNA amplification was 30 min. Fig. 14 represent the DNA amplification curves of all the cases; especially, Fig. 14 (a) shows a zoomed-in area of the DNA amplification curves in the initial state, whereas Fig. 14 (b) depicts the entire area of the curves. As shown in Fig. 14 (a), it is normal that the number of dsDNAs of all cases initially decreases due to the denaturation process and exponentially increases after some point due to the annealing and extension processes. Fig. 14 (b) reveals that all cases have distinctive amplification rates, which describe the superiority of the respective performance.

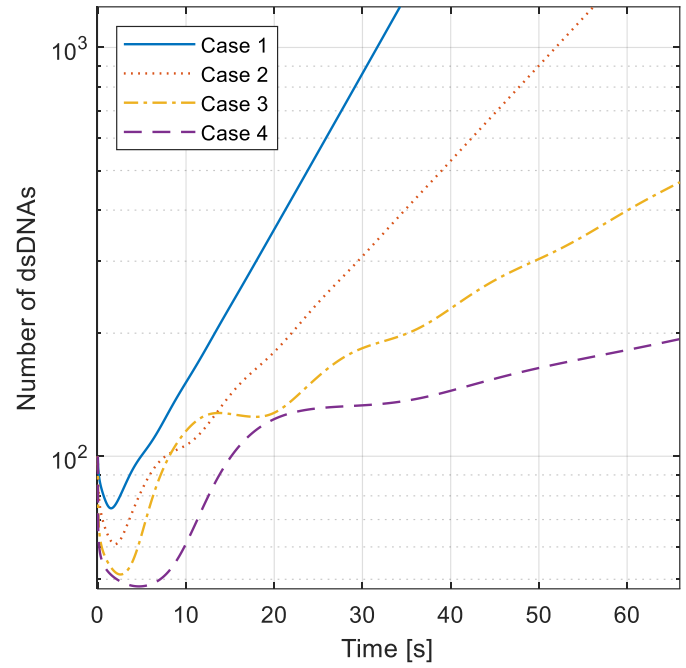

(a)

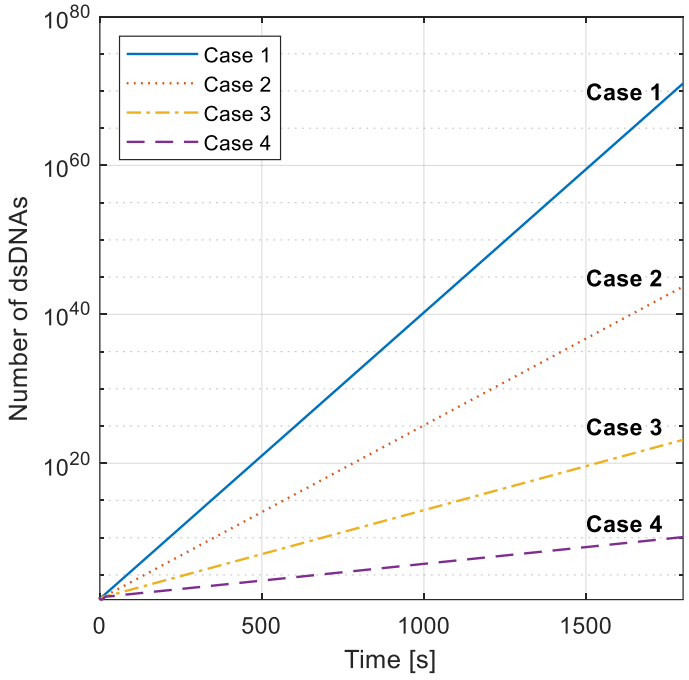

(b)

Fig. 14. Number of DNAs amplified for 1,800 sec: (a) zoom-in, and (b) zoom-out

Generally, the steepest slope is considered to be the best performance. Case 1 is the one on which the largest number of DNAs is counted as the result of the amplification within the given time. From the curves, it appears that the capillary height is inversely proportional to the slope [1]. The curves are of the theoretical yield, differing from the actual experimental phenomenon. The CFD solver for the species transport model produced the results on the assumption that the sufficient amount of primers exists. For this reason, the plateau region was not made on the curves, whereas the primers are used up in experiments.

Additionally, the DNA doubling time was obtained using Eq. (14). As seen in Fig. 15, the initial doubling time is yielded to be larger than the average doubling time, which means that the amplification goes slow at first, and then, gradually accelerated at a constant rate. The

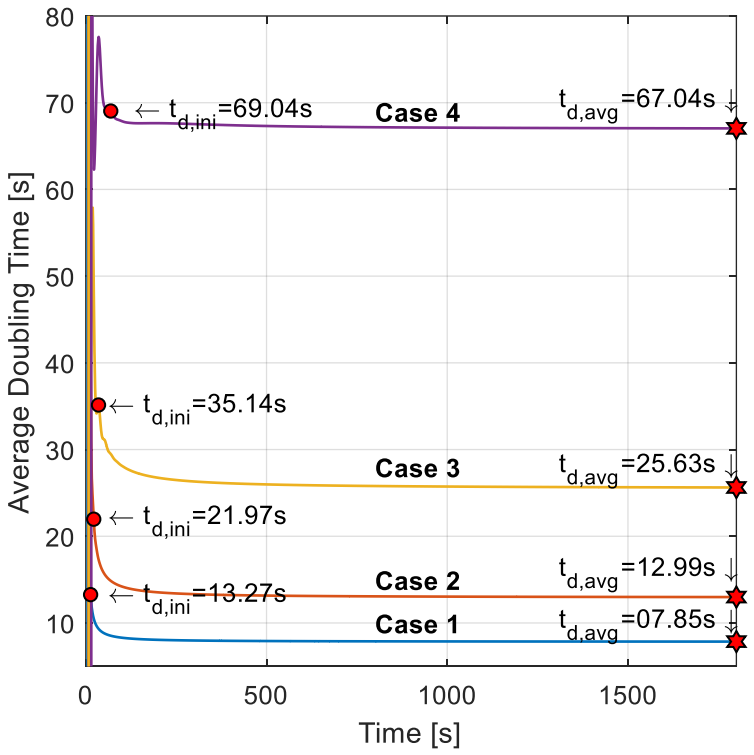

Fig. 15. Convergence history of the average doubling times: (1) initial doubling time (circular-shaped marker), and (2) average doubling time (hexagram-shaped marker)

average doubling time explosively increases for a few seconds, dramatically decreases until the number of dsDNA is initially doubled, and steadily converges as the error of the cases is yielded to be 1.3844e-07, 3.633e-07, 7.464e-07, and 5.843e-07, respectively. It seems that the initial and average doubling times are computed to be lower if the flow circulates faster. The CFD simulation results are summarized in Table 7 [1].

TABLE 7

COMPARISONS OF DOUBLING TIMES FOR CASE 1 TO 4

Variables	Unit	Case 1	Case 2	Case 3	Case 4
Initial Copies of dsDNAs	-	100	100	100	100
Amplified Copies of dsDNAs	-	1.020×10^{71}	5.2651×10^{43}	1.306×10^{23}	1.210×10^{10}
Initial Doubling Time	sec	13.27	21.97	35.14	69.04
Average Doubling Time	sec	7.85	12.99	26.63	67.04
Number of Cycles	-	235	145	76	33
Running Time	min	30	30	30	30

The 100 copies of dsDNA were initially doubled at 13.27 sec (Case 1), 21.97 sec (Case 2), 35.14 sec (Case 3), and 69.04 sec (Case 4). The average doubling time measured at the terminal time was computed to be 7.85 sec (Case 1), 12.99 sec (Case 2), 26.63 sec (Case 3), and 67.04 sec (Case 4) after the amplification reaches 235, 145, 76, and 33 cycles, respectively. It is considered that the performance of Case 3 is close to the doubling time of a conventional PCR system as it is reported in the literature to be approximately 20-25 sec [19, 22]. Nevertheless, the

results reveal that the copies of DNAs are amplified at a faster rate for Cases 1 and 2; the doubling times of the corresponding cases are found to be shorter. It is somewhat unexpected because it is typically believed that the higher aspect ratio of a PCR reactor renders better in performance. However, the results make sense since the primer is assumed to be infinite and, therefore, no plateau effect is made from the simulation.

3.6 Conclusions

In this chapter, the performance of double-heater cPCR reactors has been quantified based on the DNA doubling time to confirm if they could be efficiently developed using the computational method. Mathematical models for the quantification of DNA amplification are investigated and used for the development of CFD solvers. A three-dimensional, conjugate momentum and heat transfer model has given insight into the heat flow patterns that occur in cPCR reactors. The thermal properties of pure water in the polynomial form improved the accuracy of the model. The fluid domain thermally coupled with the solid made the model highly reliable as well. The DNA species transport model provided a method for quantifying the performance of cPCR reactors through CFD simulations.

Various cases of the double-heater reactor were selected with different height to demonstrate the computational method could capture the variation of the performance affected by shape parameters. The performance of the cases was evaluated via CFD simulations, and comparisons were made qualitatively and quantitatively for analysis. It was observed that the reaction was considerably dominated by the velocity rather than what is commonly believed to be the quality of the flow circulation.

Consequently, through the analysis of the double-heater reactor, we confirmed that the proposed method has the capability of effectively estimating the DNA doubling time, the number

of cycles, and the number of DNAs. It has great potential to reduce the development cost dramatically by being independent of experimentation.

In the next chapter, we will analyze a single heater cPCR reactor in the aspect of design based on the suggested models used for the double-heater reactor. Additionally, a design methodology will be proposed to show how to resolve the challenge of a single heater reactor.

(This page is intentionally left blank)

CHAPTER 4

DESIGN METHODOLOGY OF A SINGLE HEATERCONVECTIVE PCR REATOR TOWARD POINT-OF-CARE

4.1 Overview

POC testing devices are designed to ensure the quality and performance of in-vitro diagnostics, allowing near-patient testing in a hospital, doctor's office, clinic, or home. Early treatment decisions can be made if results are quickly obtained by the POC tests. Non-experts can purchase devices as POC applications at a low price and use it after a short learning period.

Single-heater cPCR devices are advantageous for the use of POC due to simplicity, low expenses, and portability. It is somewhat challenging to design reactors that assure the best performance for DNA amplifications due to the difficulty in maintaining the ideal temperature for the PCR thermal cycling processes. It is significant to find the best size of shape parameters since they seriously affect the performance.

This chapter introduces a design methodology for single heater reactors for high-performance, low-cost development of cPCR devices as POC applications. A capillary-tube-like reactor is considered to find the best shape effective for performance. Different from the previous chapter, only the lower part of a reactor is inserted into a resistive heating module. The outer surface of a reactor exposed to the ambient air loses heat due to the convective heat transfer between the reactor and the air. Hence, heat is added from the bottom to the top and escapes from inside to outside. The numerous designs with different shape parameters are produced through the design of experiments (DOE) method; the performance is evaluated for all design candidates using a computational method to find the appropriate design for the POC testing.

4.2 Methodology

The design space is investigated to comprehend the reactor performance as the shape parameters change. Numerous reactor designs are considered by changing the values of the parameters. A reactor baseline to be used for this study is parameterized, as depicted in Fig. 16, with three variables: (1) diameter, (2) height, and (3) heater height. Here, the diameter is pointed out to be the inner diameter of the cross-sectional area of the capillary tube; the height is the maximum distance of the region from bottom to top, where the PCR reagent is fully filled. The thickness of the capillary tube is a constant parameter determined to be 0.7 mm due to the durability and the manufacturability [43]. The heater height is defined as the distance between the top of the heater and the bottom of the capillary tube.

A capillary tube is made of polymethyl methacrylate (PMMA) with good diathermancy for convection. PCR reagents filling the capillary tube are assumed to be pure water for

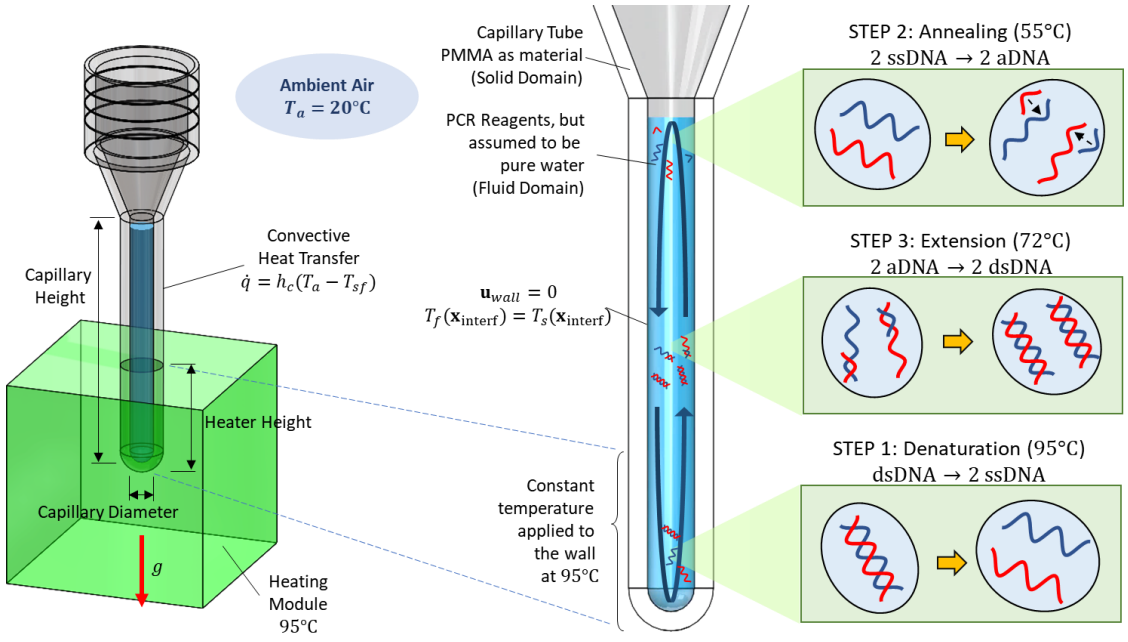

Fig. 16. Schematic of the multi-region thermal convection model for a single heater cPCR reactor

simplicity. The resistive heater maintains the constant temperature at 95 °C; the heat is transferred through the solid domains by conduction, inducing convection within the fluid domains. The temperature is required to remain at approximately 55 °C on the top region as the result of heat transfer from the resistive heater to the capillary tube and from the capillary tube to the ambient air (20 °C). Owing to the dependency of the fluid density upon temperature, the spatial temperature distributed over the fluid domains induces a convection loop efficient for DNA amplification.

The mathematical model for the steady-state buoyancy-driven fluid motion is defined in the dimensional form of the continuity, momentum, and energy equations, as presented in Chapter 2.2. A polynomial form of the fluid thermal properties, as seen in Table 1, is used to solve the mathematical model. The thermal conductivity of PMMA is assigned a constant value of 0.22 $W/(m \cdot K)$. The boundary conditions are employed as described in Chapter 2.2, and additionally considered as follows:

- **Temperature boundary conditions**
  - Bottom Resistive Heater Module: 95 °C
  - Convective Heat Transfer Coefficient: 9 $W/(m^2K)$ [44]
  - Temperature of Ambient Air: 20 °C

A process for DNA amplification is simulated using the DNA species transport model as introduced in Chapter 2.3. The initial/boundary conditions are employed, as described in Chapter 2.3. Additional considerations are made as follows:

- **Initial conditions**
  - Concentrations for dsDNA: 100 (number basis)

- **Constant Parameters**
  - Diffusive Coefficient: $10^{-11}\ m^2/s$
  - Reaction Rate for Denaturation: $0.1\ s^{-1}$
  - Reaction Rate for Annealing: $0.1\ s^{-1}$
  - Reaction Rate for Extension: $0.05\ s^{-1}$
  - Standard Deviation for Denaturation: 5.0 ℃
  - Standard Deviation for Annealing: 5.0 ℃
  - Standard Deviation for Extension: 2.5 ℃
  - Ideal Reaction Temperature for Denaturation: 95 ℃
  - Ideal Reaction Temperature for Annealing: 55 ℃
  - Ideal Reaction Temperature for Extension: 72 ℃

The DNA species concentration fields are volume-averaged using Eq. (12), varying with time. This volume-averaged concentration is deemed as the number of DNAs dissolved in the solution. Once the dsDNA concentration is computed via CFD simulation, the doubling time is estimated using Eq. (14). The CFD simulation is terminated if the amplification reaches the pre-specified termination time (1,800 s).

4.3 Design Process

A design process is established to develop a single heater reactor, which is economical, efficient, and portable. As seen in Fig. 17, the process is initiated with the inputs related to reactor geometries, such as diameter, aspect ratio (defined as the ratio of height to diameter), and heater height. Design space is investigated using the design-of-experiments (DOE) method. A total of 60 possible reactor design cases are considered by combining sets of values of the input parameters as presented in Tables 8 to 10, which are grouped by the diameter:

TABLE 8

POSSIBLE REACTOR DESIGN CANDIDATES AS GROUP 1

DN[a]	# 1	# 2	# 3	# 4	# 5	# 6	# 7	# 8	# 9	# 10	# 11	# 12	# 13	# 14	# 15	# 16	# 17	# 18	# 19	# 20
d[b]	1.0	1.0	1.0	1.0	1.0	1.0	1.0	1.0	1.0	1.0	1.0	1.0	1.0	1.0	1.0	1.0	1.0	1.0	1.0	1.0
AR[c]	6.0	6.0	6.0	6.0	6.0	8.0	8.0	8.0	8.0	8.0	10.0	10.0	10.0	10.0	10.0	12.0	12.0	12.0	12.0	12.0
HH[d]	20.0	25.0	30.0	35.0	40.0	20.0	25.0	30.0	35.0	40.0	20.0	25.0	30.0	35.0	40.0	20.0	25.0	30.0	35.0	40.0

[a]Design Number; [b]Diameter (mm); [c]Aspect Ratio; [d]Heater Height (%)

TABLE 9

POSSIBLE REACTOR DESIGN CANDIDATES AS GROUP 2

DN	# 21	# 22	# 23	# 24	# 25	# 26	# 27	# 28	# 29	# 30	# 31	# 32	# 33	# 34	# 35	# 36	# 37	# 38	# 39	# 40
d	1.5	1.5	1.5	1.5	1.5	1.5	1.5	1.5	1.5	1.5	1.5	1.5	1.5	1.5	1.5	1.5	1.5	1.5	1.5	1.5
AR	6.0	6.0	6.0	6.0	6.0	8.0	8.0	8.0	8.0	8.0	10.0	10.0	10.0	10.0	10.0	12.0	12.0	12.0	12.0	12.0
HH	20.0	25.0	30.0	35.0	40.0	20.0	25.0	30.0	35.0	40.0	20.0	25.0	30.0	35.0	40.0	20.0	25.0	30.0	35.0	40.0

TABLE 10

POSSIBLE REACTOR DESIGN CANDIDATES AS GROUP 3

DN	# 41	# 42	# 43	# 44	# 45	# 46	# 47	# 48	# 49	# 50	# 51	# 52	# 53	# 54	# 55	# 56	# 57	# 58	# 59	# 60
d	2.0	2.0	2.0	2.0	2.0	2.0	2.0	2.0	2.0	2.0	2.0	2.0	2.0	2.0	2.0	2.0	2.0	2.0	2.0	2.0
AR	6.0	6.0	6.0	6.0	6.0	8.0	8.0	8.0	8.0	8.0	10.0	10.0	10.0	10.0	10.0	12.0	12.0	12.0	12.0	12.0
HH	20.0	25.0	30.0	35.0	40.0	20.0	25.0	30.0	35.0	40.0	20.0	25.0	30.0	35.0	40.0	20.0	25.0	30.0	35.0	40.0

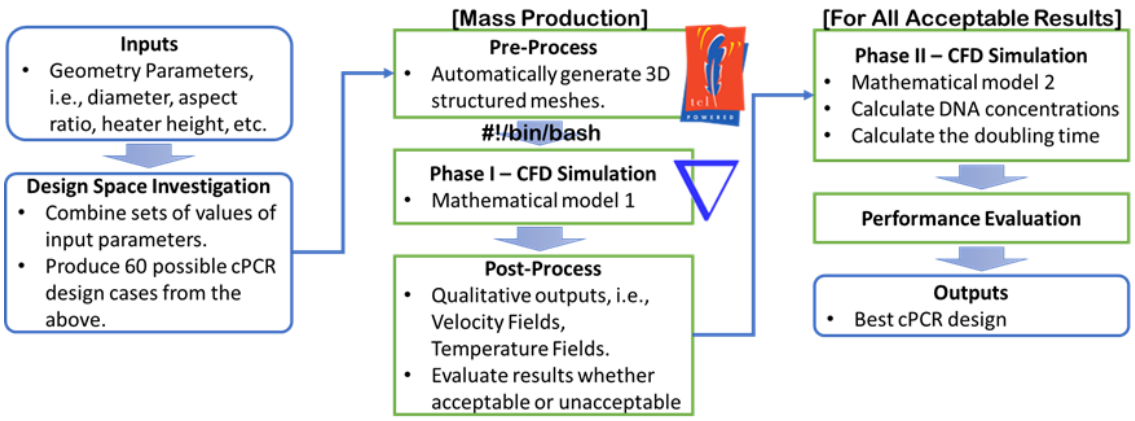

Fig. 17. Design process for single heater cPCR reactors for a POC application

Based on the designs reported in the literature, sets of values are determined as follows [14]: (1) diameter: 1.0 mm, 1.5 mm, and 2.0 mm; (2) aspect ratio: 6.0, 8.0, 10.0, and 12.0; (3) height of a heater: 20.0 %, 25.0 %, 30.0 %, 35.0 %, and 40.0 % of the total height of a capillary tube.

The developed script (`tcl`-basis) enables a user to automatically generate a mesh within a couple of seconds based on the design space (See Appendix B). A total of 60 structured meshes are generated with a hexahedral type of cells. In Phase I of the CFD simulation, the flow velocity and temperature are estimated by simultaneously solving the steady-state conjugate mass and heat transfer equations (fluid region) and heat conduction equations (solid region), which are described in Chapter 2.2. In the post-process of Phase I, the results, such as velocity, and temperature, are visualized and collected to organize a form of a design matrix. All cases are evaluated based on the velocity field visualized and the maximum/minimum fluid temperature computed. The evaluation criteria are defined as [45-47]:

(1) A single convection loop is formed in the fluid region;

(2) Temperature field has a maximum of 95 ± 5 ℃ and a minimum of 55 ± 5 ℃.

If satisfying the criteria, a candidate can be determined as “acceptable design,” and If not, a candidate is determined as “unacceptable design.” In Phase II of the CFD simulation, the obtained velocity and temperature fields from Phase I are utilized to be inputs for the time-dependent species transport equations (convection-diffusion-reaction), as described in Chapter 2.3. Phase II CFD simulation is carried out only for the acceptable candidates. The performance of a reactor is quantified by the DNA doubling time based on the computed concentrations for DNAs. Once the average doubling time is obtained for all acceptable candidates, the performance evaluation is conducted, and finally, the best reactor design can be found.

4.4 Results and Discussion

All sixty design candidates are simulated based on the proposed process and mathematical models. For the results of Phase I CFD simulation, as represented in Fig. A-3, the velocity magnitude is equivalent to zero for all the cases with a diameter of 1.0 mm. Fig. A-4 shows that the temperature gradients in a piecewise direction are approximately zero as well. That is, the natural convection does not take place inside the capillary tubes. The heat is transferred in the form of heat conduction. It appears that the Rayleigh number of these candidates, with a diameter of 2.0 mm, is much smaller than the critical number for convection. Since the Rayleigh number is directly proportional to the characteristic length, either the diameter of the height should be larger to develop the flow convection required for DNA amplification.

As seen in Fig. 18 (a), the volume-averaged velocities of the corresponding candidates are increased by the smaller aspect ratio and the higher heater height. However, the magnitude of the volume-averaged velocity of the corresponding candidates is very small; hence, they are practically zero in magnitude. Additionally, the volume-averaged velocity in the graph (a) may

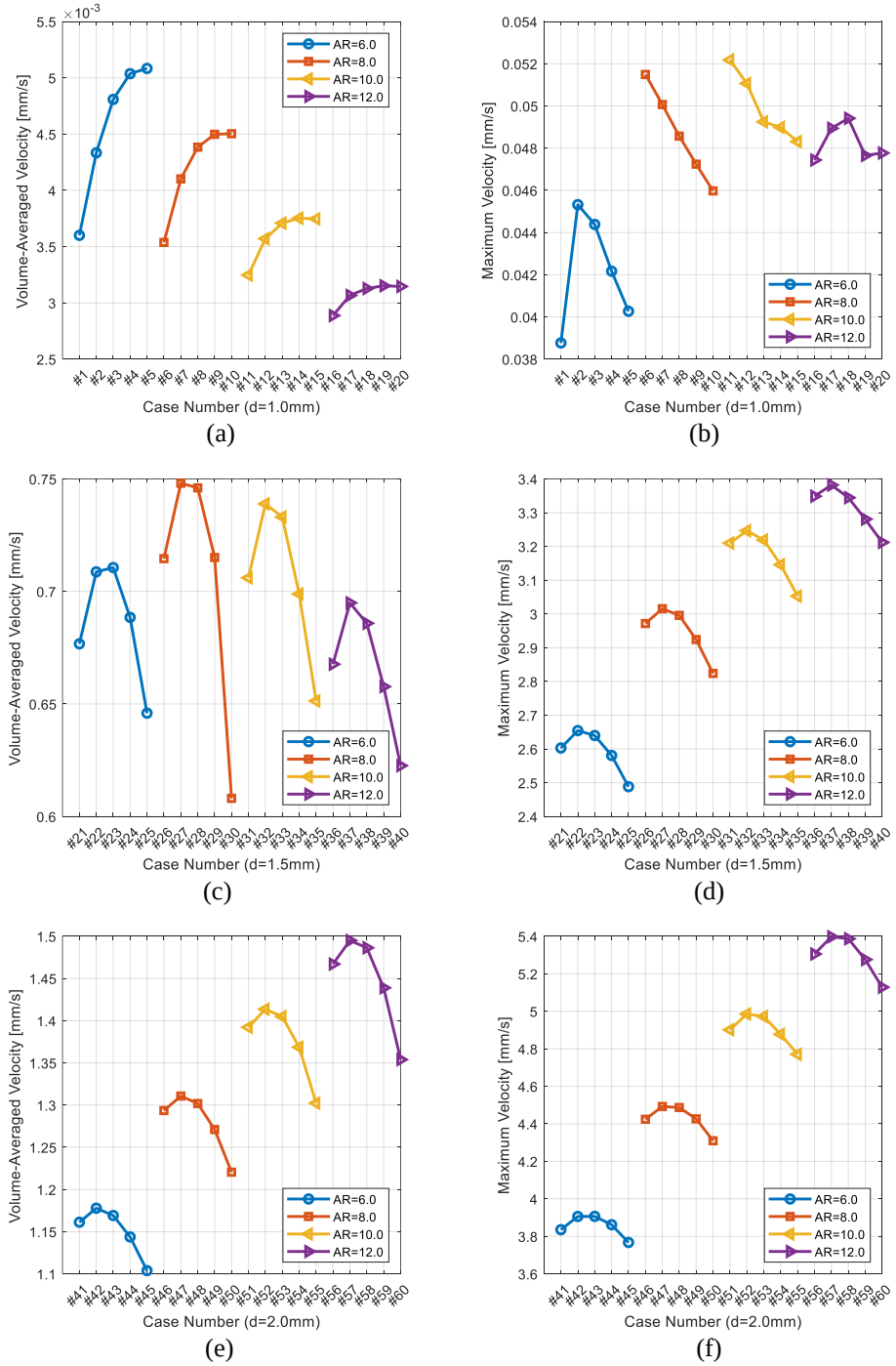

Fig. 18. Volume-averaged and maximum velocities categorized by diameter: (a), (c), and (e) volume-averaged velocity (1.0 mm, 1.5 mm, and 2.0 mm); (b), (d), and (f) maximum velocity (1.0 mm, 1.5 mm, and 2.0 mm)

seem to imply that the convection would be induced with the smaller aspect ratio. However, it does not so, because of the trend of the maximum velocity decreasing with the aspect ratio, as shown in Fig. 18 (b), which affects the characteristic length. Low aspect ratios would result in low Rayleigh number. With the stationary flow condition, heat is transferred in the form of conduction rather than convection; no further reactions on DNA species are expected. For this reason, the diameter of a capillary is recommended to be greater than 1.0 mm.

A single convection loop is attained by the candidates with a diameter of 1.5 mm, as presented in Fig. A-5. The capillary tubes with the aspect ratio of 6.0 are fully covered with a convection loop. Fluid dead zones are observed to be small in the candidates with the aspect ratio of 8.0, while the candidates with the aspect ratio of 10.0 and 12.0 have larger fluid dead zones in the regions where the local temperature is isolated. In principle, the steep temperature gradients are displayed in all corresponding cases, as depicted in Fig. A-6, provoking the change of the velocity over the entire volume. The dead zone is formed when the aspect ratio is excessively high, or the heater height is too low. This observation is supported by the trends of the volume-averaged and maximum velocities, as seen in Fig. 18 (c) and (d).

The candidates with a diameter of 2.0 mm have convection loops fully developed, as shown in Fig. A-7. The aspect ratio of the corresponding candidates seems to have less influence on the dead zones. The volume-averaged and maximum velocities increase with the aspect ratio getting higher, as presented in Fig. 18 (e) and (f). The candidates of this group have the flow velocities faster than any other cases when the heater height is 25.0 %, whereas the lowest flow velocities are monitored when the heater height is 40.0 %. It means that the heater height is the main factor that affects the dead zone, which can be more affected by the heater height than by the aspect ratio for the given conditions. The temperature gradients of the candidates in Group 3

are steeper compared with the others in Groups 1 and 2 of which the diameter of 1.0 mm and 1.5 mm (Fig. A-8). However, it is deemed that the candidates in Group 3 are determined to be "unacceptable designs" due to the failure of satisfaction of the second item in the evaluation criteria as presented in Chapter 4.3.

Only eleven of them satisfy the prerequisite two evaluation criteria, hence considered as "acceptable designs." It reveals that these are #26, #27, #31, #32, #33, #34, #36, #37, #38, #39, and #40. As looking into the acceptable designs, the dead zones are inevitably accompanied. The acceptable candidates are regrouped by the aspect ratio as RG1, RG2, and RG3, of which the aspect ratio is 8.0, 10.0, and 12.0, respectively.

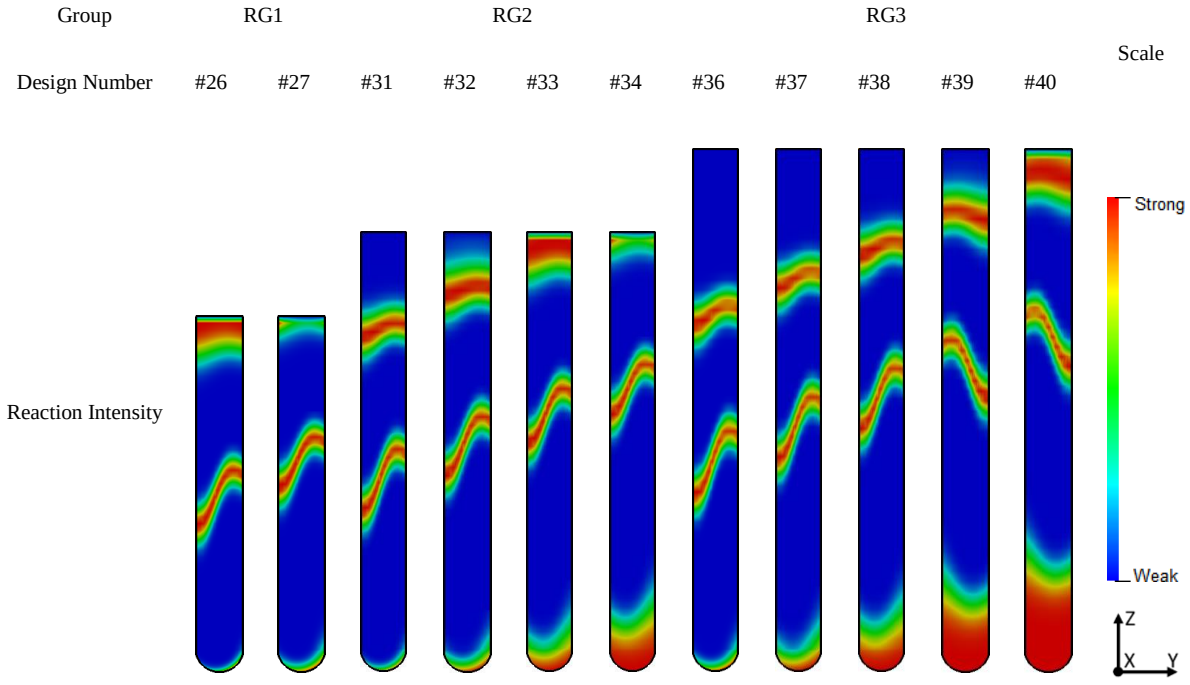

Fig. 19. Reaction intensities coupled with the temperature field; $f_a(\mathbf{x})$: strong in upper, $f_e(\mathbf{x})$: strong in mid, $f_d(\mathbf{x})$: strong in lower regions

CFD simulations in Phase II are carried out only for the "acceptable designs." The reaction intensities for denaturation, annealing, and extension are mapped based on the temperature field as depicted in Fig. 19. Note that the reaction intensity is one of the factors which affect the average doubling time. The reaction intensities of the denaturation, annealing, and extension are strong in the lower, upper, and mid regions, respectively, as colored in red, while a weak reaction is colored in blue. The location of the red zones of the respective processes is dependent on the aspect ratio and heater height, which are the factors to influence the temperature distribution. For some design candidates, the dead zones are overlapped with the regions of strong reaction intensities. The molecules, such as DNAs, primers, and so on, rarely pass through the regions; therefore, weak reactions are expected in the vicinity of such regions.

TABLE 11

INITIAL AND AVERAGE DOUBLING TIME FOR ALL ACCEPTABLE CANDIDATES

Group Number	RG1		RG2				RG3				
Design Number	#26	#27	#31	#32	#33	#34	#36	#37	#38	#39	#40
Initial Doubling Time [sec]	173.3	286.0	89.5	97.6	145.5	254.2	71.7	76.0	86.3	106.1	147.9
Average Doubling Time [sec]	107.4	77.9	40.3	28.2	39.0	68.5	25.2	22.9	26.6	32.6	40.2

Table 11 shows the initial and average doubling time for all acceptable candidates. It seems that Design #40 would assure the best performance given that it has the largest red zones for the strong reaction intensities. However, Design #37 is determined to be the best performing with 22.87 sec of the average doubling time. Design #26 has the worst performance as 107.41

sec of the average doubling time. Even though the convection loop is fully developed inside the capillary tube, the reaction intensity of denaturation is weak and small in magnitude.

The best performance is assured if the reaction intensities of the denaturation and annealing are moderate and full in size, respectively, and if flow with the molecules, which passes through it, has the proper velocity. Ironically, the dead zones are unnecessarily accompanied with the reactors that assure better performance in the doubling time.

Another consideration in selecting the best candidate is the reactor capacity for PCR reagents needed for the testing as it is assumed to raise the cost of operations. A case study is made to find a compromise between performance, as aforementioned, and volume of reagents required for testing. Fig. 20 represents the velocity, temperature fields, and their performance of the candidates selected the best in the respective groups. The best performing design is selected,

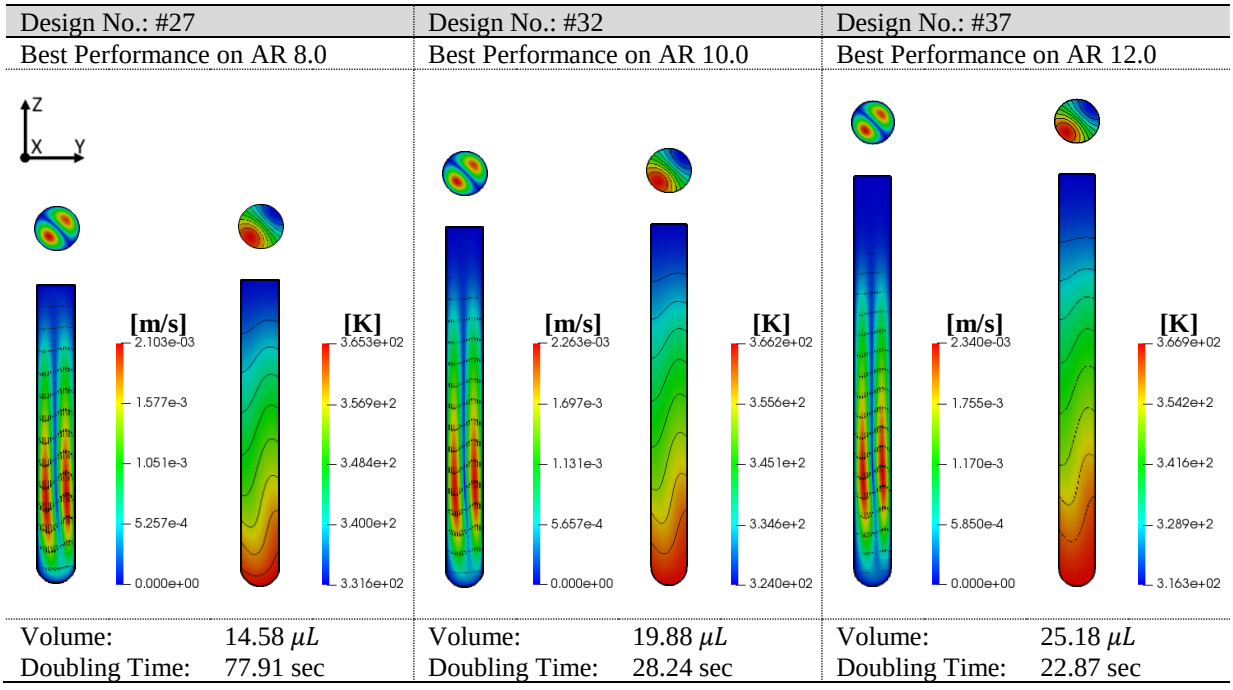

Fig. 20. Velocity and temperature contours and performance of best design candidates selected in respective groups

which are #27, #32, and #37 in RG1, RG2, and RG3, respectively. Design #27 has the smallest volume capacity and the lowest performance among the three best-in-group candidates. The choice between Designs # 32 and #37 would be dependent upon which factors are more valuable to the user: smaller volume of reagents but a moderate amplification rate, or the fastest amplification rate but a large amount of reagent needed.

4.5 Conclusions

In this chapter, we have introduced a design methodology to develop a single heater cPCR reactor to be portable, economical; yet still, be accurate and efficient for a POC application. One challenge that we emphasized on the design of a single heater cPCR was to achieve the temperatures for thermal cycling processes for DNA amplification. We have effectively resolved the challenge at low cost by adopting a computational design process.

The cPCR model used in this chapter had three-dimensional, multi-regional blocks made up of the fluid and solid regions. For higher-fidelity simulations, we considered the solid domains thermally coupled with the fluid domains to induce a single convection loop in the fluid domains. The design space was investigated by planning the DOE method. A total of sixty-four design candidates were initially simulated based on the conjugate momentum. The performance of all design candidates was qualitatively evaluated according to the evaluation criteria, resulting in eleven “acceptable design” candidates. We implemented Phase II CFD simulations (species transport model) to quantify the performance of the acceptable candidates by the doubling time.

We also carried out a case study to demonstrate a compromise between the performance and the volume capacity of the reactors. The best designs were found to be Design #32 (diameter 1.5 mm; aspect ratio 10.0; heater height 25.0 %), and Design #37 (diameter 1.5 mm; aspect ratio 12.0; heater height 25.0%) as the double time of 28.24 sec and 22.87 sec, and the

volume capacity of 19.88 μL and 25.18 μL, respectively. Through the study, it was demonstrated that a single heater cPCR reactor could be effectively designed using the proposed methodology.

In pursuit of a POC application, testing in various environments is necessary. The performance of POC devices should be guaranteed even if one might use a cPCR device any time, any places, or any conditions. In the next chapter, we will cover one of the conditions aforementioned: the operating position. A single heater cPCR will be laid down in a horizontal position, and the performance will be evaluated for the comparison with a reactor in a vertical position.

CHAPTER 5

REAL-TIME CONVECTIVE PCR BASED ON HORIONTAL THERMAL CONVECTION

5.1 Overview

Various PCR systems are developed to be economical, efficient, and portable for POC testing. Real-time PCR devices are beneficial since they can be used to monitor DNA amplification in real time [2]. A real-time cPCR is the one that takes benefits of both real-time PCR and cPCR systems. It has the potential to achieve higher efficiency even with a simplified heating system. A compact setup enables to produce stable thermal convection induced inside a capillary tube and detect fluorescence emitted from PCR reagents as proof of the efficient amplification of DNA in real time.

This chapter reports the real-time cPCR system based on horizontal thermal convection to be used as a POC application. The real-time, cPCR system is developed to induce horizontal convection inside the capillary tube. The reactor is heated at one-end in a pseudo-isothermal manner, achieving efficient thermal cycling processes for denaturation, annealing, and extension [2]. Through the CFD simulations, it can be confirmed that a repeatable and continuous convection loop is produced in the horizontal direction. The inherent mechanism of the real-time cPCR in a horizontal position is computationally analyzed with mathematical models and confirmed with experimentation. The performance of the horizontal cPCR is evaluated with the detection of influenza A (H1N1) virus nucleic acid targets.

5.2 Real-Time Horizontal cPCR

The real-time horizontal cPCR system is made up of the horizontal reactor, and the control/detection modules. As shown in Fig. 21, the reactor is positioned in a horizontal direction, having a volume capacity of up to 40 µL with an outer diameter of 3.3 mm, an inner diameter of 1.7mm, and a length of 19 mm [2, 43]. Capillary tubes are made from polycarbonate by injection moldings due to its remarkably smooth surface and the satisfied transparency for optical detection. The reactor is laid down to produce horizontal thermal convection. A resistive heater is in contact with one end of the capillary tube, generating a stable steady-state temperature gradient along the horizontal direction. The reactor induces a continuous back-and-forth circulation for reactants to move between hot and cool regions, achieving the efficient PCR thermal cycling.

A compact setup is developed to perform real-time horizontal cPCR, as shown in Fig. 22. A one-end heating strategy uses a resistive heater to increase the temperature of reagents in the

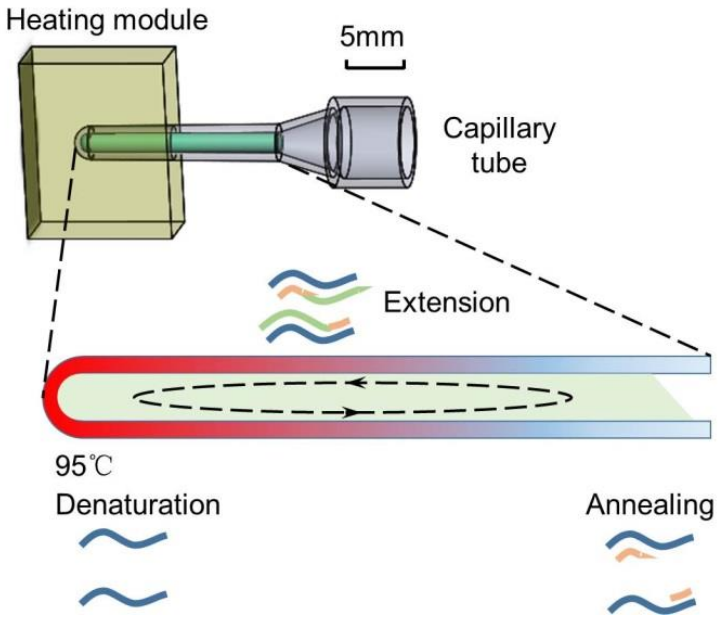

Fig. 21. cPCR reactor for horizontal convection (Figure by courtesy of Dr. Xianbo Qiu) [2]

capillary tube. A thermistor measures the temperature applied to the one-end of the capillary tube. A smartphone camera is utilized as a real-time monitoring module to detect fluorescence emitted from the reaction of DNA amplification. The system has two sub-systems for the thermal control and optical detection, which are integrated to implement the real-time horizontal cPCR. A PID controller ensures to maintain precise temperature for one end heating. An optical module is made up of a LED with an optical filter for excitation and a smartphone camera equipped with another optical filter for detection of fluorescence emission, enabling convenient detection.

For the TaqMan probe conjugated with FAM™, a high excitation efficiency can be achieved by adopting a specific LED with a proper wavelength of 475 nm. Fluorescence images are captured using a custom Java application running on the smartphone. A custom image algorithm allows the smartphone to implement quantification by processing the fluorescence

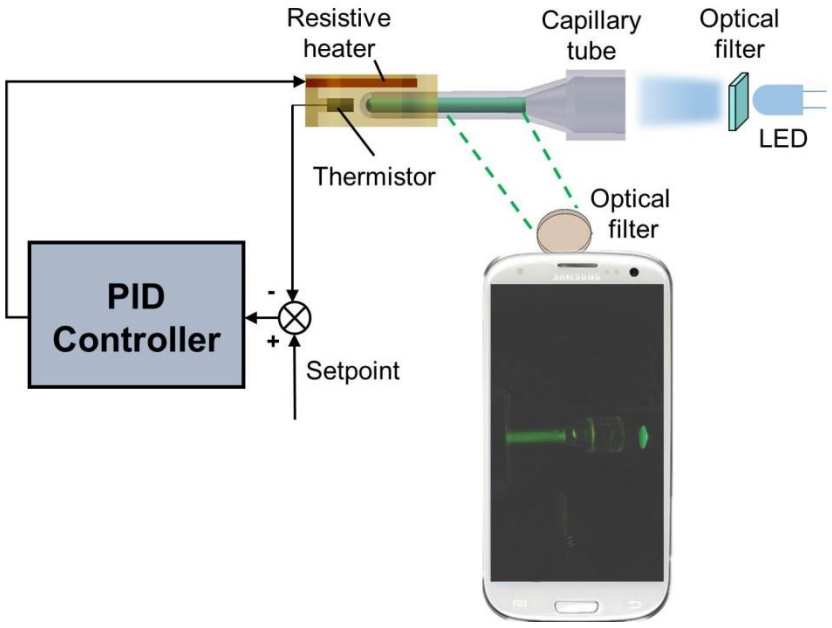

Fig. 22. Schematic of real-time horizontal cPCR system (Figure by courtesy of Dr. Xianbo Qiu) [2]

images collected in real-time. The amplitude of fluorescence intensities is recorded over time and visualized for quantification. A compact system has dimensions of 100 mm × 70 mm × 150 mm; and it carries out real-time quantification with a total cost of approximately $ 50, not including the smartphone.

5.3 Methodology for Computational Simulations

The 3-D models are applied for the horizontal cPCR as well as the vertical cPCR for comparison. The mathematical model for the steady-state buoyancy-driven fluid motion is defined in the dimensional form of the continuity, momentum, and energy equations, as presented in Chapter 2.2. A polynomial form of the fluid thermal properties, as seen in Table 1, is used to solve the mathematical model. The thermal conductivity of polycarbonate is assigned a constant value of 0.22 $W/(m \cdot K)$. Fig. 23 represents 3-D models for the horizontal and vertical cPCR to be used for the computational analysis. The computational domains for both

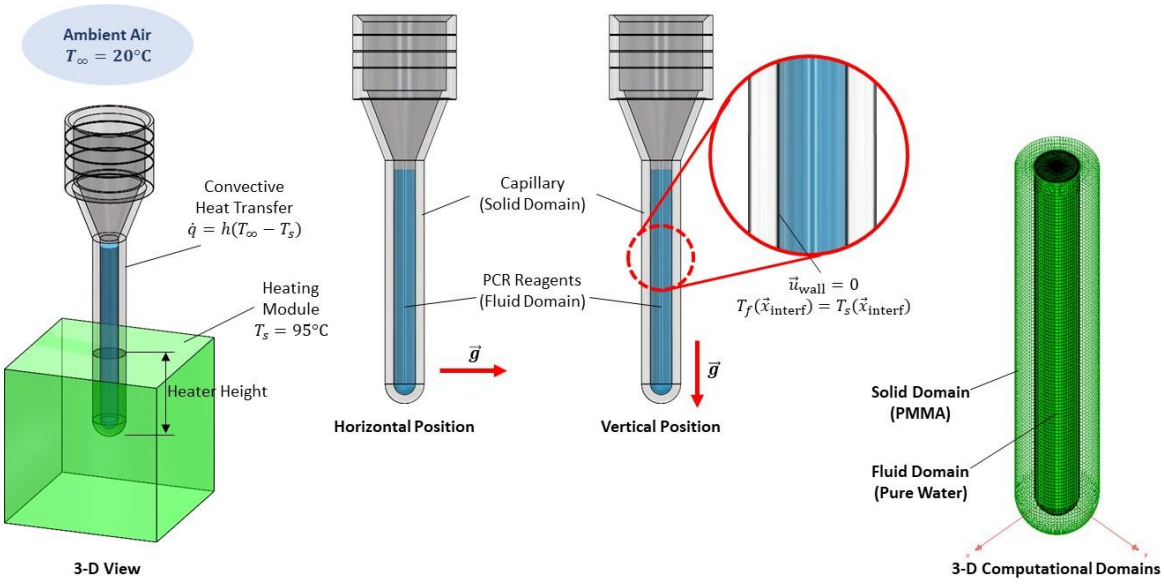

Fig. 23. 3-D model for the capillary tube, boundary conditions, and its computational domains

cPCR are placed in the vertical position, but the gravitational acceleration is assumed to be applied in the direction of +Y and -Z, respectively. The boundary conditions are employed as described in Chapter 2.2, and additionally considered as follows:

- **Temperature boundary conditions for Horizontal cPCR**
  - Bottom Resistive Heater Module: 95 ℃
  - Convective Heat Transfer Coefficient: $26.7\ \mathrm{W/(m^2K)}$ [48]
  - Temperature of Ambient Air: 20 ℃
- **Temperature boundary conditions for Vertical cPCR**
  - Bottom Resistive Heater Module: 95 ℃
  - Convective Heat Transfer Coefficient: $11.5\ \mathrm{W/(m^2K)}$ [35, 36, 44]
  - Temperature of Ambient Air: 20 ℃

Structured, multi-region domain meshes are generated for both the fluid and the solid regions. A grid independence study is carried out to ensure the results are converged, as represented in Chapter 3.4. The results are grid-independent when the fluid and solid domains are of 224,576 and 123,948 cells, respectively.

5.4 Results and Discussion

From the experiment, it can be known that the heating temperature for the horizontal cPCR should be maintained to be about 95 ℃ when the capillary tube is heated from its one-end. There is a difference between the controlled temperature from the heating block and the reaction temperature from the capillary tube. The feedback temperature control system intentionally adjusts the setpoint for temperature compensation. A properly tuned PID controller maintains

the heating temperature to be of consistency with a steady-state error of ± 0.1 °C, which ensures the efficiency of amplification for the horizontal cPCR.

The performance of the reactor in the horizontal position is evaluated by detecting influenza-A (H1N1) virus nucleic acid targets. To validate the real-time horizontal cPCR system, a cPCR reactor with the same dimensions but vertically placed is evaluated and used as a reference for comparison. Stock culture samples of 1.0 $TCID_{50}$/mL containing the diluted influenza-A virus are individually tested to obtain negative control (NC) as reference.

The PCR solutions used for the experiment are made up of the reagents, such as 3 µL of a mixture of primers (Beijing Wantai Biological Pharmacy Enterprise, Ltd.) and a TaqMan probe labeled with FAM ™ at 5'end and Eclipse at the 3'end, 4 mM dNTP and 4 µL of Fast Buffer I (Mg ion buffer) (all Takara Bio Inc., Shiga, Japan), 0.4 U of AM reverse transcriptase (Promega, USA), 1 U of SpeedSTAR HS DNA polymerase (Takara), 10 µL of the purified influenza-A RNA as per above protocol, and molecular-biology grade water to a total reaction volume of 40 µL. The experiment adopts a 105-bp amplicon of the primer sequence used with influenza H1N1 template. Once the capillary tube is filled, the reagents is sealed with a layer of 10 µL sterile mineral oil (Sigma-Aldrich, St. Louis, MO, USA). The mineral oil maintains the PCR reagents stayed right inside the capillary tube without a lid due to the surface tension caused by its high viscosity.

A smartphone camera captures the images of the productions of amplicons with TaqMan probes labeled with FAM™ in real time. The amplitude of the fluorescence intensity is extracted

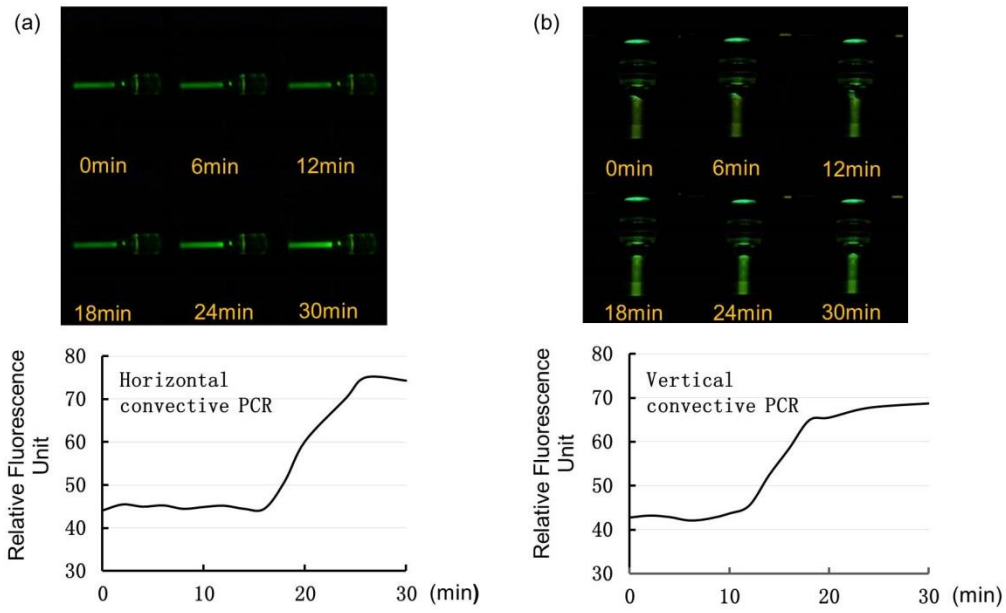

Fig. 24. Real-time cPCR with influenza A (H1N1) virus RNA template (1.0 $TCID_{50}$/mL). Fluorescence images at different amplification time and corresponding fluorescence signal intensity as a function over time for: (a) horizontal, and (b) vertical cPCR. (Figure by courtesy of Dr. Xianbo Qiu) [2]

from the respective images and analyzed using customized software. As seen in Fig. 24, fluorescence intensities of the horizontal (Fig. 24 (a)) and vertical positions (Fig. 24 (b)) are obtained in real time for 30 min. For the amplification of the horizontal cPCR, the log-linear stage lasts for about 10 min after the linear-ground stage for about 17 min; and then, it finally reaches the plateau stage at approximately 25 min, which is comparable results with that of the existing vertical cPCR. Compared with the positive test, NC does not show any significant increase in fluorescence signal intensity. The experimental data are obtained by repeating the test at least three times, and similar results are obtained.

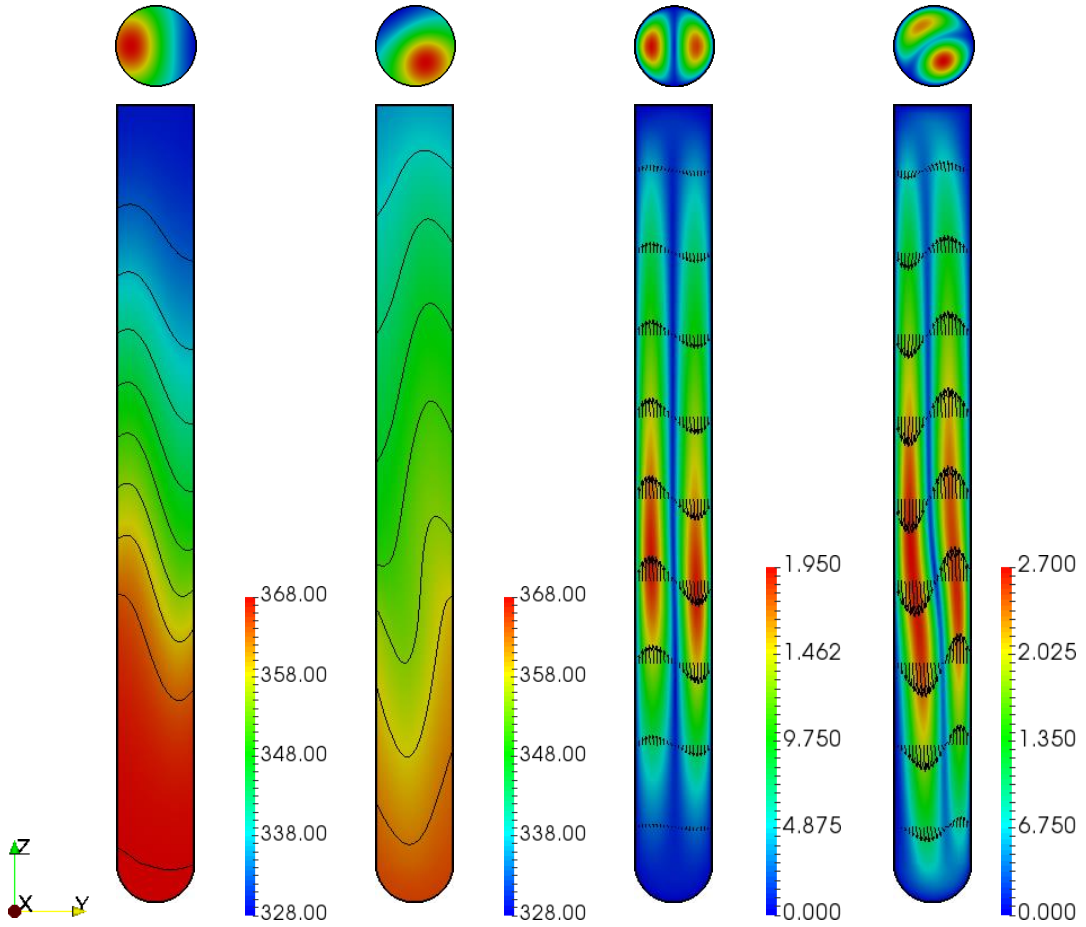

Fig. 25. Simulation results of horizontal and vertical cPCR: Temperature fields (K) of (a) horizontal, and (b) vertical cPCR; Velocity fields (mm/s) of (c) horizontal, and (d) vertical cPCR

From the results, it turns out that the amplification of the horizontal cPCR achieves similar efficiency to that of the cPCR reactor in the vertical position. As a proof of concept, the real-time horizontal cPCR system successfully detects the nucleic acid targets from H1N1 virus sample with a concentration of 1.0 $TCID_{50}$/ml (limit of detection) [49, 50]. The horizontal cPCR obtains similar results to the existing vertical cPCR, which show significantly less time taken to amplify nucleic acid with a reasonable sensitivity when comparing to the traditional PCR. As seen in Fig. 24, it can be known that the curves of the horizontal and vertical cPCR have a little

difference in intensity and rise time because the number of thermal convection cycle is uncontrolled. It turns out that the real-time horizontal cPCR has the capability of achieving the desired amplification as efficiently as the vertical cPCR does.

The numerical simulations are performed to investigate the insight into the nature of flow in the horizontal and vertical cPCR. A sample of results is presented in Fig. 25. Both cases approach the maximum temperature of 95 ℃, which is proper for the denaturation process. However, there is a stark difference in the minimum temperature of both. The top regions have the minimum temperature since flow is naturally cooled by transferring heat to the ambient air. Given that the ideal annealing process occurs in the range of 55-60 ℃, the temperature near the top region is adequate for annealing process as approximately 55 ℃ and 60 ℃ for the horizontal and vertical positions, respectively. It is observed that the maximum velocity of the vertical cPCR is approximately 1.4 times faster than that of the horizontal cPCR. The result is caused by the buoyancy force of the horizontal cPCR generated much stronger than that of the vertical cPCR. The reason for the stronger buoyancy force of the vertical case is because of its deeper depth of the reactor, which affects the strength of the hydrostatic pressure.

From Figs. 25 (c) and (d), it can be found that the horizontal convection has a shape of a perfect oval loop, whereas the vertical convection is slightly twisted. Due to the stronger convective heat transfer inside the reactor in the vertical position, more heat is transferred from the bottom to the top, causing the fluid temperature near the top to be slightly higher than that of the horizontal convection. For the same reason, the near-bottom temperature in the vertical position is slightly lower than in the horizontal position.

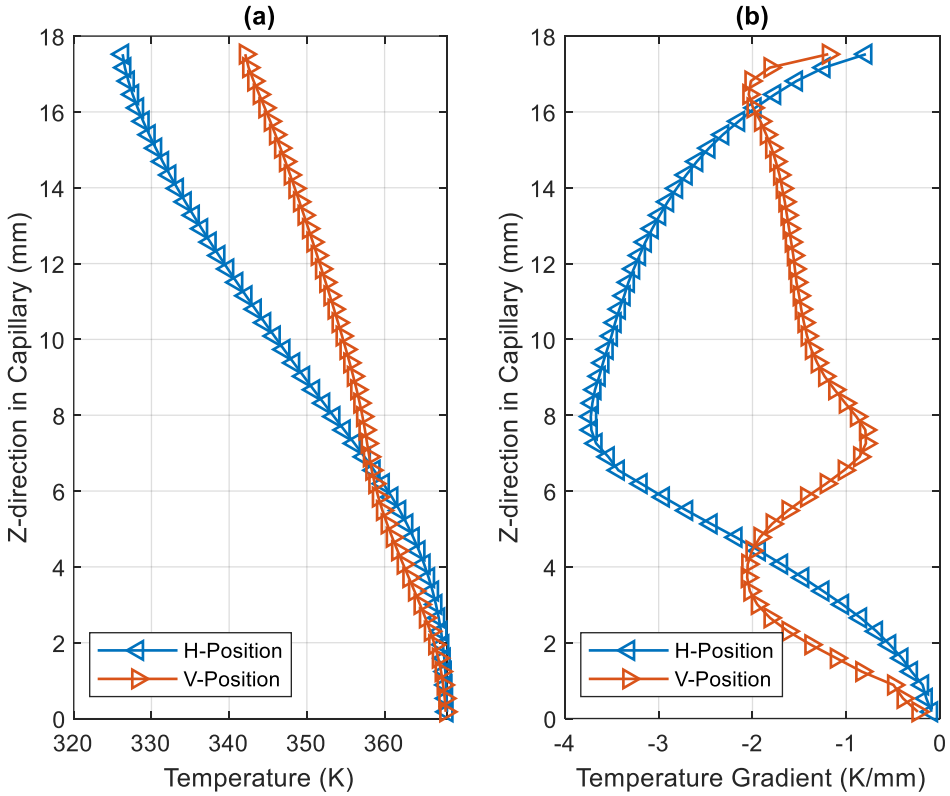

Fig. 26. Flow temperature and its gradient of the horizontal and vertical convections along the z-direction

Fig. 26 represents the fluid temperature and its gradient along the z-direction, which corresponds to the direction of the height of the capillary tube. Beyond a certain point (i.e., z_{cr}) in the z-direction, which is about half of the total fluid height, the vertical convection (solid line with the right-pointing triangle) has the temperature higher than the horizontal convection (solid line with the left-pointing triangle) does. In contrast, the temperature of the vertical convection is lower than that of the horizontal convection in the region of $z < z_{cr}$. Except for the regions of the ends of the reactor, the temperature gradient of the horizontal convection is higher than that of the vertical convection, as shown in Fig. 26 (b).

Compared with the experimental results in Fig. 24, the numerical results qualitatively agree with them as well. As aforementioned, the vertical convection has a higher maximum

velocity; hence, it takes a shorter time for the vertical cPCR to complete circulating in one oval loop. Note that one loop is qualitatively equivalent to one PCR cycle. Therefore, the amplification carried by the vertical cPCR is yielded to be faster than by the horizontal one, which explains why the RFU signal of the vertical convection starts to rise earlier than that of the horizontal convection. However, when seeing the RFU signals in the stage of the plateau, both cases have very close magnitude, which is approximately 70 and can be considered as successful amplification. It seems that lower flow velocity reduces the contribution of convective heat transfer that would help maintain temperature efficient for PCR thermal cycling processes. The spatial temperature distribution of the vertical convection slightly deviates from the ideal temperature profile for DNA amplification. It partly explains the reason for the RFU signals of both cases that have the same magnitude in the stage of the plateau.

All in all, the horizontal case produces very flow circulation similar to the vertical case. Although the horizontal case needs a slightly longer time for the efficient DNA amplification, it has the temperature fields more suitable for DNA amplification than the vertical case due to the speed of the convection. Therefore, it proves that the real-time horizontal cPCR assures the performance equivalent to the cPCR device in the vertical position.

5.5 Conclusions

A real-time cPCR device has been successfully developed to induce horizontal convection. For the potential use as a POC application, the system was compact and enabled one-end heating and in situ fluorescence monitoring. The actual reactor of the cPCR system was computationally modeled to investigate insight into thermal convection. Through the analysis, it was confirmed that the rapid thermal cycling made the horizontal cPCR reactor capable of reducing the required amplification time.

We implemented CFD simulations for the horizontally/vertically positioned reactors, which used the conjugate momentum and heat transfer model, and the species transport model. The inherent characteristics of thermo-fluid were analyzed in depth. We evaluated the performance of the real-time horizontal cPCR reactor by detecting influenza A (H1N1) virus samples with a concentration of 1.0 $TCID_{50}$/mL for 30 min. The experimentations were effectively verified by the CFD simulations. It was demonstrated that the horizontal cPCR had performance almost equivalent to the vertically positioned cPCR reactor.

In the next chapter, a more sophisticated design methodology will be introduced for the double-heater cPCR reactor. Based on the single heater reactor design methodology covered in Chapter 4, we additionally consider surrogate models and optimization to develop a doubling heater reactor. With the improved methodology, we will show that the result is very accurate and cost-effective as POC applications.

CHAPTER 6

SURROGATE-ASSISTED DESIGN OPTIMIZATION FOR DOUBLE-HEATER CPCR REACTORS

6.1 Overview

Design optimization is the process of finding the best design parameters from numerous possible options. It is advantageous due to the high flexibility to find optimality before physical modeling [51]. A combination of high-fidelity analysis tools and optimization packages can make a great result with the highest accuracy. However, a direct method of CFD optimization requires tremendous computational efforts, which leads to an increase in costs and time [52, 53]. Therefore, an indirect method of CFD optimization is needed to avoid the problems as aforementioned.

One possible method is to make surrogate models after implementing numerous CFD simulations as planned based on DOE. A surrogate model is an approximation that evaluates in a cheaper and faster way, replacing a known expensive computational model [52]. Surrogate-assisted optimization is a kind of indirect methods that enables to find optimal designs fast [54, 55].

As an extension of the study in Chapter 4, the design optimization is carried out to find a double-heater reactor that assures the best performance. A double-heater cPCR reactor is used as a baseline, as shown in Fig. 27. A resistive heater is inserted into a heating module made of aluminum, maintaining a constant temperature applied to the bottom and top of the cylindrical tube by the aid of thermostats. The cylindrical tube is enclosed by an insulator to circumvent heat loss. Artificial neural network (ANN) is used to develop a surrogate model. Numerous

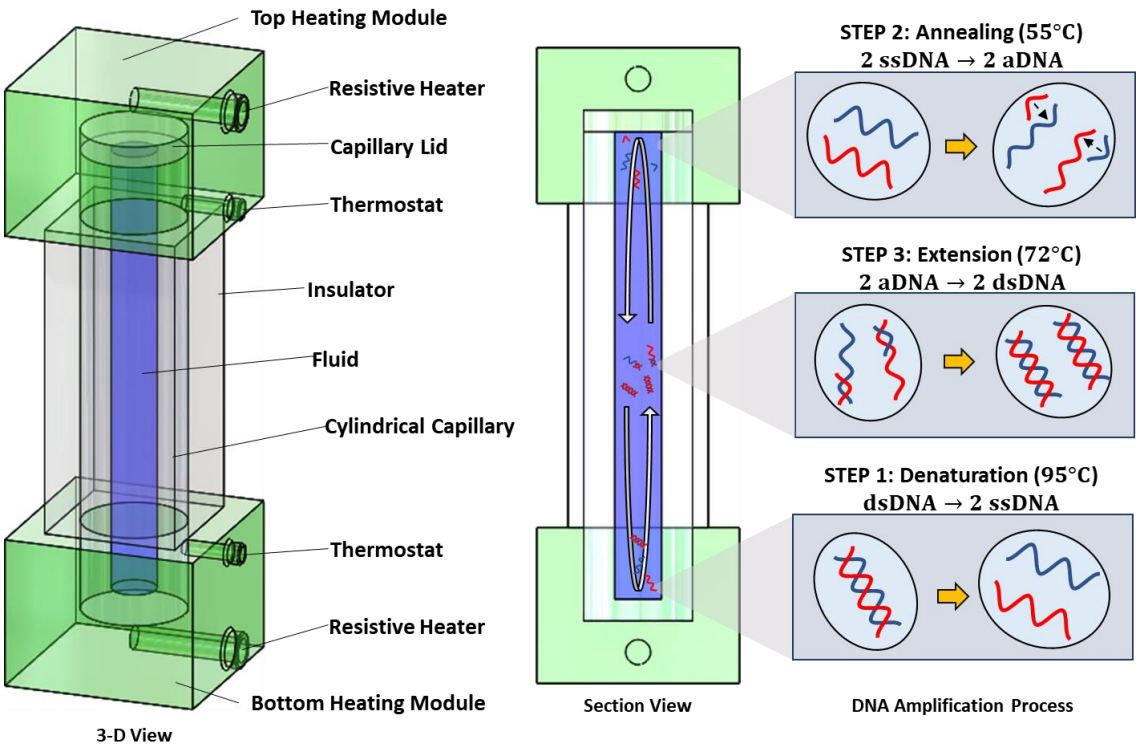

Fig. 27. Flow temperature and its gradient of the horizontal and vertical convections along the z-direction

designs of a double-heater reactor are regarded based on DOE and simulated using CFD to train the neural network with the Bayesian algorithm. Finally, design optimization is implemented to find the best performing double-heater cPCR reactor using surrogate models developed.

6.2 Mathematical Models

A double-heater cPCR can be computationally simulated using the mathematical models already discussed in Chapter 2. The simulation is carried out using in-house codes that employ the conjugate momentum and heat transfer model and the species transport model. Initially, the steady-state Rayleigh-Bénard problem is solved for the four cylindrical capillary tubes with

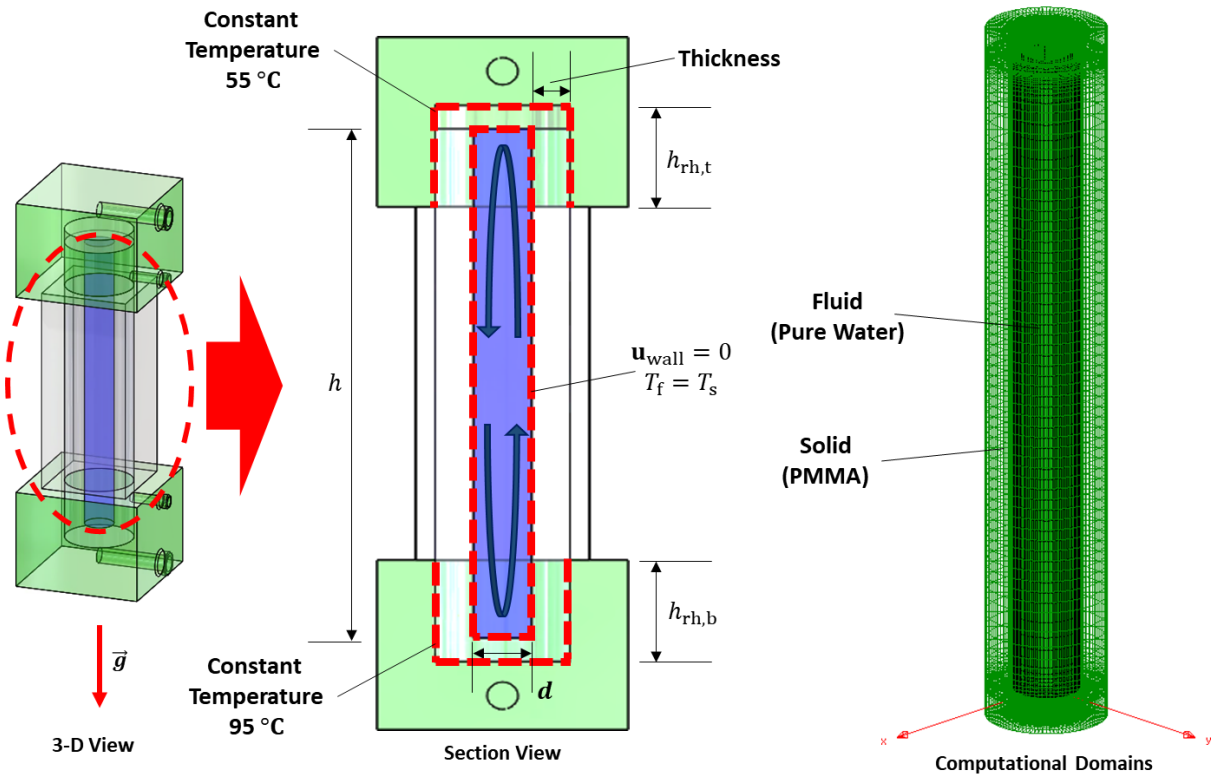

Fig. 28. Boundary conditions of double-heater reactor and its computational domains

different heights. The boundary conditions described in Chapter 2.2 are employed, as shown in Fig. 28, and additionally described as follows:

- **Temperature boundary conditions**
  - Top Resistive Heating Module: 55 ℃
  - Bottom Resistive Heater Module: 95 ℃
  - Outer Surface of the Cylindrical Capillary Tube: $\partial T/\partial \hat{\mathbf{n}} = 0$

Then, concentrations of the respective DNA species are computed using the unsteady species transport model. The initial/boundary conditions are employed, as described in Chapter 2.3. Additional considerations are made as follows:

- **Initial conditions**
  - Concentrations for dsDNA: 100 (number basis)
- **Constant Parameters**
  - Diffusive Coefficient: $10^{-11}\ m^2/s$
  - Reaction Rate for Denaturation: $0.1\ s^{-1}$
  - Reaction Rate for Annealing: $0.1\ s^{-1}$
  - Reaction Rate for Extension: $0.05\ s^{-1}$
  - Standard Deviation for Denaturation: 5.0 ℃
  - Standard Deviation for Annealing: 5.0 ℃
  - Standard Deviation for Extension: 2.5 ℃
  - Ideal Reaction Temperature for Denaturation: 95 ℃
  - Ideal Reaction Temperature for Annealing: 55 ℃
  - Ideal Reaction Temperature for Extension: 72 ℃

The DNA species concentration fields are volume-averaged using Eq. (12), varying with time. This volume-averaged concentration is deemed as the number of DNAs dissolved in the solution. Once the dsDNA concentration is computed via CFD simulation, the doubling time is estimated using Eq. (14). The CFD simulation is terminated if the amplification reaches the pre-specified termination time (1,800 s).

6.3 Design Space Investigation

Various design candidates are considered to investigate design space for the double-heater cPCR reactor. A total of 625 design candidates are obtained by combining sets of values of the selected parameters: diameter, aspect ratio, heater heights (top and bottom). Table 12 represents the information of the parameters used for design space investigation:

TABLE 12

VARIOUS QUANTITIES IN DESIGN VARIABLES

Design Parameters	Variables	Unit	Lower Limit	Upper Limit	Step Size
Diameter	d	mm	1.3	1.7	0.1
Aspect Ratio	h/d	-	6.0	10.0	1.0
Top Heater Height	$h_{\mathrm{rt,t}}$	%	7.0	15.0	2.0
Bottom Heater Height	$h_{\mathrm{rt,b}}$	%	7.0	15.0	2.0

The sets of values of the parameters are determined as commonly used for PCR studies as presented in the literature. All design candidates are grouped by the diameter from G1 to G5 to consider 125 candidates per group sorted by design parameters in the order of the bottom heater height, the top heater height, and the aspect ratio. The design number is assigned to all double-heater cPCR reactors in the same manner. Once the design space is investigated using CFD simulations, the performance is individually quantified for all candidates. The data obtained from CFD simulations are utilized to develop surrogate models using ANN.

6.4 Artificial Neural Network Build-Up

Surrogate models are developed by customizing MATLAB Neural Network Toolbox to ensure higher accuracy of the approximation. A single neuron model is used, consisting of three different functions: synaptic weight, summing junction, and transfer function. Initially, the model takes inputs and weights them in the synaptic weight level. Then, the weighted inputs are summed up with a bias; the product is called ‘net inputs’ (the summing junction level) [56]. In

the final level, the transfer function takes the net inputs to calculate the output of the single neuron. This can be mathematically expressed as follows [57, 58]:

$$y(\mathbf{p}) = f\left(\sum_{i=1}^{R} w_i p_i + b\right) \tag{18}$$

where, p is the vector of inputs with R elements, w is the weighted value, b is the bias, and f is the transfer function. A combination of neurons can be made up of a neural network. Fig. 29 depicts the neuron architecture customized for this problem, which consists of one input layer, two hidden layers, and one output layer. In the input layer, the parameters related to the cPCR reactor are taken as inputs, such as the diameter, aspect ratio, bottom heater height, and top heater height. For the fast computation, all single neuron models in the hidden layers utilize the hyperbolic tangent sigmoid transfer function defined as [59]:

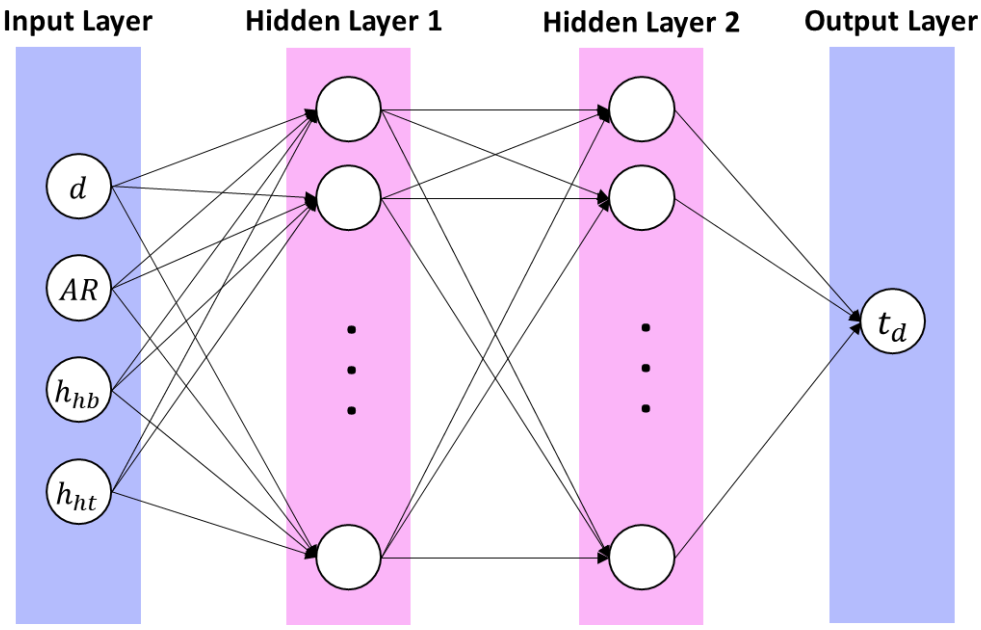

Fig. 29. Customized feed forward network with two hidden layers

$$f(y) = \frac{2}{(1 + e^{-2y})} - 1 \tag{19}$$

The output layer has one single neuron with a linear transfer function to estimate one output parameter, which is the DNA doubling time. The Bayesian regularization backpropagation is adopted for the network training algorithm, which depends on the probabilistic interpretation of network parameters [60, 61]. For the Bayesian regularization process, Levenberg-Marquardt optimization updates weights and bias to minimize a linear combination of squared errors and weights [62, 63].

6.5 Optimization Strategies

Optimization is a technique that finds a set of design variables to obtain the optimal condition of a system. In simple cases, an optimization problem is formulated to minimize or maximize a function by finding input values that give an optimal solution within given ranges. The general form of optimization can be formulated as follows [64]:

$$\begin{aligned} &\text{Minimize} && f(\mathbf{x}) \\ &\text{Subject to} && G_i(\mathbf{x}) \le 0, \quad (i = 1, 2, \ldots, N) \\ &&& G_i(\mathbf{x}) = 0, \quad (i = N+1, N+2, \ldots, M) \end{aligned} \tag{20}$$

where, $\mathbf{x}$ is the vector of design variables, $f(\mathbf{x})$ denotes the objective function, and $G(\mathbf{x})$ is the constraint vector with a length of N and M for inequality and equality, respectively. There are numerous algorithms to resolve optimization problems formulated as Eq. (20). Here, we suggest two representative algorithms to solve complicated nonlinear optimization problems: genetic algorithm (GA), and sequential quadratic programming (SQP).

Genetic Algorithm (GA)

The GA is a stochastic and heuristic method inspired by biological evolution based on natural selection. It produces offspring that have the information on the characteristics of the parents and will hand down to the next generation. In the GA, design variables are expressed as a chromosome, a string of binary values which are called Gene; a population is a group of chromosomes or a subset of solutions in the current generation.

The process considers five phases for the evolutionary generation: initial population, fitness function, selection, crossover, and mutation [65, 66]. The GA starts with the initial population phase. The initial population is randomly created as initialization of a set of individuals. The population should be of high diversity at the first generation to globally explore design space [64]. In the next step, the fitness function scores all individuals at the current generation to find the chromosomes with a high probability of being near the optimality [65, 67]. In the selection step, the fittest chromosomes are selected for reproduction for the next generation based on the fitness score. The selected two pairs of chromosomes are used to hand down the characteristics of the genes of parents. The selection process is significant since the functions specify how to choose the parents. The GA can adopt several schemes for the selection process, such as linear and nonlinear ranking, k-tournament selection, roulette wheel selection, and so on. Crossover is a process for creating offspring by exchanging some parts of the parents' dominant genes. A crossover point is randomly selected from within the genes; it continues to exchange the genes of parents until the crossover point is reached [66]. In the mutation step, a new generation may have some of their genes mutated with a low random probability. Recalling the gene is binary numbers, some of the genes of a chromosome can be flipped by the mutation. The GA terminates the process if satisfying the stopping criteria in

which the current generation is not significantly different from the previous generation; that is, lack of improvement in the best solution will terminate the process. Otherwise, the process keeps repeating selection, crossover, mutation, and fitness scoring to create the next generations. The pseudo code of the GA is presented as follows [65]:

TABLE 13

PSEUDOCODE OF GENETIC ALGORITHM

```
START
GENERATE INITIAL POPULATION
SCORE FITNESS
REPEAT
     SELECTION
     CROSSOVER
     MUTATION
     SCORE FITNESS
UNTIL THE CONVERGENCE OF POPULASION
END
```

Sequential Quadratic Programming (SQP)

The SQP is a method for solving continuous and smooth nonlinear optimization problems. It evaluates functions and derivatives to find the optimal solution with sufficiently high precision. It is required that the objective functions and constraints must be continuously differentiable because the SQP is the derivative-based optimization. As a strategy of the consideration of constraints into the objective function, the Lagrangian function is utilized as follows [64]:

$$L(\mathbf{x}, \boldsymbol{\lambda}) = f(\mathbf{x}) + \sum_{i=1}^{M} \lambda_i G_i(\mathbf{x}) \tag{21}$$

where, $\boldsymbol{\lambda}$ indicates the vector of multipliers, λ_i.

The quadratic subproblem can be formulated based on the Lagrangian function. The SQP requires to compute the derivatives of the Lagrangian function in order to resolve the quadratic programming (QP) sub-problem, which is defined as [64]:

$$\begin{aligned} &\text{Minimize} && \frac{1}{2}\mathbf{d}^T \mathbf{H}_k \mathbf{d} + \nabla f(\mathbf{x}_k)^T \mathbf{d} \\ &\text{Subject to} && \nabla G_i(\mathbf{x}_k)^T \mathbf{d} + G_i(\mathbf{x}_k) \geq 0, \quad (i = 1, 2, \ldots, N) \\ & && \nabla G_i(\mathbf{x}_k)^T \mathbf{d} + G_i(\mathbf{x}_k) = 0, \quad (i = N+1, N+2, \ldots, M) \end{aligned} \tag{22}$$

where, $\mathbf{d}$ is the vector of the search direction, $\mathbf{H}$ is the Hessian matrix of the Lagrangian function, $\nabla f(\mathbf{x})$ denotes the gradient of the objective function. The QP sub-problem aims to find the appropriate quantities of the vector $\mathbf{d}$ to be used as the search direction at the *k*-th iteration of the main problem. The solution of the QP subproblem can be obtained by implementing algorithms such as the Newton method, quasi-Newton method, conjugate gradient, gradient projection, etc.

Once the solution of the sub-problem is obtained, the main problem level of the SQP algorithm determines the next iteration point of the vector of design variables using equation as follows [68]:

$$\mathbf{x}_{k+1} = \mathbf{x}_k + \alpha_k \mathbf{d}_k \tag{23}$$

where, α_k denotes the step-length at the *k*-th iteration. Note that the proper size of the step-length can be determined using a line-search method, such as backtracking, bisection, and so on. The SQP is terminated if the conditions meet the first-order optimality, $L(\mathbf{x}_k, \boldsymbol{\lambda}_k) \approx 0$.

TABLE 14

PSEUDOCODE OF SEQUENTIAL QUADRATIC PROGRAMMING

```
START
SET k := 1
REPEAT
    COMPUTE DERIVATIVES (HESSIAN, GRADIENT)
    REPEAT: SOLVE THE QP SUB-PROBLEM
        SET t := 1
        COMPUTE THE QP SEARCH DIRECTION P_t
        COMPUTE THE STEP LENGTH α_t
        UPDATE d_{t+1} = d_t + α_t P_t
        INCREMENT t
    UNTIL QUADRATIC FUNCTION APPROXIMATES TO ZERO
    COMPUTE THE STEP LENGTH α_k
    UPDATE x_{k+1} = x_k + α_k d_k
    INCREMENT k
UNTIL IT MEETS THE 1ST-ORDER OPTIMALITY ∇L ≈ 0
END
```

Hybrid GA-SQP Algorithm

The GA makes a better exploration of design space with derivatives free, while it is slow in convergence and does not guarantee optimality. The SQP features its fast convergence speed but is prone to be trapped in local minima [69]. If the problem is as complicated as there are more than two local minima, a hybrid algorithm can be considered to take advantage of the merits of the respective algorithms to be combined. The hybrid algorithm is a combination of global and local strategies; it gives deterministic global optimization solutions. More than two

algorithms are combined into one to take advantage of their strong points. In this study, the genetic algorithm (GA) and sequential quadratic programming (SQP) are employed for the global exploration of the design space and the deterministic local optima, respectively. The reason for the combination is that the hybrid GA-SQP algorithm avoids being trapped in local minima and converges solutions quickly. We utilize MATLAB built-in optimization functions – `ga()`, and `fmincon()` – to implement the hybrid GA-SQP algorithm [66, 70]. The simple two-step method starts the GA first with high tolerance options for optimality. Few generations are produced for global optimality exploration; the GA gives a solution, not but near the optimum. The hybrid algorithm switches to the SQP, continuing the optimization by using the solution obtained from the GA as an initial guess. As a result, we can rapidly obtain a solution for global deterministic optimization.

6.6 Design Formulation for Optimization

Surrogate-assisted optimization is implemented to find the optimal design of the cPCR reactor. The design problem is formulated as follows:

$$\begin{aligned}
&\text{Minimize} && t_d \\
&\text{Find} && \mathbf{x} = \{d,\ AR,\ h_{\mathrm{rh,t}},\ h_{\mathrm{rt,b}}\} \\
&\text{subject to} && \\
& && 1.3 \leq d \leq 1.7 \\
& && 6.0 \leq AR \leq 10.0 \\
& && 7.0 \leq h_{\mathrm{rh,t}} \leq 15.0 \\
& && 7.0 \leq h_{\mathrm{rh,b}} \leq 15.0
\end{aligned}$$

The objective function is determined to minimize the doubling time to find the best performance of the reactor design. The design variables are the diameter, aspect ratio, top heater height, and the bottom heater height. Box constraints are applied to prevent the optimizer from

finding the solutions extrapolated beyond the data samples that we used for the surrogate models. It is expected that the problem has a complicated design space. Therefore, two different algorithms are considered for an optimization strategy. We build the hybrid GA-SQP algorithm and resolve the design optimization by using MATLAB built-in "`ga()`" genetic algorithm for the global minima and "`fmincon()`" sequential quadratic programming (SQP) for the local minima as described in the previous chapter [66, 70].

6.7 Surrogate Model Development Process

A simple process for surrogate models is established by using the methods as described in the previous chapters, as shown in Fig. 30. The data obtained from CFD simulations (total of 625 samples) are initially provided to process for sample elimination. The CFD data is processed under specific conditions. Three different sets of data should satisfy the respective conditions as follows:

1) Conditions for data set 1: the doubling time should be positive and less than 1,500 sec – relatively a large number of samples are remained.
2) Conditions for data set 2: the doubling time should be positive and less than 200 sec – the number of samples is between that of Condition 1 and 2.
3) Conditions for data set 3: the doubling time should be positive and less than 60 sec – relatively a small number of samples are remained.

The values of interest are positive, not far deviated from the typical values of the doubling time (approximately 30-60 sec) obtained from the other PCR devices, thereby creating Condition 3 [1]. The reason for Condition 1 is that the computation model terminates the DNA amplification if it reaches 1,500 sec. It is considered a worthless candidate in amplification if the doubling time is computed to be greater than the termination time (1,500 sec). To investigate

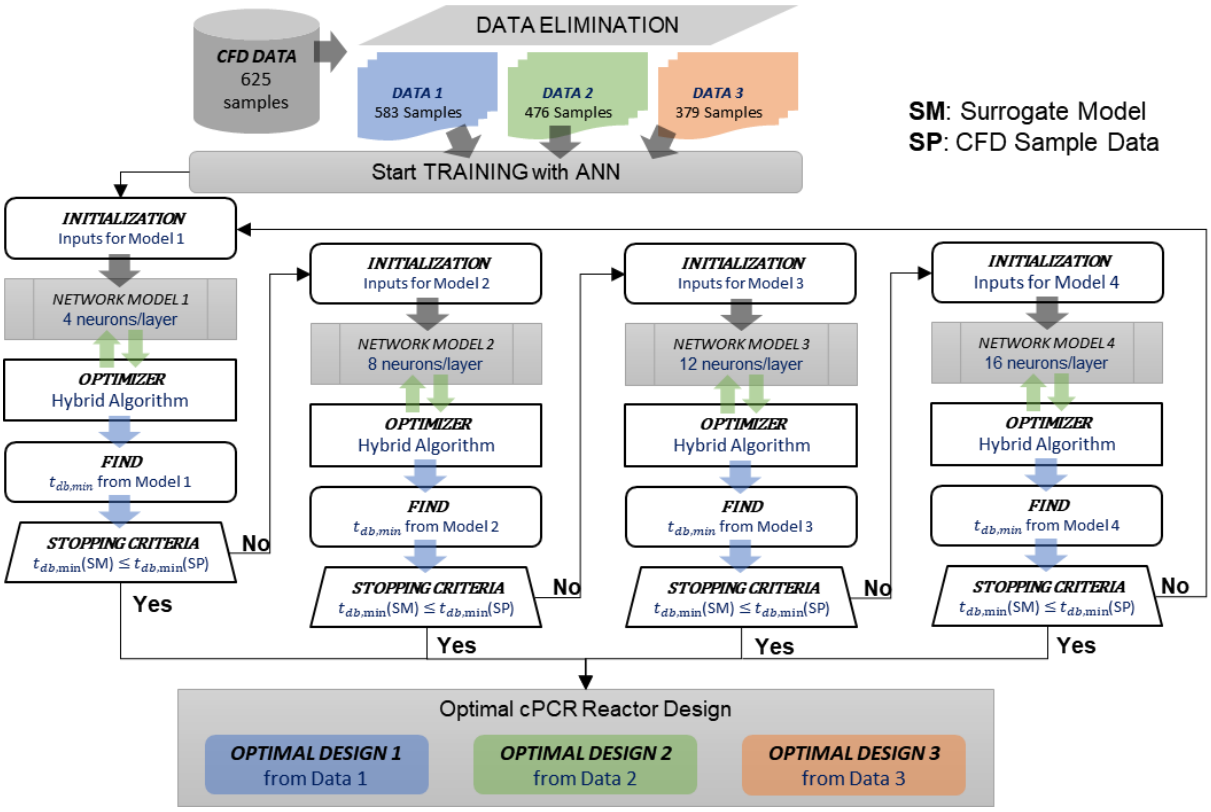

Fig. 30. Process for the development of highly accurate surrogate models

how the number of samples affects the model accuracy, another data set is produced from the original CFD data under Condition 2.

Each set of data makes distinct surrogate models. A set of data is transmitted to the network training stage. The number of neurons is one of the significant factors that determine the model accuracy and computation speed. A lower accurate surrogate model can be developed if fewer neurons are utilized in the hidden layers, whereas overfitting is caused with excessively numerous neurons; hence, four different network models are adopted for the training, which uses 4, 8, 12, and 16 neurons per hidden layers, respectively. Network models produce surrogate models after training. The process starts training the network model 1; the optimizer that uses a hybrid algorithm finds the minimum doubling time from the respective network models. If the

minimized doubling time is gr eater than or equal to the best one from the CFD sample data, the process abandons the network model, initializes the inputs, and trains the network model 2. So, it does for the network models 3 and 4. The process will repeat itself by going back to the initialization step for the network model 1 if the network model 4 does not meet the stopping criterion. If any of the network models satisfy the criterion for stopping, the corresponding reactor design is determined to be appropriate. The process initially goes with the data set 1 and repeats it for the data sets 2 and 3 in order. Once the appropriate reactor designs are obtained based on the data sets 1, 2, and 3, respectively, a comparison is made to find the best one of the three.

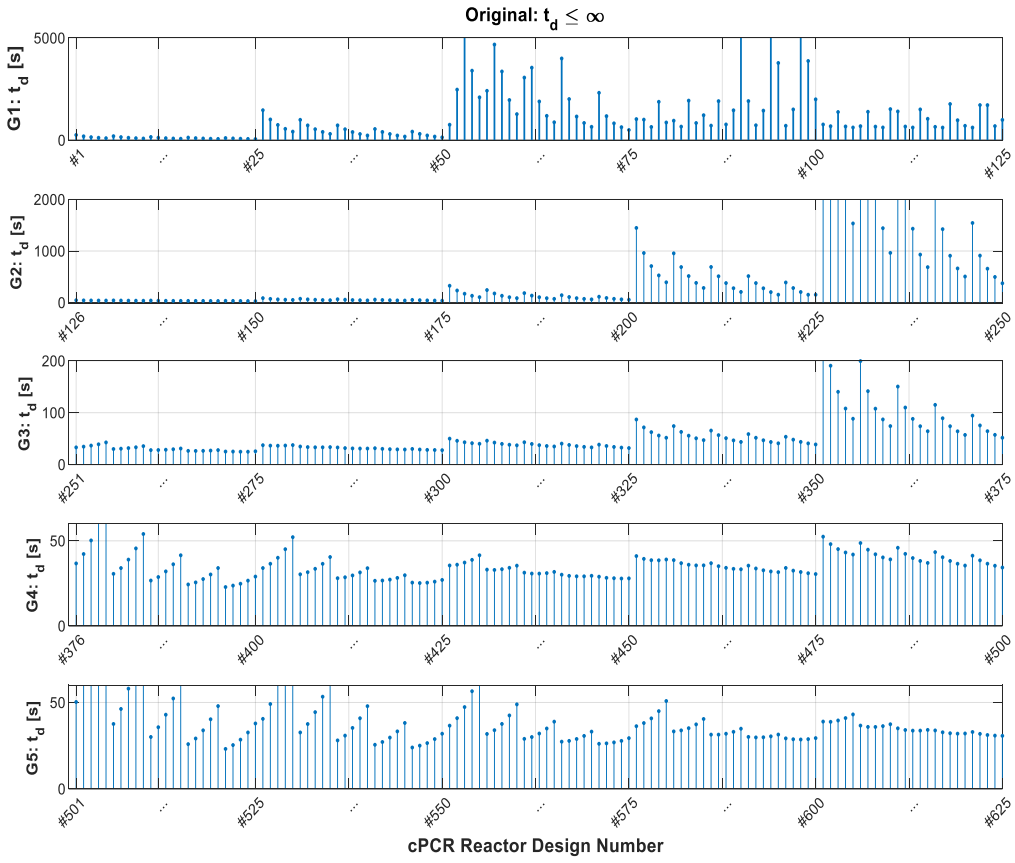

Fig. 31. Doubling time of all design candidates as performance evaluation

6.8 Results and Discussion

The design space is investigated by implementing CFD simulations (Phase I and II, as described in Chapters 2.2 and 2.3) for a total of 625 design candidates. The performance of all candidates is evaluated, as presented in Fig. 31. The corresponding results can be found in detail, as presented in Tables C-1 to 7. Some of the candidates have the unattractive performance to be used as POC applications, but most of them show typical performance in doubling time. Fig. 32 shows the contour plots for the velocity and temperature of the candidates arbitrarily selected from the respective groups.

Design #101, as seen in Fig. 31, represents the cases of poor performance due to no flow convection inside of the reactor. It appears that heat is transferred in the form of conduction, resulting in no temperature gradient on the XY plane. Even though the temperature is formed appropriate for DNA thermal cycling processes over the entire area, DNA amplification proceeds very slowly. The doubling time is estimated as very high as 766.9 sec. Design #211 generates a small, weak single convection loop of which the size is equivalent to a half of the capillary tube. Although the reactor induces a small convection loop near the bottom, the heat is transferred as conduction above it. It results in the low performance as the doubling time is computed to be 690.5 sec. A fully developed single convection loop can be found in Designs #373, #455, and #614, and it can be known that the temperature gradients are sufficiently large to induce the convection. The doubling times are computed as 64.3 sec, 39.0 sec, and 33.7 sec, respectively. It is found that other candidates showing typical performance have similar velocity and temperature patterns. It seems that the maturity of convection is majorly determined by the size of the diameter, given that most of the candidates of G1 and G2 have low performance in the doubling time.

The surrogate models are developed based on the established process. It takes inputs such as the diameter, aspect ratio, top heater height, and bottom heater height, and outputs the doubling time. The candidates that have abnormally high doubling time are ruled out to ensure the higher model accuracy. Three different surrogate models were considered after eliminating candidates of which the doubling time is greater than: 1) 1,500 sec, 2) 200 sec, and 3) 60 sec. The elimination results are shown in Fig.33.

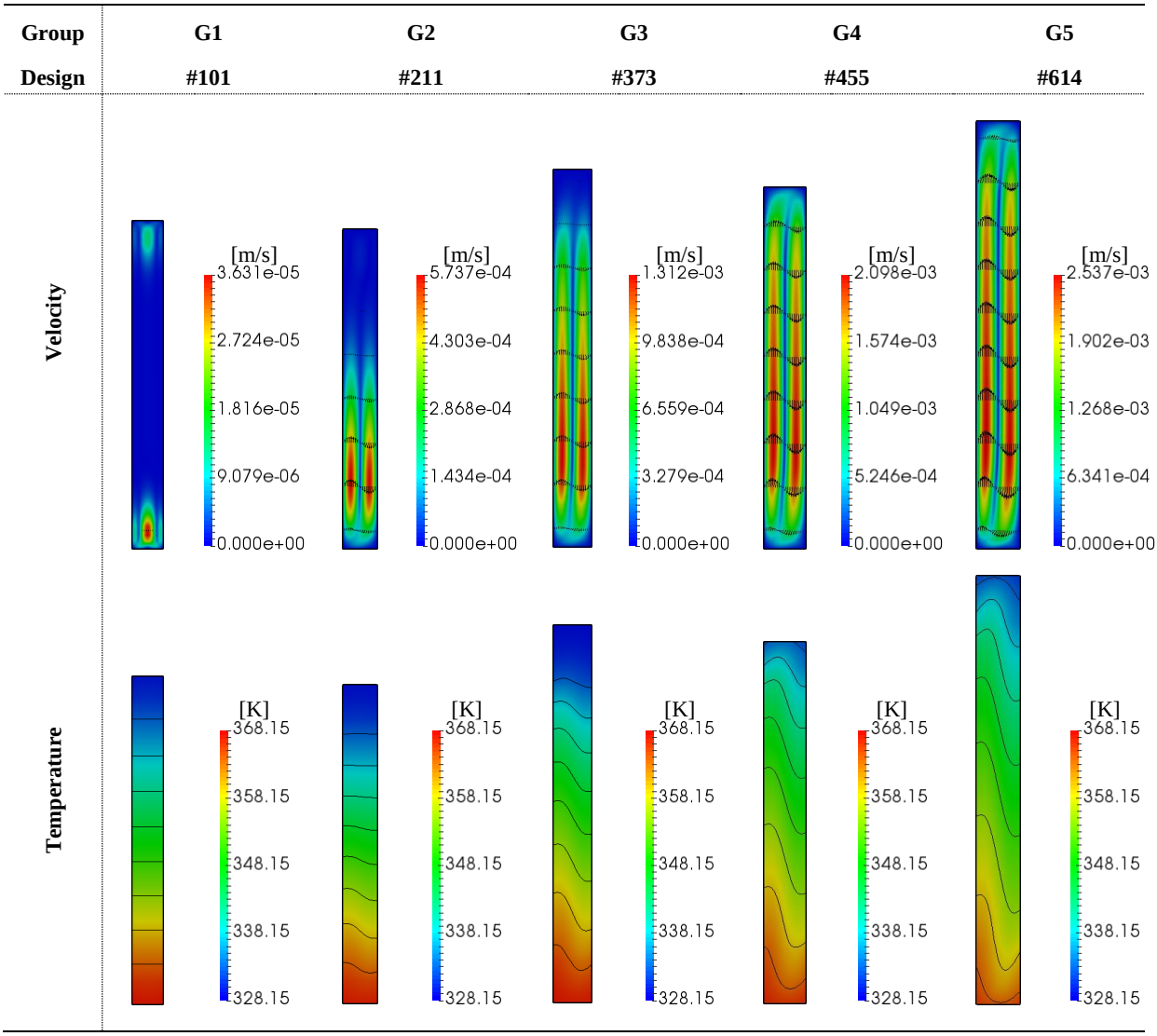

Fig. 32. Contour plots of velocity and temperature for the arbitrarily selected cases

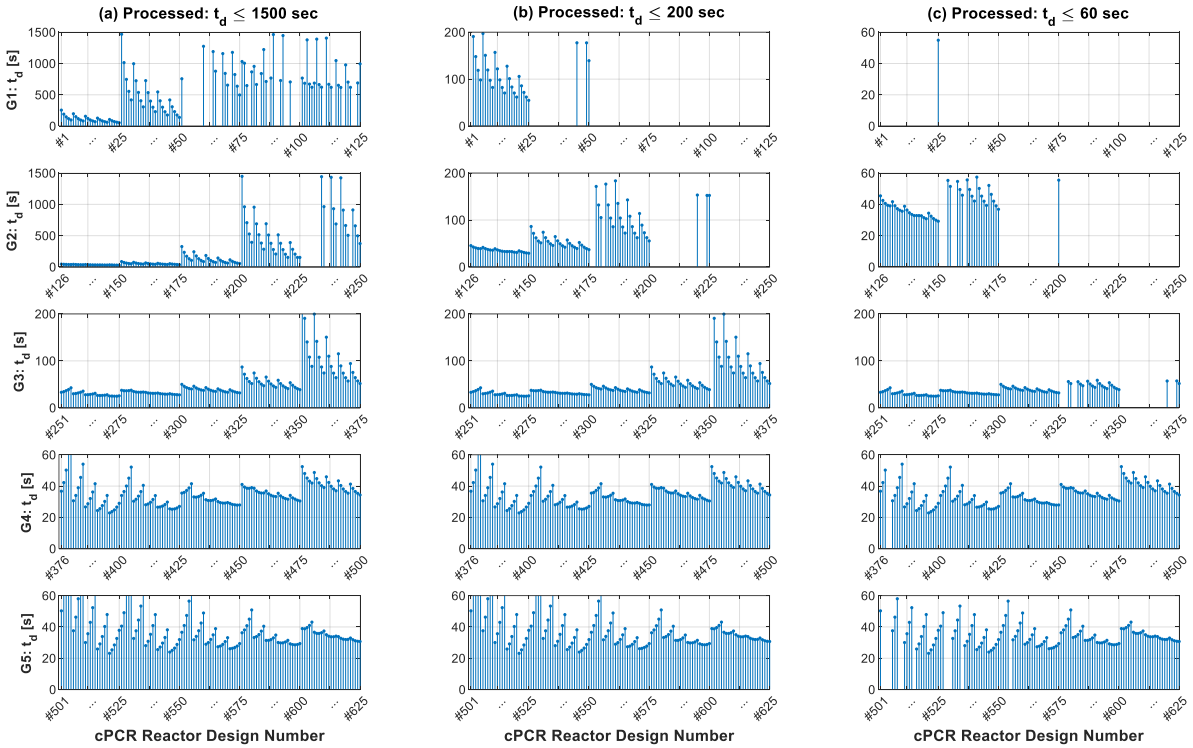

Fig. 33. Candidate elimination, abiding by three different rules: (a) doubling time ≤ 1,500 sec, (b) doubling time ≤ 200 sec, and (c) doubling time ≤ 60 sec

The first, second, and third columns in the figure indicate the available design candidates for the network training after applying Conditions 1, 2, and 3, respectively. That is, the design candidates in the respective column are an individual set of data to be used for the network training; hence, three distinct surrogate models will be developed as outcomes of the process. For G4 and G5, no design candidate is discarded since they do not meet any of the elimination conditions. The total number of available candidates of individual data sets are 583, 476, and 379, respectively.

The networks are trained with a different number of neurons per a hidden layer. The split ratio for training, test, validation sets is initially assigned to be 80 %, 10 %, and 10 %,

respectively, according to the Pareto principle (the 80/20 rule) [71]. The training goal is set to minimize the mean square error (MSE) [72].

The optimizer determines the best surrogate models for the data sets 1, 2, and 3 by the minimized doubling time, as shown in Fig. 34. The linear regression curves in the left side of the figure present how accurate the surrogate models are. The surrogate model 1 uses 583 samples of CFD data for network training, and it gives the best when 12 neurons per layer are applied to the hidden layer. The R^2 is yielded to be 0.99439, which is relatively low, compared with the other two models. As seen in the linear regression curve, the samples begin to be highly inaccurate for the doubling time beyond approximately 700 sec. However, it is of minor significance because the interval of interest is between 20 sec and 60 sec. The surrogate model 2 uses 476 samples of CFD data for network training, and the best number of neurons per layer is determined to be 8. The R^2 is yielded to be 0.99594. For the same reason as the surrogate model 1, the samples start to be highly inaccurate at the point where the doubling time is beyond 150 sec. The surrogate model 3 utilizes 379 samples of CFD data for network training. Since the least number of CFD data is used, the best number of neurons per layer is determined to be 4. The R^2 is relatively high as 0.99938. The performance history in the right of the figure shows how the network training algorithm attains the best performance. The best validation performance of the surrogate models 1, 2, and 3 is calculated to be 168.23, 18.0097, and 0.064431, respectively. The performance history of the training, validation, and test could be a factor that indicates over- or underfitting.

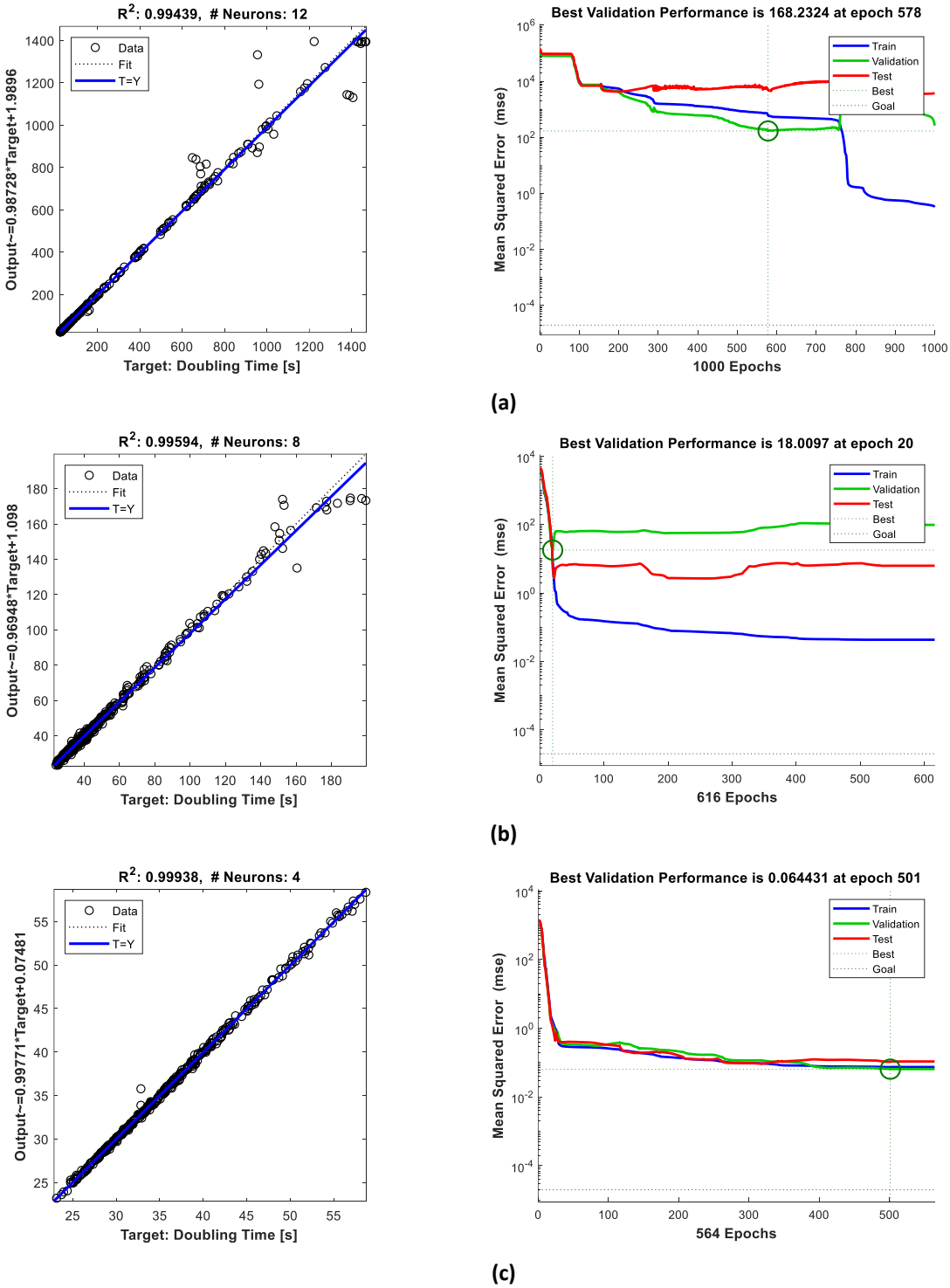

Fig. 34. Linear regression curves (left) and performance history (right) as training results: (a) doubling time ≤ 1,500 sec (583 samples), (b) doubling time ≤ 200 sec (476 samples), and (c) doubling time ≤ 60 sec (379 samples)

TABLE 15

OPTIMIZATION RESULTS OF ALL SURROGATE MODELS

Design Parameters	Unit	Model 1	Model 2	Model 3	Best Sample (as reference)
Diameter	mm	1.6209	1.6033	1.6475	1.6000
Aspect Ratio	-	6.0000	6.0000	6.0000	6.0000
Top Heater Height	%	15.000	15.0000	15.0000	15.0000
Bottom Heater Height	%	7.0197	7.0000	7.0000	7.0000
Doubling Time (Surrogate Estimated)	sec	21.7780	21.4264	21.7473	N/A
Doubling Time (CFD Estimated)	sec	20.1823	20.1977	20.2479	22.8519
Relative Percentage Error	%	7.9064	6.0834	7.4052	N/A

Table 13 represents the optimization results of all surrogate models and the verification using CFD simulation. The doubling time of the surrogate model 1, 2, and 3 is estimated to be 21.78 sec, 21.43 sec, and 21.75 sec, respectively. They are even lower than the best one from the CFD data samples that we used for the network training. The doubling time estimated by the surrogate models is validated by CFD simulations, resulting in 20.18 sec, 20.20 sec, and 20.25 sec, respectively. To confirm the model accuracy, we compare the doubling time obtained from both sources by relative percentage errors. The design candidate of the surrogate model 2 is determined to be the best, accurate result since the relative percentage error is yielded to be the least as 6.08 %.

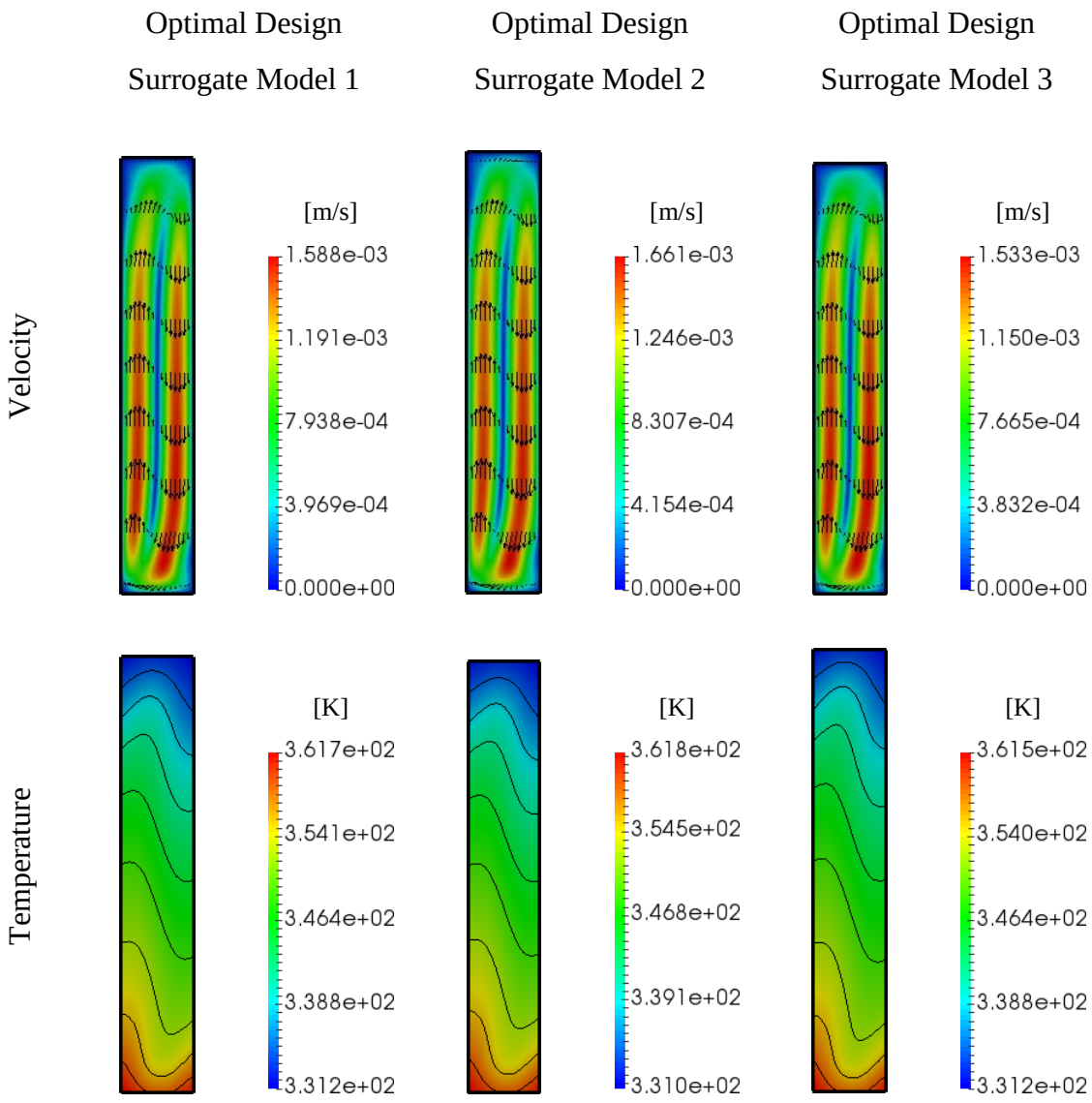

Fig. 35. Velocity and temperature contours for optimal designs of surrogate models 1, 2, and 3, respectively

Fig. 35 shows the contour plots of the velocity and temperature fields for the optimal designs from the surrogate models 1, 2, and 3. The optimal designs from the respective surrogate models have a single convection loop induced by the temperature differences between the top and bottom regions. The maximum velocity of the optimal design from the surrogate model 2 is computed to be 1.661 mm/s, which is the fastest one, compared with the others. The

temperature of the optimal design from the surrogate model 2 is the most appropriate as the minimum/maximum values are 331.0 K and 361.8 K, respectively. The substantial difference in the temperature of the corresponding design induces the stronger convection. For this reason, the optimal design of the surrogate model 2 is qualitatively evaluated to be the best. It gives the same conclusion as we have quantitatively evaluated the performance by the doubling time. Therefore, it is recommended that the optimal double-heater reactor has a diameter of 1.6033 mm, the aspect of 6.0, the top heater height of 15.0 %, and the bottom heater height of 7.0 %.

6.9 Conclusions

In this chapter, a methodology for designing double-heater cPCR reactors has been proposed for POC applications. The proposed method has the potential to reduce the development cost by lowering the reliance upon expensive experimentation. Here, we have shown that a cPCR reactor with double heaters can be computationally designed in pursuit of the best performance.

Initially, we have planned a DOE to investigate the design space for the double-heater reactors. A total of 625 design candidates are considered for the analysis. CFD simulations are implemented using the mathematical models as described in Chapters 2.2, 2.3, and 6.2, estimating the doubling time of all design candidates.

We have established the network training process for the design with higher accuracy. The CFD data was filtered by the three conditions to have a different number of samples in a data set. Three optimal designs and corresponding surrogate models were obtained by the hybrid algorithm for the optimization. We could select one of the best by comparing the relative percentage error obtained from the verification of the optimal design. Limited to this study, we found that a surrogate model estimates the performance well if it is developed based on 376

samples. Additionally, it is also confirmed that the optimal double-heater reactor has a diameter of 1.6033 mm, the aspect of 6.0, the top heater height of 15.0 %, and the bottom heater height of 7.0 %. Therefore, it is demonstrated that the proposed methodology has the capability of designing a double-heater cPCR reactor with higher accuracy at a low cost.

CHAPTER 7

CONCLUSIONS AND FUTUREWORK

7.1 Concluding Remarks

The investigation on the cPCR reactor has been implemented in the aspect of analysis and designs. We have confirmed the potential of cPCR devices to be used for POC testing by using the computational methods that we proposed. Two different types of cPCR devices were analyzed through the four different applications: 1) a single heater reactor, and 2) a double-heater reactor. We applied the mathematical model for the double-heater reactor as the first application to briefly study its potential to replace a part of expensive experiments. As the second application, a single heater reactor was rationally designed considering the challenges. We studied the single heater reactor lied in the horizontal position. Then, we implemented a design optimization for the double-heater reactor by expanding the study of the single heater reactor design as the last application.

For the analysis of the double-heater reactor, the performance was quantified based on the DNA doubling time. We have confirmed that they could be efficiently developed using the computational method. An insight into the heat flow physics was gained using the three-dimensional, conjugate momentum and heat transfer model. The buoyancy effect was produced by taking the thermal properties of pure water in the polynomial form. The fluid domain thermally coupled with the solid highly increased the accuracy of the model as well. We quantified the performance of reactors by conducting CFD simulations that use the DNA species transport model. The investigation was made to learn how the height of a capillary tube affects the performance. Through the study, we observed that the reaction was considerably dominated

by the velocity rather than what is commonly believed to be the quality of the flow circulation. Consequently, we confirmed that the method is capable of effectively quantifying the performance, such as the DNA doubling time, the number of cycles, and the number of DNAs. It has great potential to reduce the development cost dramatically by being independent of experimentation.

As a further step of the study for the double-heater reactor, we established a process for design optimization, which was an expansion study of the design methodology for a double-heater reactor. The study was aimed to obtain the optimal single-heater reactor design determined by the high-fidelity analysis-based optimization. The available design space was planned by using the DOE method. A great number of design candidates are considered for the analysis. CFD simulations are implemented using the mathematical models as described in Chapters 2.2, 2.3, and 6.2, estimating the doubling time of all design candidates. We have established the network training process for the design with higher accuracy. The CFD data was filtered by the three conditions to have a different number of samples in a data set. Three optimal designs and corresponding surrogate models were obtained by the hybrid algorithm for the optimization. We could select one of the best by comparing the relative percentage error obtained from the verification of the optimal design. Limited to this study, we found that a surrogate model could estimate the performance well after providing a moderate number of data samples. Additionally, it is also confirmed that the optimal double-heater reactor has a diameter of 1.6033 mm, the aspect of 6.0, the top heater height of 15.0 %, and the bottom heater height of 7.0 %. Therefore, it is demonstrated that the proposed methodology has the capability of designing a double-heater cPCR reactor with higher accuracy at a low cost.

Compared with the double-heater reactor, the design of the single heater reactor was somewhat challenging due to the maintenance of the proper temperature for the DNA thermal cycling processes. However, as a means of resolving the problem, we introduced a design methodology for the device to be portable, economical, yet still be accurate and efficient for a POC application. The cPCR model used in this chapter had three-dimensional, multi-regional blocks made up of the fluid and solid regions. For higher-fidelity simulations, we considered the solid domains thermally coupled with the fluid domains to induce convection in the fluid domains. The design space was planned by using the DOE method. Numerous candidates were initially simulated based on the conjugate momentum and heat transfer model. The performance of all design candidates was qualitatively evaluated according to the evaluation criteria, resulting in eleven "acceptable design" candidates. We implemented Phase II CFD simulations (species transport model) to quantify the performance of the acceptable candidates by the doubling time. We also carried out a case study to demonstrate a compromise between the performance and the volume capacity of the reactors, determining the best designs. Through the study, it was demonstrated that a single heater cPCR reactor could be effectively designed using the proposed methodology.

In pursuit of a POC application, testing in various environments is necessary. We covered one of the conditions aforementioned: the operating position. A single heater cPCR was laid down in a horizontal position, and the performance was evaluated for the comparison with a reactor in a vertical position. A real-time cPCR device has been successfully developed to induce horizontal convection. For the potential use as a POC application, the system was compact and enabled one-end heating and in situ fluorescence monitoring. The actual reactor of the cPCR system was computationally modeled to investigate insight into thermal convection.

Through the analysis, it was confirmed that the rapid thermal cycling made the horizontal cPCR reactor capable of reducing the required amplification time. We implemented CFD simulations for the horizontally/vertically positioned reactors, which used the conjugate momentum and heat transfer model, and the species transport model. The inherent characteristics of thermo-fluid were analyzed in depth. We evaluated the performance of the real-time horizontal cPCR reactor by detecting influenza A (H1N1) virus samples. The experimentations were effectively verified by the CFD simulations. It was demonstrated that the horizontal cPCR had performance almost equivalent to the vertically positioned cPCR reactor.

In conclusion, we have shown that the methodologies can be used for the design/analysis of cPCR reactors with various geometries. Whether cPCR reactors have a single-heater or double heaters, it is obvious that the methodologies propose the effective, economical ways of analysis and design by lowering the dependency on expensive experimentations. We even could reduce time and human efforts dramatically by adopting automation techniques for preprocessing, such as mesh generation, simulations and so on. Therefore, with the methodologies that we suggest, cPCR reactor can be designed by the purpose of POC applications. It will also thrive in public health hygiene for the people in the third world.

7.2 Future Work

We have proposed the computational methods for design/analysis of cPCR reactors as POC applications. The methodologies have a few limitations to be removed for future work, which are 1) an infinite amount of primers, 2) an assumption of PCR solutions as a Newtonian fluid, and 3) roughly determined constant values of the parameters associated with the reactions.

For the first limitation, the plateau effect is not expected due to the assumption of an infinite amount of primers. The volume capacity of a reactor is highly related to the

amplification time since it determines the amount of PCR solutions. The proposed method adopts the DNA species transport model that solves for the concentrations of dsDNA, aDNA, and ssDNA, as described in Chapter 2.3. The plateau of the DNA amplification can be considered by adding concentrations for primers to the species transport model. This method will enable the model to estimate the performance regarding the volume capacity of a reactor. It will be beneficial for designing cPCR reactors because the volume capacity can be included in the computational models as one of the factors that affect the performance.

We have assumed the fluid to be Newtonian fluid due to the pure-water-based PCR solution. For low concentration, the behavior of DNA solutions is very close to Newtonian fluids, which feature a linear relationship between shear stress and shear rate. However, the concentration gets higher as DNA is amplified; it results in non-Newtonian property of the DNA solution. One study revealed the fact that viscosity is proportional to the DNA concentration [73]. Another study suggested using the cross model as non-Newtonian viscosity model for the high DNA concentration [74]. The consideration of DNA solution as non-Newtonian fluids is needed as future work to improve our results.

Lastly, one of the biggest problems to use the species transport model was to provide the constant parameters related to reactions. Especially, although we have provided the plausible values of the reaction intensities of denaturation, annealing, and extension, the proper magnitude remains unknown. Additionally, we have adopted the Gaussian function to map the reaction intensities. The standard deviations for denaturation, annealing, and extension has been just presumed based on the range of temperatures for the respective thermal cycling process. The aforementioned physical properties need to be investigated to resolve the problems. Reverse

engineering may be utilized to find the quantities, and a different form of Gaussian function may be adapted to improve the accuracy of solutions.

REFERENCES

[1] Shu, J., Baysal, O., Qian, S., Qiu, X., and Wang, F., "Performance of convective polymerase chain reaction by doubling time," *International Journal of Heat and Mass Tansfer*, vol. 133, pp. 1230-1239, 2019.

[2] Qiu, X., Shu, J. I., Baysal, O., Wu, J., Qian, S., Ge, S., Li, K., Ye, X., Xia, N., and Yu, D., "Real-time capillary convective PCR based on horizontal thermal convection," *Microfluidics and Nanofluidics*, vol. 23, no. 3, p. 39, February 18 2019.

[3] Primiceri, E., Chiriaco, M. S., Notarangelo, F. M., Crocamo, A., Ardissino, D., Cereda, M., Bramanti, A. P., Bianchessi, M. A., Giannelli, G., and Maruccio, G., "Key Enabling Technologies for Point-of-Care Diagnostics," (in English), *Sensors*, vol. 18, no. 11, Nov 2018.

[4] Wu, J. D., Dong, M. L., Rigatto, C., Liu, Y., and Lin, F., "Lab-on-chip technology for chronic disease diagnosis," (in English), *npj Digital Medicine*, vol. 1, Apr 11 2018.

[5] Dincer, C., Bruch, R., Kling, A., Dittrich, P. S., and Urban, G. A., "Multiplexed Point-of-Care Testing - xPOCT," (in English), *Trends in Biotechnology*, vol. 35, no. 8, pp. 728-742, Aug 2017.

[6] Andrews, D., Chetty, Y., Cooper, B., Virk, M., Glass, S. K., Letters, A., Kelly, P. A., Sudhanva, M., and Jeyaratnam, D., "Multiplex PCR point of care testing versus routine, laboratory-based testing in the treatment of adults with respiratory tract infections: a

quasi-randomised study assessing impact on length of stay and antimicrobial use," (in English), *BMC Infectious Diseases*, vol. 17, Oct 10 2017.

[7] Petralia, S. and Conoci, S., "PCR Technologies for Point of Care Testing: Progress and Perspectives," (in English), *ACS Sensors*, vol. 2, no. 7, pp. 876-891, Jul 2017.

[8] Stone, C. and Mahony, J. B., "Point-of-care (POC) Tests for Infectious Diseases - The Next," *Annals of Infectious Disease and Epidemiology*, vol. 3, no. 1, p. 1025, 2018.

[9] Powledge, T. M., "The polymerase chain reaction," (in English), *Advances in Physiology Education*, vol. 28, no. 2, pp. 44-50, Jun 2004.

[10] Gibbs, R. A., "DNA Amplification by the Polymerase Chain-Reaction," (in English), *Analytical Chemistry*, vol. 62, no. 13, pp. 1202-1214, Jul 1 1990.

[11] Agrawal, N., Hassan, Y. A., and Ugaz, V. M., "A pocket-sized convective PCR thermocycler," (in English), *Angewandte Chemie International Edition*, vol. 46, no. 23, pp. 4316-4319, 2007.

[12] Chen, J. J., and Li, K. T., "Analysis of PCR Kinetics inside a Microfluidic DNA Amplification System," *Micromachines (Basel)*, vol. 9, no. 2, Jan 28 2018.

[13] Ragsdale, V., Li, H. Z., Sant, H., Ameel, T., and Gale, B. K., "A disposable, continuous-flow polymerase chain reaction device: design, fabrication and evaluation," (in English), *Biomedical Microdevices*, vol. 18, no. 4, Aug 2016.

[14] Li, Z. Q., Zhao, Y., Zhang, D. W., Zhuang, S. L., and Yamaguchi, Y., "The development of a portable buoyancy-driven PCR system and its evaluation by capillary

electrophoresis," (in English), *Sensors and Actuators B: Chemical*, vol. 230, pp. 779-784, Jul 2016.

[15] Zhang, C. S. and Xing, D., "Parallel DNA amplification by convective polymerase chain reaction with various annealing temperatures on a thermal gradient device," (in English), *Analytical Biochemistry*, vol. 387, no. 1, pp. 102-112, Apr 1 2009.

[16] Agrawal, N., and Ugaz, V. M., "A buoyancy-driven compact thermocycler for rapid PCR," (in English), *Clinics in Laboratory Medicine*, vol. 27, no. 1, pp. 215-223, Mar 2007.

[17] Chou, W.-P., Lee, C., Hsu, Z.-J., Lai, M.-H., Kuo, L.-S., and Chen, P.-H., "Development of Capillary Loop Convective Polymerase Chain Reaction Platform with Real-Time Fluorescence Detection," *Inventions*, vol. 2, no. 1, 2017.

[18] Koklu, M., and Baysal, O., "Performance Evaluation of a Micro Synthetic-Jet Actuator via Its Generated Vortices," *Micro and Nanosystems*, vol. 1, no. 2, pp. 147-162, 2009.

[19] Krishnan, M., Ugaz, V. M., and Burns, M. A., "PCR in a Rayleigh-Bénard Convection Cell," *Science*, vol. 298, no. 5594, pp. 793, 2002.

[20] Chen, Z. Y., Qian, S. Z., Abrams, W. R., Malamud, D., and Bau, H. H., "Thermosiphon-based PCR reactor: Experiment and modeling," (in English), *Analytical Chemistry*, vol. 76, no. 13, pp. 3707-3715, Jul 1 2004.

[21] Yariv, E., Ben-Dov, G., and Dorfman, K. D., "Polymerase chain reaction in natural convection systems: A convection-diffusion-reaction model," (in English), *Europhysics Letters,* vol. 71, no. 6, pp. 1008-1014, Sep 2005.

[22] Allen, J. W., Kenward, M., and Dorfman, K. D., "Coupled flow and reaction during natural convection PCR," (in English), *Microfluidics and Nanofluidics,* vol. 6, no. 1, pp. 121-130, Jan 2009.

[23] Muddu, R., Hassan, Y. A., and Ugaz, V. M., "Chaotically Accelerated Polymerase Chain Reaction by Microscale Rayleigh-Benard Convection," (in English), *Angewandte Chemie International Edition,* vol. 50, no. 13, pp. 3048-3052, 2011.

[24] Phaneuf, C. R., Pak, N., Saunders, D. C., Holst, G. L., Birjiniuk, J., Nagpal, N., Culpepper, S., Popler, E., Shane, A. L., Jerris, R., and Forest, C. R., "Thermally multiplexed polymerase chain reaction," (in English), *Biomicrofluidics,* vol. 9, no. 4, Jul 2015.

[25] Farrar, J. S., and Wittwer, C. T., "Extreme PCR: Efficient and specific DNA amplification in 15-60 seconds," (in English), *Clinical Chemistry,* vol. 61, no. 1, pp. 145-153, Jan 2015.

[26] Wang, X., Lim, H. J., and Son, A., "Characterization of denaturation and renaturation of DNA for DNA hybridization," *Journal of Toxicology and Environmental Health,* vol. 29, p. e2014007, 2014.

[27] Rengarajan, K., Cristol, S. M., Mehta, M., and Nickerson, J. M., "Quantifying DNA concentrations using fluorometry: A comparison of fluorophores," (in English), *Molecular Vision,* vol. 8, no. 43, pp. 416-421, Nov 6 2002.

[28] Sanderson, M. J., Smith, I., Parker, I., and Bootman, M. D., "Fluorescence microscopy," *Cold Spring Harbor Protocols,* vol. 2014, no. 10, p. pdb top071795, Oct 1 2014.

[29] Quesada, M. A., and Zhang, S. P., "Multiple capillary DNA sequencer that uses fiber-optic illumination and detection," (in English), *Electrophoresis,* vol. 17, no. 12, pp. 1841-1851, Dec 1996.

[30] Wong, M. L. and Medrano, J. F., "Real-time PCR for mRNA quantitation," (in English), *Biotechniques,* vol. 39, no. 1, pp. 75-85, Jul 2005.

[31] Ruijter, J. M., Ramakers, C., Hoogaars, W. M. H., Karlen, Y., Bakker, O., van den Hoff, M. J. B., and Moorman, A. F. M., "Amplification efficiency: linking baseline and bias in the analysis of quantitative PCR data," (in English), *Nucleic Acids Research,* vol. 37, no. 6, Apr 2009.

[32] Kainz, P., "The PCR plateau phase - towards an understanding of its limitations," (in English), *Biochimica et Biophysica Acta - Gene Structure and Expression,* vol. 1494, no. 1-2, pp. 23-27, Nov 15 2000.

[33] Morrison, C., and Gannon, F., "The Impact of the PCR Plateau-Phase on Quantitative PCR," (in English), *Biochimica et Biophysica Acta - Gene Structure and Expression,* vol. 1219, no. 2, pp. 493-498, Oct 18 1994.

[34] Çengel, Y. A., and Ghajar, A. J., *Heat and mass transfer: fundamentals & applications*, 5th ed. New York, N.Y.: McGraw-Hill, 2015, pp. xxi, 968 pages.

[35] Holman, J. P., *Heat transfer*, 10th ed. (McGraw-Hill series in mechanical engineering). Boston: McGraw Hill Higher Education, 2010, pp. xxii, 725 p.

[36] Çengel, Y. A., and Boles, M. A., *Thermodynamics : an engineering approach*, 8th ed. New York: McGraw-Hill Education, 2015, pp. xxvi, 996 pages.

[37] Wheeler, E. K., Benett, W., Stratton, P., Richards, J., Chen, A., Christian, A., Ness, K. D., Ortega, J., Li, L. G., Weisgraber, T. H., Goodson, K. E., and Milanovich, F., "Convectively driven polymerase chain reaction thermal cycler," (in English), *Analytical Chemistry*, vol. 76, no. 14, pp. 4011-4016, Jul 15 2004.

[38] Li, S. F., Fozdar, D. Y., Ali, M. F., Li, H., Shao, D. B., Vykoukal, D. M., Vykoukal, J., Floriano, P. N., Olsen, M., McDevitt, J. T., Gascoyne, P. R. C., and Chen, S. C., "A continuous-flow polymerase chain reaction microchip with regional velocity control," (in English), *Journal of Microelectromechanical Systems*, vol. 15, no. 1, pp. 223-236, Feb 2006.

[39] Marimuthu, K., Jing, C., and Chakrabarti, R., "Sequence-dependent biophysical modeling of DNA amplification," *Biophysical Journal*, vol. 107, no. 7, pp. 1731-43, Oct 7 2014.

[40] Marimuthu, K., and Chakrabarti, R., "Dynamics and control of DNA sequence amplification," (in English), *Journal of Chemical Physics*, vol. 141, no. 16, Oct 28 2014.

[41] Rossby, H. T., "A Study of Benard Convection with and without Rotation," (in English), *Journal of Fluid Mechanics*, vol. 36, pp. 309-&, 1969.

[42] Hennig, M., and Braun, D., "Convective polymerase chain reaction around micro immersion heater," *Applied Physics Letters*, vol. 87, p. 183901, 2005.

[43] Qiu, X., Ge, S., Gao, P., Li, K., Yang, Y., Zhang, S., Ye, X., Xia, N., and Qian, S., "A Low-Cost and Fast Real-Time PCR System Based on Capillary Convection," *SLAS Technol*, vol. 22, no. 1, pp. 13-17, Feb 2017.

[44] Churchill, S. W., and Chu, H. H. S., "Correlating Equations for Laminar and Turbulent Free Convection from a Vertical Plate," (in English), *International Journal of Heat and Mass Transfer*, vol. 18, no. 11, pp. 1323-1329, 1975.

[45] Braun, D., Goddard, N. L., and Libchaber, A., "Exponential DNA replication by laminar convection," (in English), *Physical Review Letters*, vol. 91, no. 15, Oct 10 2003.

[46] El-Ali, J., Perch-Nielsen, I. R., Poulsen, C. R., Bang, D. D., Telleman, P., and Wolff, A., "Simulation and experimental validation of a SU-8 based PCR thermocycler chip with integrated heaters and temperature sensor," (in English), *Sensors and Actuators A: Physical*, vol. 110, no. 1-3, pp. 3-10, Feb 1 2004.

[47] Erickson, D., and Li, D. Q., "Numerical simulations of a low power microchannel thermal cycling reactor," (in English), *International Journal of Heat and Mass Transfer*, vol. 45, no. 18, pp. 3759-3770, Aug 2002.

[48] Boetcher, S., "Natural convection heat transfer from horizontal cylinders," in *Natural convection heat transfer from horizontal cylinders* (SpringerBriefs in Thermal Engineering and Applied Science), Springer International Publishing, 2014, p. 48.

[49] Hayden, F. G., Rollins, B. S., and Madren, L. K., "Anti-influenza virus activity of the neuraminidase inhibitor 4-guanidino-Neu5Ac2en in cell culture and in human respiratory epithelium," *Antiviral Research*, vol. 25, no. 2, pp. 123-31, Oct 1994.

[50] Jonges, M., Liu, W. M., van der Vries, E., Jacobi, R., Pronk, I., Boog, C., Koopmans, M., Meijer, A., and Soethout, E., "Influenza virus inactivation for studies of antigenicity and phenotypic neuraminidase inhibitor resistance profiling," *Journal of Clinical Microbiology*, vol. 48, no. 3, pp. 928-40, Mar 2010.

[51] Allison, J. T., and Herber, D. R., "Multidisciplinary Design Optimization of Dynamic Engineering Systems," *AIAA Journal*, vol. 52, no. 4, pp. 691-710, 2014.

[52] Mack, Y., Goel, T., Shyy, W., Haftka, R., and Queipo, N., "Multiple Surrogates for the Shape Optimization of Bluff Body-facilitated Mixing," presented at the 43rd AIAA Aerospace Sciences Meeting and Exhibit, Reno, Nevada, Jan 10 - 13, 2005.

[53] Hacioglu, A., "Fast evolutionary algorithm for airfoil design via neural network," (in English), *AIAA Journal*, vol. 45, no. 9, pp. 2196-2203, Sep 2007.

[54] Iuliano, E., "Efficient Design Optimization Assisted by Sequential Surrogate Models," *International Journal of Aerospace Engineering*, vol. 2019, p. 34, 2019.

[55] Chamseddine, I. M., Frieboes, H. B., and Kokkolaras, M., "Design Optimization of Tumor Vasculature-Bound Nanoparticles," *Scientific Report*, vol. 8, no. 1, p. 17768, Dec 11 2018.

[56] Abd-Ellatif, S. A. M., "Optimizing sliver quality using Artificial Neural Networks in ring spinning," *Alexandria Engineering Journal*, vol. 52, no. 2, pp. 637-642, 2013.

[57] Srivastava, N., Hinton, G., Krizhevsky, A., Sutskever, I., and Salakhutdinov, R., "Dropout: A Simple Way to Prevent Neural Networks from Overfitting," (in English), *Journal of Machine Learning Research*, vol. 15, pp. 1929-1958, Jun 2014.

[58] Dongale, T. D., Patil, K. P., Vanjare, S. R., Chavan, A. R., Gaikwad, P. K., and Kamat, R. K., "Modelling of nanostructured memristor device characteristics using Artificial Neural Network (ANN)," (in English), *Journal of Computational Science*, vol. 11, pp. 82-90, Nov 2015.

[59] Vogl, T. P., Mangis, J. K., Rigler, A. K., Zink, W. T., and Alkon, D. L., "Accelerating the convergence of the backpropagation method," *Biological Cybermetrics*, vol. 59, pp. 257-263, 1988.

[60] Karnin, E., "A simple procedure for pruning back-propagation trained neural networks," *IEEE Transactions on Neural Networks*, vol. 1, no. 2, pp. 239-242, 1990.

[61] Burden, F., and Winkler, D., "Bayesian regularization of neural networks," *Methods Mol Biol*, vol. 458, pp. 25-44, 2008.

[62] Mackay, D. J. C., "Bayesian Interpolation," (in English), *Neural Computation*, vol. 4, no. 3, pp. 415-447, May 1992.

[63] Foresee, F. D., and Hagan, M. T., "Gauss-Newton approximation to Bayesian learning," in *Proceedings of International Conference on Neural Networks*, Houston, TX, USA, 1997.

[64] Mansoornejad, B., Mostoufi, N., and Jalali-Farahani, F., "A hybrid GA-SQP optimization technique for determination of kinetic parameters of hydrogenation reactions," *Computers and Chemical Engineering*, vol. 32, no. 2008, pp. 1447-1455, 2007.

[65] Kumar, M., Husian, M., Upreti, N., and Gupta, D., "Genetic Algorithm: Review and Application," *International Journal of Information Technology and Knowledge Management*, vol. 2, no. 2, pp. 451-454, 2010.

[66] Goldberg, D. E., *Genetic algorithms in search, optimization, and machine learning*. Reading, Mass.: Addison-Wesley Pub. Co., 1989, pp. xiii, 412 p.

[67] Peck, C. C., Dhawan, A. P., Meyer, C. M., and United States. National Aeronautics and Space Administration., *Genetic algorithm based input selection for a neural network function approximator with application to SSME health monitoring* (NASA contractor report, no. NASA CR-199089). Washington, DC, springfield, VA.: NASA ;National Technical Information Service, distributor, 1991, p. 1 volume.

[68] Yang, X., Teo, K. L., and Caccetta, L., *Optimization methods and applications* (Applied optimization, no. 52). Dordrecht ; Boston: Kluwer Academic Publishers, 2001, pp. xxxvii, 412 pages.

[69] Argáez, M., Velázquez, L., Quintero, C., Klie, H., and Wheeler, M. F., "A Hybrid Algorithm for Global Optimization Problems," *Reliable Computing*, vol. 15, pp. 230-241, 2011.

[70] Gill, P. E., Murray, W., and Wright, M. H., *Practical optimization*. London ; New York: Academic Press, 1981, pp. xvi, 401 p.

[71] Harvey, H. B., and Sotardi, S. T., "The Pareto Principle," *Journal of the American College of Radiology*, vol. 15, no. 6, p. 931, Jun 2018.

[72] Haykin, S. S., and Haykin, S. S., *Neural networks and learning machines*, 3rd ed. New York: Prentice Hall, 2009, pp. xxx, 906 p.

[73] Li, Y., Burke, D. T., Kopelman, R., and Burns, M. A., "Asynchronous Magnetic Bead Rotation (AMBR) Microviscometer for Label-Free DNA Analysis," *Biosensors (Basel)*, vol. 4, no. 1, pp. 76-89, Mar 2014.

[74] Bravo-Anaya, L. M., Pignon, F., Martinez, F. A. S., and Rinaudo, M., "Rheological Properties of DNA Molecules in Solution: Molecular Weight and Entanglement Influences," *Polymers (Basel)*, vol. 8, no. 8, Aug 3 2016.

[75] Orlandini, E., Bhattacharjee, S. M., Marenduzzo, D., Maritan, A., and Seno, F., "Mechanical denaturation of DNA: existence of a low-temperature denaturation," (in English), *Journal of Physics A: Mathematical and General*, vol. 34, no. 50, pp. L751-L758, Dec 21 2001.

(This page is intentionally left blank)

APPENDICES

APPENDIX A. USER-DEFINED OPENFOAM CODES

C++ OpenFOAM-library-based user-defined codes: `convDiffFoam`

<Structure of Files>

File Name	File Location
files	/convDiffFoam/Make/files
Options	/convDiffFoam/Make/options
convDiffFoam	/convDiffFoam/convDiffFoam.C
ConvDiff	/convDiffFoam/ConvDiff.H
refValues	/convDiffFoam/refValues.H
checkSource	/convDiffFoam/checkSource.H
nDNA	/convDiffFoam/nDNA.H
createFields	/convDiffFoam/createFields.H

<convDiffFoam.C>

```
#include <fstream>
#include "fvCFD.H"

using namespace std;

int main(int argc, char *argv[])
{
    #include "setRootCase.H"
    #include "createTime.H"
    #include "createMesh.H"
    #include "refValues.H"
    #include "createFields.H"
    #include "checkSource.H"

    scalar n=0;
    scalar dbtime = 0.0;
    scalar dbtimeOld;
    scalar C2_ini;
    scalar C1S_ini;
    scalar C1_ini;
    scalar Vtot;

    C2_ini = 0;
    C1S_ini = 0;
    C1_ini = 0;
    Vtot = 0;

    forAll(mesh.V(), idx)
    {
      C2_ini += mesh.V()[idx]*(C2[idx]);
      C1S_ini += mesh.V()[idx]*(C1S[idx]);
      C1_ini += mesh.V()[idx]*(C1[idx]);
      Vtot += mesh.V()[idx];
```

```
}

// Reduce decomposed variables in parallel to have a global variable
reduce(C1_ini, sumOp<scalar>());
reduce(C1S_ini, sumOp<scalar>());
reduce(C2_ini, sumOp<scalar>());
reduce(Vtot, sumOp<scalar>());

Info << "Total Volume of a Mesh = " << Vtot << endl;
Info << "dsDNA = " << C2_ini << endl;
Info << "aDNA = " << C1S_ini << endl;
Info << "ssDNA = " << C1_ini << endl;
Info << "Number of DNAs = " << C2_ini << endl;
Info<< "\nStarting time loop\n" << endl;

while (runTime.loop())
{

    Info<< "Time = " << runTime.timeName() << nl << endl;
    U = U.oldTime();
    U.correctBoundaryConditions();

    #include "ConDiff.H"

    U.storeOldTime();

    if (dbtime > 0) {
        dbtimeOld = dbtime;

    }
    else {
        dbtimeOld = 0;
    }

    #include "nDNA.H"

    double err = Foam::sqrt(Foam::pow(dbtimeOld - dbtime,2));

    Info << "Doubling Time Error = " << err << endl;

    runTime.write();

    if (n == 0) {
        if (C2_num >= 2*C2_ini) {

              C1.write();
              C1S.write();
              C2.write();
              f_a.write();
              f_d.write();
              f_e.write();
              T.write();
              U.write();

              if (doubling_time.value() == 0) {
                    break;
              }
```

```
                    n = 1;
                }
            }
            else {
                if (err < DT_tol.value()) {
                    break;
                }
            }

            Info<< "ExecutionTime = " << runTime.elapsedCpuTime() << " s"
                << "  ClockTime = " << runTime.elapsedClockTime() << " s"
                << nl << endl;
        }


        ofstream outfile2;
        outfile2.open("dbtime.txt");
        outfile2 << dbtime << endl;
        outfile2.close();


        Info<< "End\n" << endl;

        return 0;
}
```

<ConvDiff.H>

```
        dimensionedScalar k_a
        (
                "k_a",
                dimensionSet(0,0,-1,0,0,0,0),
                scalar(0.0)
        );
        dimensionedScalar k_e
        (
                "k_e",
                dimensionSet(0,0,-1,0,0,0,0),
                scalar(0.0)
        );
        dimensionedScalar k_d
        (
                "k_d",
                dimensionSet(0,0,-1,0,0,0,0),
                scalar(0.0)
        );

        k_a = ka*k;
        k_e = ke*k;
        k_d = kd*k;

        solve (
              fvm::ddt(C2)
            + fvm::div(phi, C2)
            - fvm::laplacian(D,C2)
            ==
```

```
          k_e*f_e*C1S - fvm::Sp(k_d*f_d,C2)
      );

    solve (
          fvm::ddt(C1)
        + fvm::div(phi, C1)
        - fvm::laplacian(D,C1)
        ==
          2*k_d*f_d*C2 - fvm::Sp(k_a*f_a,C1)
        );

    solve (
          fvm::ddt(C1S)
        + fvm::div(phi, C1S)
        - fvm::laplacian(D,C1S)
        ==
          k_a*f_a*C1 - fvm::Sp(k_e*f_e,C1S)
      );
```

<refValues.H>

```
Info << "\nReading refValues" << endl;

IOdictionary refValues
(
    IOobject
    (
      "refValues",
      runTime.constant(),
      mesh,
      IOobject::MUST_READ,
      IOobject::NO_WRITE
    )
);

dimensionedScalar C2loc
(
    refValues.lookup("C2loc")
);
Info << "Location of C2:" << C2loc << endl;

dimensionedScalar gvec
(
    refValues.lookup("gvec")
);
Info << "Gravitational Diretion:" << gvec << endl;

dimensionedScalar HptgC2
(
    refValues.lookup("HptgC2")
);
Info << "Percentage of Height:" << HptgC2 << endl;

dimensionedScalar nDNAini
(
    refValues.lookup("nDNAini")
```

```
);
Info << "Initial # of DNA:" << nDNAini << endl;

dimensionedScalar k
(
    refValues.lookup("k")
);
Info << "Reaction rate:" << k << " [1/s]" << endl;

dimensionedScalar D
(
    refValues.lookup("D")
);
Info << "Diffusivity is:" << D << endl;

dimensionedScalar kd
(
    refValues.lookup("kd")
);
Info << "Denaturation rate constant is:" << kd << endl;

dimensionedScalar ke
(
    refValues.lookup("ke")
);
Info << "Extension rate constant is:" << ke << endl;

dimensionedScalar ka
(
    refValues.lookup("ka")
);
Info << "Annealing rate constant is:" << ka << endl;

dimensionedScalar fd
(
    refValues.lookup("fd")
);
Info << "The reaction intensity of denaturation is:" << fd << endl;

dimensionedScalar fe
(
    refValues.lookup("fe")
);
Info << "The reaction intensity of extension is:" << fe << endl;

dimensionedScalar fa
(
    refValues.lookup("fa")
);
Info << "The reaction intensity of annealing is:" << fa << endl;

dimensionedScalar Td
(
    refValues.lookup("Td")
);
Info << "The denaturation tempearture is:" << Td << endl;
```

```
dimensionedScalar Te
(
    refValues.lookup("Te")
);
Info << "The extension tempearture is:" << Te << endl;

dimensionedScalar Ta
(
    refValues.lookup("Ta")
);
Info << "The annealing tempearture is:" << Ta << endl;

dimensionedScalar sigma_d
(
    refValues.lookup("sigma_d")
);
Info << "The sigma for denaturation is:" << sigma_d << endl;

dimensionedScalar sigma_a
(
    refValues.lookup("sigma_a")
);
Info << "The sigma for annealing is:" << sigma_a << endl;

dimensionedScalar sigma_e
(
    refValues.lookup("sigma_e")
);
Info << "The sigma for extension is:" << sigma_e << endl;

dimensionedScalar doubling_time
(
    refValues.lookup("doubling_time")
);
Info << "Check only doubling time? (0:yes, 1:no)" << doubling_time << endl;

dimensionedScalar DT_tol
(
    refValues.lookup("DT_tol")
);
Info << "Tolerance for Doubling time:" << DT_tol << endl;

dimensionedScalar gauss_m
(
    refValues.lookup("gauss_m")
);
Info << "Gaussian Member Function, Factor 'm':" << gauss_m << endl;

dimensionedScalar gauss_r
(
    refValues.lookup("gauss_r")
);
Info << "Gaussian Member Function, Factor 'r':" << gauss_r << endl;
```

<checkSource.H>

```
scalar Pd;
scalar Pe;
scalar Pa;

dimensionedScalar Length;

forAll (mesh.C(), Idx) {

      Pd = Foam::exp(-1/gauss_r.value()*Foam::pow( (T[Idx]-
Td.value())/sigma_d.value(), gauss_m.value() ));

      f_d[Idx] = fd.value() * Pd;

      Pe = Foam::exp(-1/gauss_r.value() * Foam::pow( (T[Idx]-
Te.value())/sigma_e.value(), gauss_m.value() ));

      f_e[Idx] = fe.value() * Pe;

      Pa = Foam::exp(-1/gauss_r.value() * Foam::pow( (T[Idx]-
Ta.value())/sigma_a.value(), gauss_m.value() ));

      f_a[Idx] = fa.value() * Pa;

}
```

<nDNA.H>

```
scalar C2_num;
scalar C1S_num;
scalar C1_num;

C2_num = 0;
C1S_num = 0;
C1_num = 0;

forAll(mesh.V(), idx)
{
      C2_num += mesh.V()[idx]*(C2[idx]);
      C1S_num += mesh.V()[idx]*(C1S[idx]);
      C1_num += mesh.V()[idx]*(C1[idx]);
}

// Reduce decomposed variables in parallel to have a global variable
reduce(C1_num, sumOp<scalar>());
reduce(C1S_num, sumOp<scalar>());
reduce(C2_num, sumOp<scalar>());

Info << "dsDNA = " << C2_num << endl;
Info << "aDNA = " << C1S_num << endl;
Info << "ssDNA = " << C1_num << endl;
Info << endl << "Number of DNAs = " << C2_num<< endl;

if (mag(Foam::log(C2_num)-Foam::log(C2_ini)) > 1e-12) {
    dbtime = (runTime.value()*Foam::log(2.0))/(Foam::log(C2_num/C2_ini));
    Info << "DoublingTime [s] = " << dbtime <<endl;
```

```
}
else {
      dbtime = runTime.value() * 2;
    Info << "DoublingTime [s] Not Appliable Now" << endl;
}
```

<createFields.H>

```
Info<< "Reading field C1\n" << endl;
volScalarField C1
(
    IOobject
    (
        "C1",
        runTime.timeName(),
        mesh,
        IOobject::MUST_READ,
        IOobject::AUTO_WRITE
    ),
    mesh
);

Info<< "Reading field C1S\n" << endl;
volScalarField C1S
(
    IOobject
    (
        "C1S",
        runTime.timeName(),
        mesh,
        IOobject::MUST_READ,
        IOobject::AUTO_WRITE
    ),
    mesh
);

Info<< "Reading field C2\n" << endl;
volScalarField C2
(
    IOobject
    (
        "C2",
        runTime.timeName(),
        mesh,
        IOobject::MUST_READ,
        IOobject::AUTO_WRITE
    ),
    mesh
);

Info<< "Reading field U\n" << endl;
volVectorField U
(
    IOobject
    (
        "U",
```

```
        runTime.timeName(),
        mesh,
        IOobject::MUST_READ,
        IOobject::AUTO_WRITE
    ),
    mesh
);

Info<< "Reading field T\n" << endl;
volScalarField T
(
    IOobject
    (
        "T",
        runTime.timeName(),
        mesh,
        IOobject::MUST_READ,
        IOobject::AUTO_WRITE
    ),
    mesh
);

Info<< "Reading field f_d\n" << endl;
volScalarField f_d
(
    IOobject
    (
        "f_d",
        runTime.timeName(),
        mesh,
        IOobject::NO_READ,
        IOobject::AUTO_WRITE
    ),
    mesh,
      dimensionedScalar("f_d", dimless, scalar(0.0))
);

Info<< "Reading field f_a\n" << endl;
volScalarField f_a
(
    IOobject
    (
        "f_a",
        runTime.timeName(),
        mesh,
        IOobject::NO_READ,
        IOobject::AUTO_WRITE
    ),
    mesh,
ensionedScalar("f_a", dimless, scalar(0.0))
);

Info<< "Reading field f_e\n" << endl;
volScalarField f_e
(
    IOobject
    (
```

```
        "f_e",
        runTime.timeName(),
        mesh,
        IOobject::NO_READ,
        IOobject::AUTO_WRITE
    ),
    mesh,
      dimensionedScalar("f_e", dimless, scalar(0.0))
);
```

<files>

```
convDiffFoam.C

EXE = $(FOAM_USER_APPBIN)/convDiffFoam
```

<options>

```
EXE_INC = \
    -I$(LIB_SRC)/finiteVolume/lnInclude \
    -I$(LIB_SRC)/meshTools/lnInclude

EXE_LIBS = \
    -lfiniteVolume \
    -lmeshTools
```

APPENDIX B. MESH AUTOMATION

A mesh automation code is developed using `tcl` & `tk` scripts. The code is run by Pointwise Glyph 2 and has a user-friendly GUI, as shown in Fig. A-1.

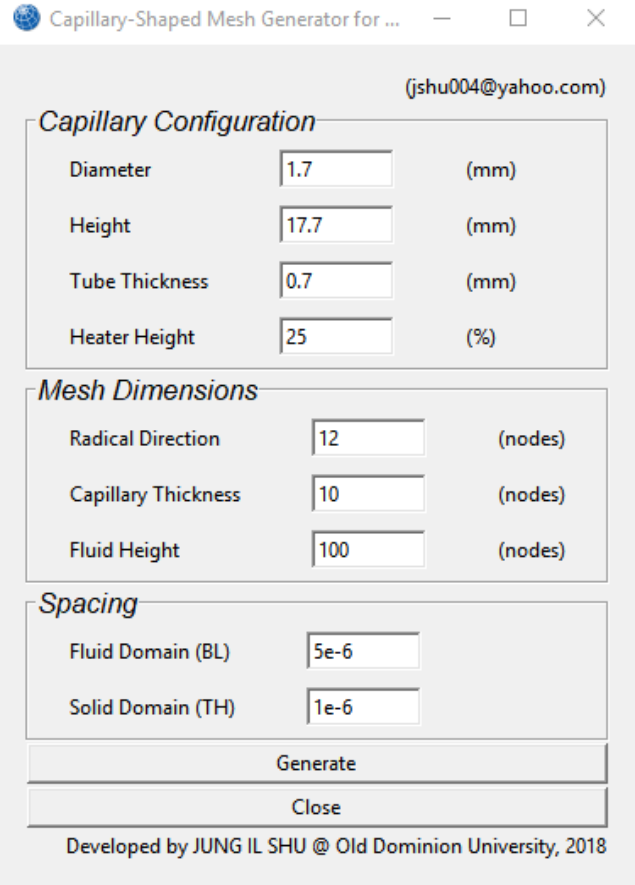

Fig. A-1. User-Friendly GUI for Automatic Generation of Single-Heater cPCR Meshes

The code automatically generates a multi-regional mesh within a couple of seconds, resulting in a fully structured typed one with numerous hexahedral cells. A user can input a value of the shape parameters in the first frame of the window, named '*Capillary Configuration*.' The fineness of a mesh can be defined by providing values of the respective dimensions in '*Mesh Dimensions*.' In "Spacing" frame, the gaps between the nodes are determined near the boundaries of the solid and fluid regions.

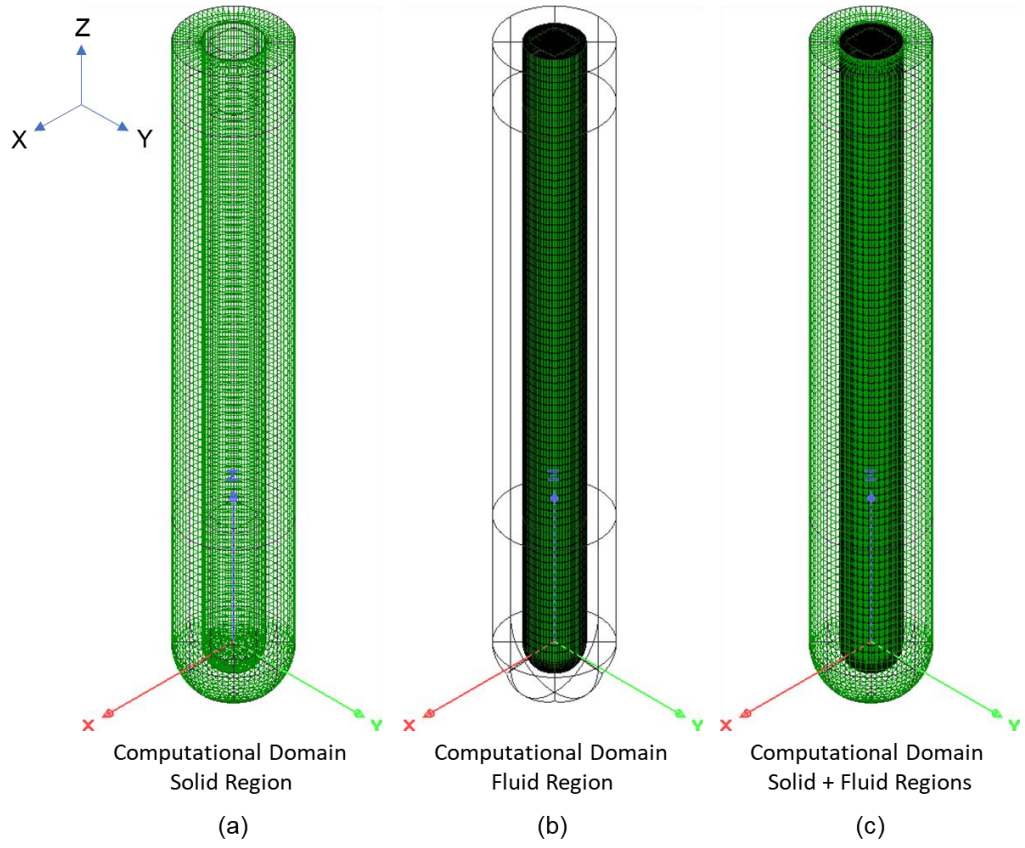

Fig. A-2. Fully Structured Single-Heater cPCR Meshes: (a) Solid Region Only; (b) Fluid Region Only; (c) Solid and Fluid Regions Together

Fig. A-2 represents the meshes generated by the mesh automation code. The left one (Fig. A-2 (a)) shows the computational domain for the solid region, the middle (b) represents the computational domain for the fluid region, and the right one (c) shows the combined mesh, which is the final version a user can handle.

We develop another code for double-heater CPCR reactors, which generates a great number of the meshes with various dimensions within a few seconds by one click, which was used for the study in Chapter 6. However, the we do not intentionally include the detail explanation of the code in this study.

APPENDIX C. DESIGN MATRIX OF SINGLE HEATER REACTORS

No.	#1	#2	#3	#4	#5
AR	HH 20.0%	HH 25.0%	HH 30.0%	HH 35.0%	HH 40.0%
6.0	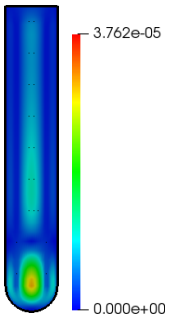	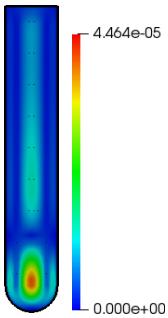	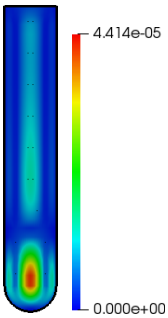	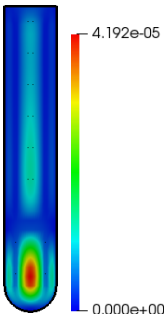	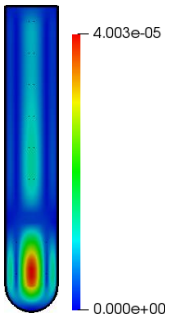
No.	#6	#7	#8	#9	#10
AR	HH 20.0%	HH 25.0%	HH 30.0%	HH 35.0%	HH 40.0%
8.0	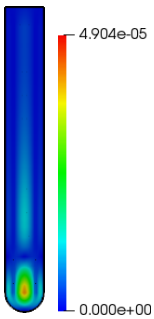	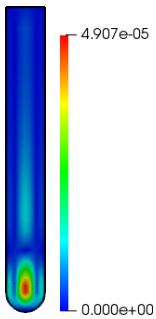	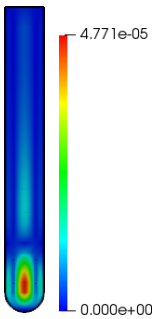	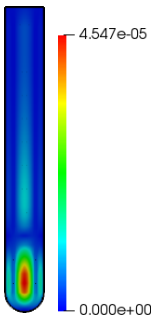	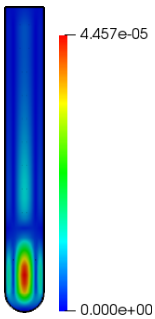
No.	#11	#12	#13	#14	#15
AR	HH 20.0%	HH 25.0%	HH 30.0%	HH 35.0%	HH 40.0%
10.0	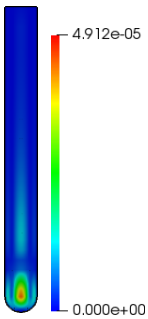	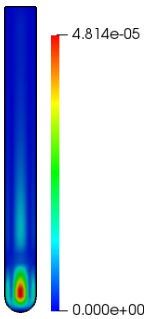	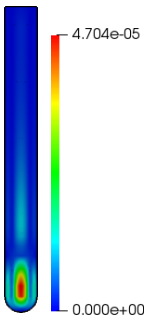	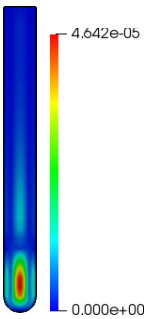	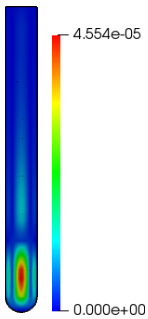
No.	#16	#17	#18	#19	#20
AR	HH 20.0%	HH 25.0%	HH 30.0%	HH 35.0%	HH 40.0%
12.0	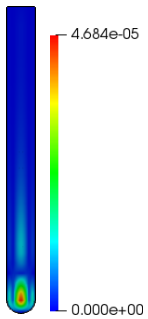	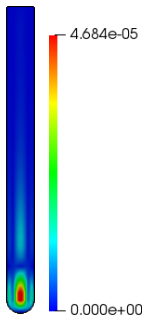	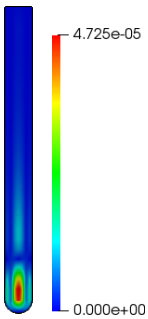	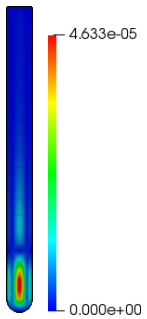	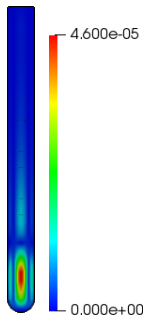

Fig. A-3. Design matrix of velocity fields for Designs #1-20 in the YZ Plane

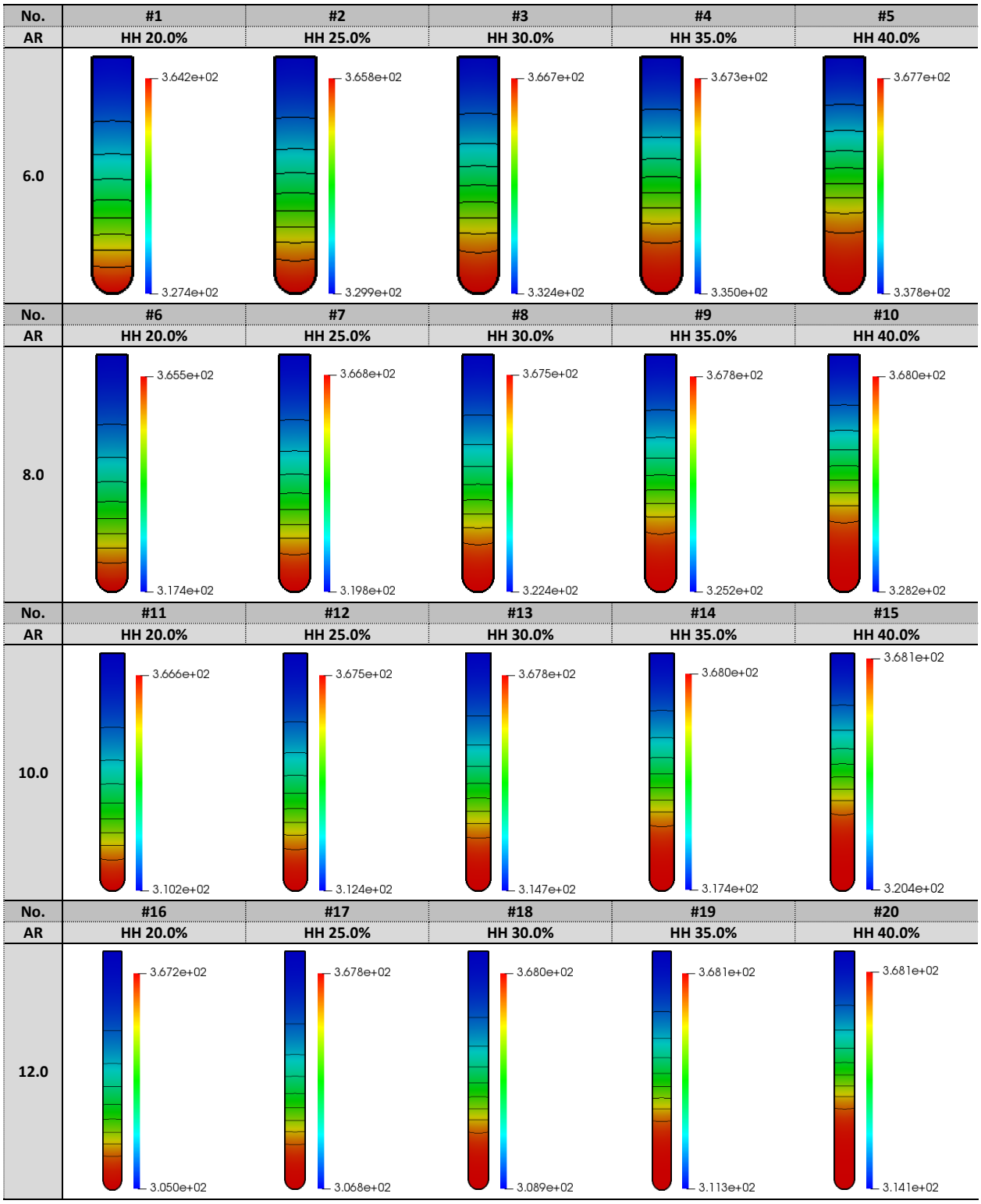

Fig. A-4. Design matrix of temperature fields for Designs #1-20 in the YZ Plane

No.	#21	#22	#23	#24	#25
AR	HH 20.0%	HH 25.0%	HH 30.0%	HH 35.0%	HH 40.0%
6.0	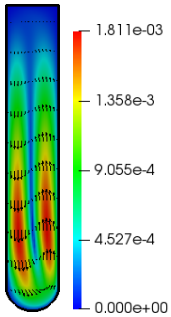	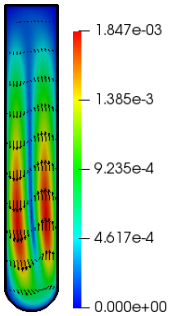	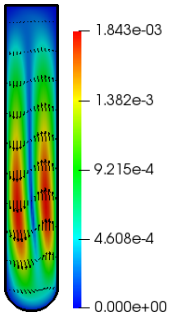	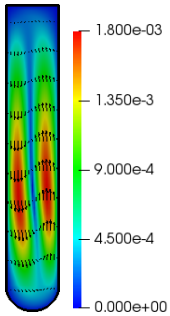	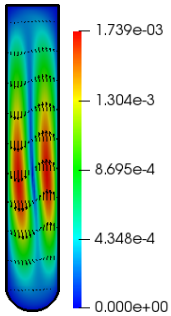
No.	#26	#27	#28	#29	#30
AR	HH 20.0%	HH 25.0%	HH 30.0%	HH 35.0%	HH 40.0%
8.0	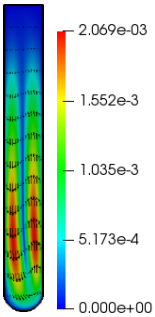	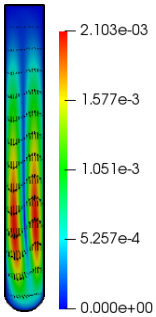	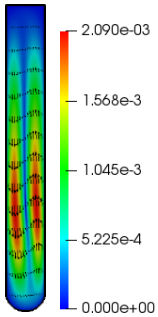	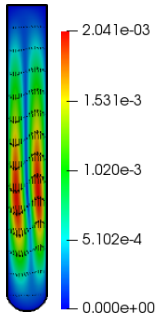	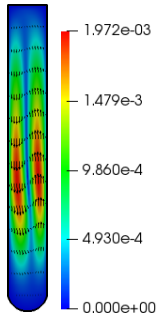
No.	#31	#32	#33	#34	#35
AR	HH 20.0%	HH 25.0%	HH 30.0%	HH 35.0%	HH 40.0%
10.0	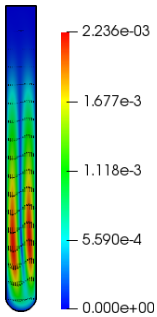	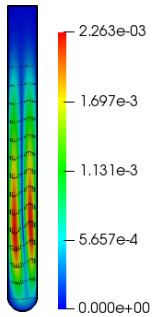	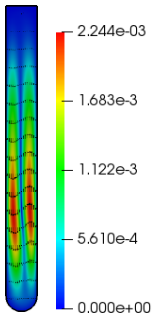	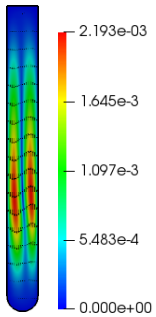	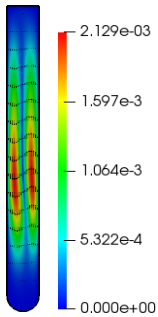
No.	#36	#37	#38	#39	#40
AR	HH 20.0%	HH 25.0%	HH 30.0%	HH 35.0%	HH 40.0%
12.0	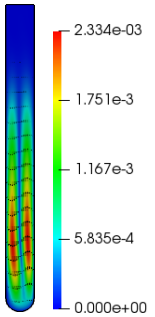	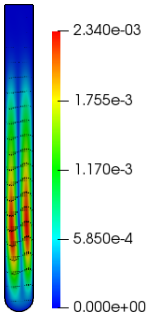	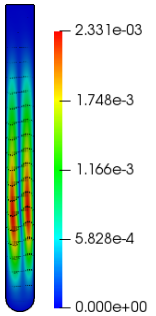	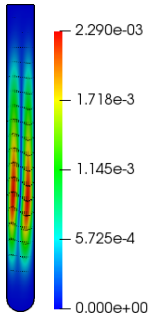	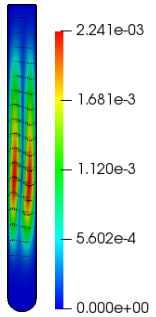

Fig. A-5. Design matrix of velocity fields for Designs #21-40 in the YZ Plane

No.	#21	#22	#23	#24	#25
AR	HH 20.0%	HH 25.0%	HH 30.0%	HH 35.0%	HH 40.0%
6.0	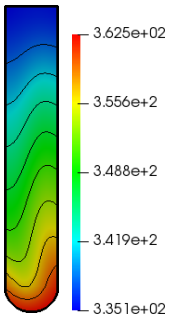	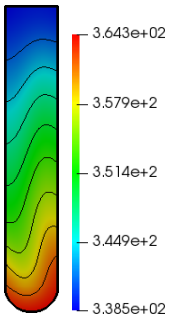	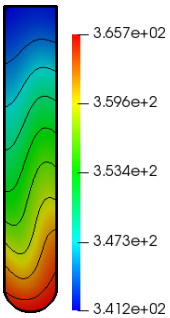	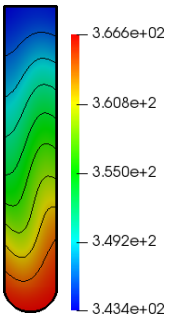	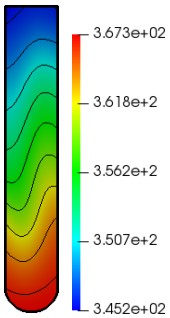
No.	#26	#27	#28	#29	#30
AR	HH 20.0%	HH 25.0%	HH 30.0%	HH 35.0%	HH 40.0%
8.0	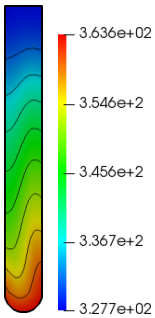	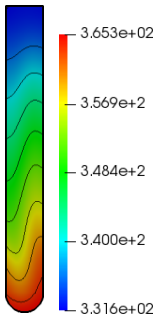	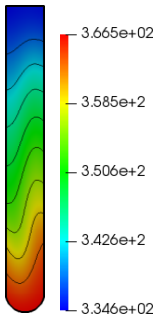	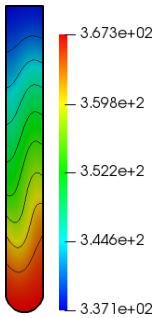	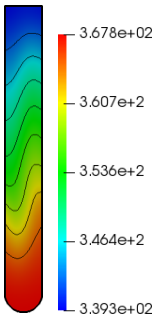
No.	#31	#32	#33	#34	#35
AR	HH 20.0%	HH 25.0%	HH 30.0%	HH 35.0%	HH 40.0%
10.0	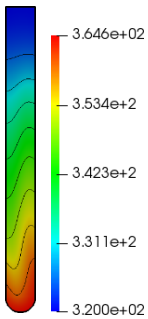	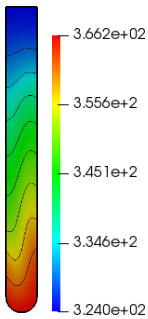	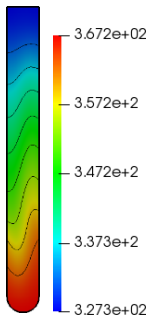	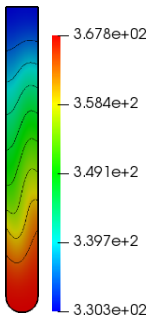	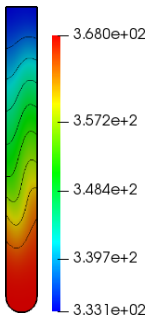
No.	#36	#37	#38	#39	#40
AR	HH 20.0%	HH 25.0%	HH 30.0%	HH 35.0%	HH 40.0%
12.0	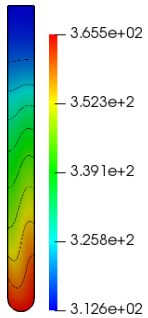	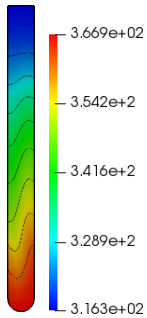	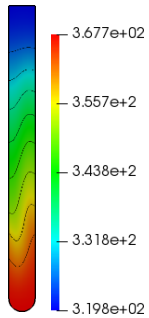	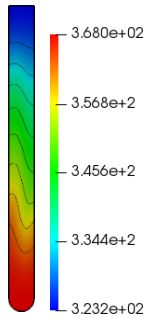	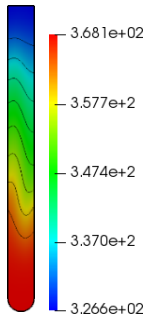

Fig. A-6. Design matrix of temperature fields for Designs #21-40 in the YZ Plane

No.	#41	#42	#43	#44	#45
AR	HH 20.0%	HH 25.0%	HH 30.0%	HH 35.0%	HH 40.0%
6.0	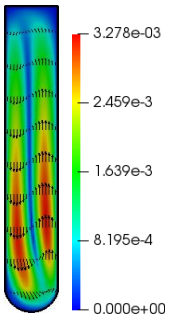	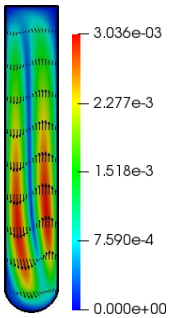	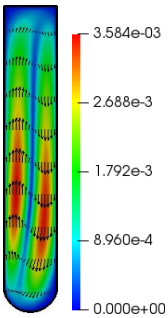	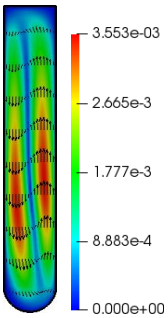	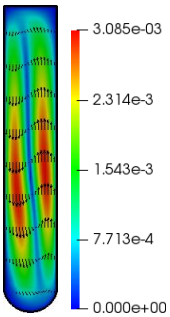
No.	#46	#47	#48	#49	#50
AR	HH 20.0%	HH 25.0%	HH 30.0%	HH 35.0%	HH 40.0%
8.0	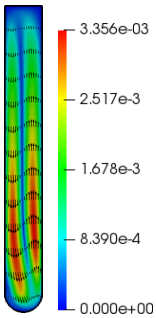	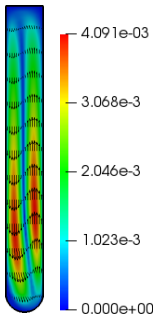	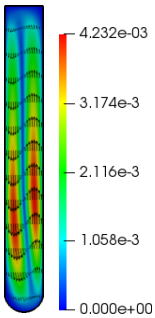	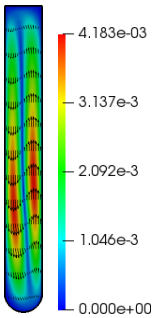	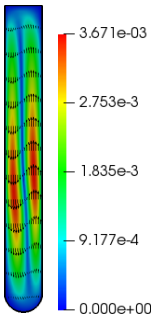
No.	#51	#52	#53	#54	#55
AR	HH 20.0%	HH 25.0%	HH 30.0%	HH 35.0%	HH 40.0%
10.0	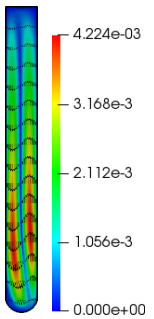	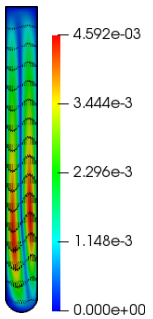	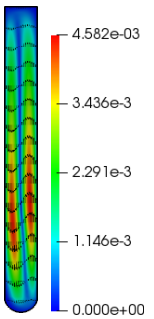	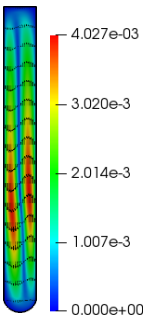	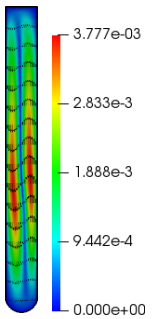
No.	#56	#57	#58	#59	#60
AR	HH 20.0%	HH 25.0%	HH 30.0%	HH 35.0%	HH 40.0%
12.0	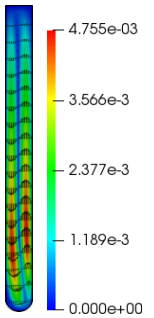	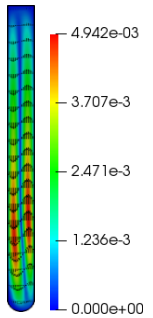	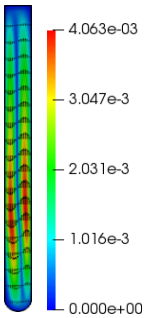	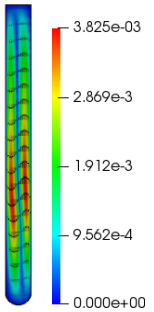	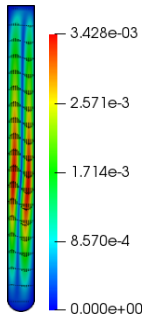

Fig. A-7. Design matrix of velocity fields for Designs #41-60 in the YZ Plane

No.	#41	#42	#43	#44	#45
AR	HH 20.0%	HH 25.0%	HH 30.0%	HH 35.0%	HH 40.0%
6.0	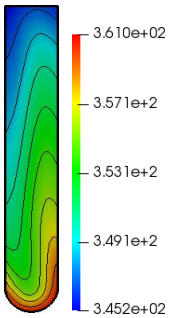	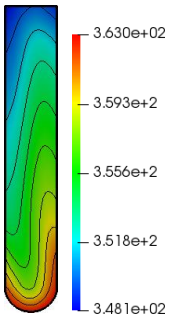	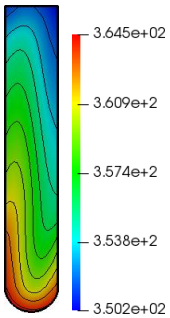	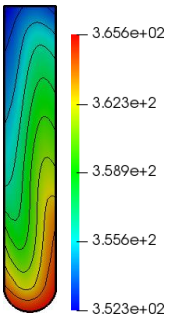	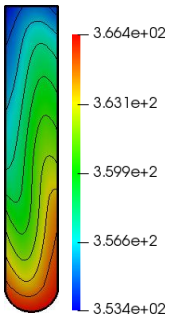
No.	#46	#47	#48	#49	#50
AR	HH 20.0%	HH 25.0%	HH 30.0%	HH 35.0%	HH 40.0%
8.0	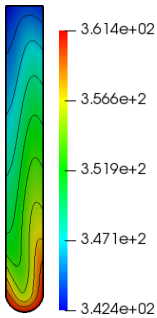	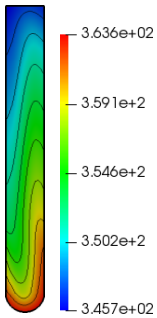	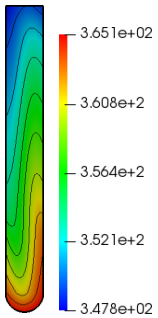	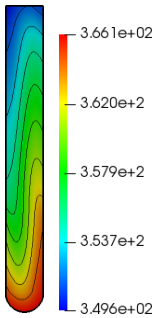	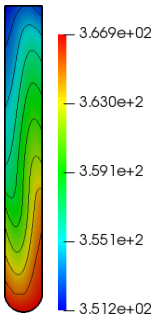
No.	#31	#32	#33	#34	#35
AR	HH 20.0%	HH 25.0%	HH 30.0%	HH 35.0%	HH 40.0%
10.0	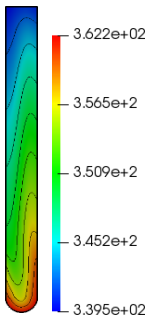	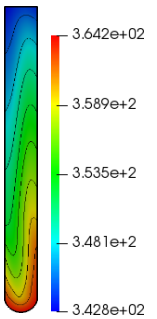	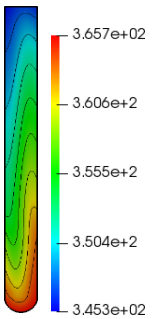	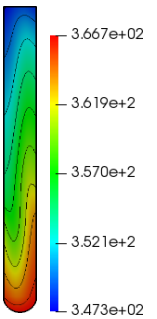	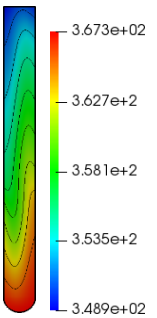
No.	#36	#37	#38	#39	#40
AR	HH 20.0%	HH 25.0%	HH 30.0%	HH 35.0%	HH 40.0%
12.0	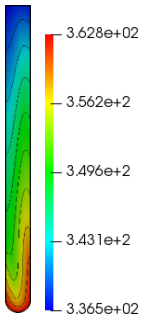	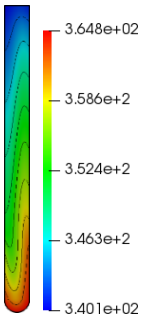	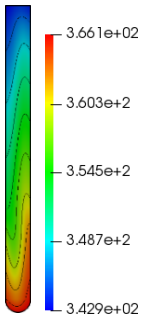	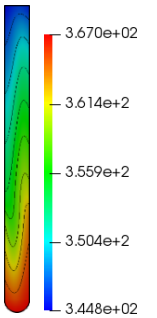	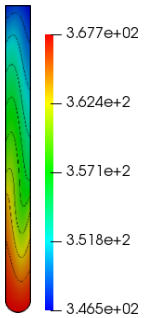

Fig. A-8. Design matrix of temperature fields for Designs #41-60 in the YZ Plane

APPENDIX D. DESIGN PERFORMANCE RESULTS

TABLE C-1

CANDIDATES NUMBER FROM 1 TO 100

No.	d	AR	$h_{rt,t}$	$h_{rt,b}$	t_d
1	1.3	6	7	7	255.4504213
2	1.3	6	7	9	190.8164133
3	1.3	6	7	11	148.0349787
4	1.3	6	7	13	118.8143166
5	1.3	6	7	15	98.22540739
6	1.3	6	9	7	197.1838034
7	1.3	6	9	9	150.7188082
8	1.3	6	9	11	119.4517965
9	1.3	6	9	13	97.53810429
10	1.3	6	9	15	82.27963861
11	1.3	6	11	7	156.9682729
12	1.3	6	11	9	121.9405768
13	1.3	6	11	11	98.45275542
14	1.3	6	11	13	82.25374668
15	1.3	6	11	15	70.51882941
16	1.3	6	13	7	127.5675663
17	1.3	6	13	9	101.0936133
18	1.3	6	13	11	83.24348529
19	1.3	6	13	13	70.52269456
20	1.3	6	13	15	61.82375751
21	1.3	6	15	7	105.8014817
22	1.3	6	15	9	85.77651634
23	1.3	6	15	11	71.77070811
24	1.3	6	15	13	61.88075793
25	1.3	6	15	15	54.86243477
26	1.3	7	7	7	1466.635585
27	1.3	7	7	9	1014.072858
28	1.3	7	7	11	746.4415158
29	1.3	7	7	13	555.0149596
30	1.3	7	7	15	418.0900057
31	1.3	7	9	7	996.5008562
32	1.3	7	9	9	724.6758337
33	1.3	7	9	11	537.7551387
34	1.3	7	9	13	404.6189696
35	1.3	7	9	15	307.0294023
36	1.3	7	11	7	726.5455365
37	1.3	7	11	9	534.8631362
38	1.3	7	11	11	399.7610732
39	1.3	7	11	13	301.9442479
40	1.3	7	11	15	230.8284308
41	1.3	7	13	7	545.9295112
42	1.3	7	13	9	404.1514328
43	1.3	7	13	11	302.2283831
44	1.3	7	13	13	229.4843636
45	1.3	7	13	15	177.4583222
46	1.3	7	15	7	417.896848
47	1.3	7	15	9	308.6962829
48	1.3	7	15	11	231.3230481
49	1.3	7	15	13	177.3583329
50	1.3	7	15	15	139.3309376
51	1.3	8	7	7	756.4663509
52	1.3	8	7	9	2473.612936
53	1.3	8	7	11	6172.554154
54	1.3	8	7	13	3399.803691
55	1.3	8	7	15	2097.334805
56	1.3	8	9	7	2414.717917
57	1.3	8	9	9	4679.463749
58	1.3	8	9	11	3361.752682
59	1.3	8	9	13	1965.008897
60	1.3	8	9	15	1274.448919
61	1.3	8	11	7	3063.026705
62	1.3	8	11	9	3547.97799
63	1.3	8	11	11	1893.930026
64	1.3	8	11	13	1190.440781
65	1.3	8	11	15	876.9283063
66	1.3	8	13	7	3998.400096
67	1.3	8	13	9	2011.55956
68	1.3	8	13	11	1158.169808
69	1.3	8	13	13	841.8547182
70	1.3	8	13	15	654.5422661
71	1.3	8	15	7	2317.726855
72	1.3	8	15	9	1177.58949
73	1.3	8	15	11	823.7386522
74	1.3	8	15	13	637.5755553
75	1.3	8	15	15	497.5517128
76	1.3	9	7	7	1031.662019
77	1.3	9	7	9	1004.536105
78	1.3	9	7	11	647.324851
79	1.3	9	7	13	1878.580998
80	1.3	9	7	15	866.1758785
81	1.3	9	9	7	954.1557983
82	1.3	9	9	9	664.3957679
83	1.3	9	9	11	1935.747321
84	1.3	9	9	13	839.6163244
85	1.3	9	9	15	1222.640055
86	1.3	9	11	7	712.6528819
87	1.3	9	11	9	1911.757682
88	1.3	9	11	11	767.8514956
89	1.3	9	11	13	1462.670236
90	1.3	9	11	15	24930.46703
91	1.3	9	13	7	1914.481613
92	1.3	9	13	9	728.2248242
93	1.3	9	13	11	1446.425748
94	1.3	9	13	13	36201.54237
95	1.3	9	13	15	3777.489216
96	1.3	9	15	7	705.5419286
97	1.3	9	15	9	1504.55278
98	1.3	9	15	11	54229.93715
99	1.3	9	15	13	3874.879673
100	1.3	9	15	15	1999.146013

TABLE C-2

CANDIDATES NUMBER FROM 101 TO 200

No.	d	AR	$h_{rt,t}$	$h_{rt,b}$	t_d
101	1.3	10	7	7	766.9346359
102	1.3	10	7	9	684.3413793
103	1.3	10	7	11	1377.52294
104	1.3	10	7	13	671.2364981
105	1.3	10	7	15	620.5356451
106	1.3	10	9	7	686.9230951
107	1.3	10	9	9	1389.434203
108	1.3	10	9	11	663.5127969
109	1.3	10	9	13	621.2340773
110	1.3	10	9	15	1520.512638
111	1.3	10	11	7	1405.83844
112	1.3	10	11	9	667.5906377
113	1.3	10	11	11	619.6218381
114	1.3	10	11	13	1505.383553
115	1.3	10	11	15	1046.42859
116	1.3	10	13	7	651.8771315
117	1.3	10	13	9	617.5864116
118	1.3	10	13	11	1769.043608
119	1.3	10	13	13	977.468861
120	1.3	10	13	15	702.879436
121	1.3	10	15	7	618.8718899
122	1.3	10	15	9	1717.187554
123	1.3	10	15	11	1717.187554
124	1.3	10	15	13	689.3318467
125	1.3	10	15	15	994.0128523
126	1.4	6	7	7	45.44137433
127	1.4	6	7	9	42.50749949
128	1.4	6	7	11	40.61679685
129	1.4	6	7	13	39.39359675
130	1.4	6	7	15	39.02652738
131	1.4	6	9	7	41.69465942
132	1.4	6	9	9	39.10361333
133	1.4	6	9	11	37.27863101
134	1.4	6	9	13	36.26084383
135	1.4	6	9	15	35.61586179
136	1.4	6	11	7	38.77673882
137	1.4	6	11	9	36.37982215
138	1.4	6	11	11	34.64861629
139	1.4	6	11	13	33.54643078
140	1.4	6	11	15	32.8352641
141	1.4	6	13	7	32.8352641
142	1.4	6	13	9	32.8352641
143	1.4	6	13	11	32.70724776
144	1.4	6	13	13	31.51650782
145	1.4	6	13	15	30.8107704
146	1.4	6	15	7	34.37676699
147	1.4	6	15	9	32.46737601
148	1.4	6	15	11	30.95160167
149	1.4	6	15	13	29.93446679
150	1.4	6	15	15	29.21724901
151	1.4	7	7	7	86.19917431
152	1.4	7	7	9	71.59462775
153	1.4	7	7	11	62.06273336
154	1.4	7	7	13	55.30070166
155	1.4	7	7	15	51.44872909
156	1.4	7	9	7	73.93678384
157	1.4	7	9	9	62.38996243
158	1.4	7	9	11	54.64902309
159	1.4	7	9	13	49.47249526
160	1.4	7	9	15	45.84208015
161	1.4	7	11	7	64.67156528
162	1.4	7	11	9	55.61836289
163	1.4	7	11	11	49.50471681
164	1.4	7	11	13	45.20132212
165	1.4	7	11	15	42.11358229
166	1.4	7	13	7	57.40458094
167	1.4	7	13	9	50.16716689
168	1.4	7	13	11	45.26182778
169	1.4	7	13	13	42.01037387
170	1.4	7	13	15	39.32920671
171	1.4	7	15	7	52.08408412
172	1.4	7	15	9	46.39776465
173	1.4	7	15	11	42.03611951
174	1.4	7	15	13	39.06895859
175	1.4	7	15	15	36.84162677
176	1.4	8	7	7	326.0987108
177	1.4	8	7	9	234.1942506
178	1.4	8	7	11	171.4830175
179	1.4	8	7	13	131.9939543
180	1.4	8	7	15	105.1616302
181	1.4	8	9	7	242.9669373
182	1.4	8	9	9	176.5018674
183	1.4	8	9	11	132.1089326
184	1.4	8	9	13	104.1351741
185	1.4	8	9	15	85.62961375
186	1.4	8	11	7	183.4458675
187	1.4	8	11	9	135.353246
188	1.4	8	11	11	104.217634
189	1.4	8	11	13	85.17666008
190	1.4	8	11	15	72.19754815
191	1.4	8	13	7	142.7891677
192	1.4	8	13	9	108.0065938
193	1.4	8	13	11	85.85727972
194	1.4	8	13	13	71.98017113
195	1.4	8	13	15	62.31166941
196	1.4	8	15	7	113.8983991
197	1.4	8	15	9	89.10052566
198	1.4	8	15	11	72.89881907
199	1.4	8	15	13	62.40269485
200	1.4	8	15	15	55.4593856

TABLE C-3

CANDIDATES NUMBER FROM 201 TO 300

No.	d	AR	$h_{rt,t}$	$h_{rt,b}$	t_d
201	1.4	9	7	7	1447.563435
202	1.4	9	7	9	961.0613279
203	1.4	9	7	11	707.4807529
204	1.4	9	7	13	526.7604179
205	1.4	9	7	15	393.3061232
206	1.4	9	9	7	955.0169668
207	1.4	9	9	9	688.9709038
208	1.4	9	9	11	514.3935613
209	1.4	9	9	13	381.8033743
210	1.4	9	9	15	283.2643431
211	1.4	9	11	7	690.4538872
212	1.4	9	11	9	510.2573932
213	1.4	9	11	11	378.1833136
214	1.4	9	11	13	278.5291796
215	1.4	9	11	15	206.825742
216	1.4	9	13	7	513.1455618
217	1.4	9	13	9	378.2111483
218	1.4	9	13	11	277.1554716
219	1.4	9	13	13	203.1806335
220	1.4	9	13	15	153.2084933
221	1.4	9	15	7	389.7053529
222	1.4	9	15	9	281.7707286
223	1.4	9	15	11	205.2996105
224	1.4	9	15	13	152.364694
225	1.4	9	15	15	152.364694
226	1.4	10	7	7	6000.651628
227	1.4	10	7	9	15080.03872
228	1.4	10	7	11	10387.70829
229	1.4	10	7	13	2887.005689
230	1.4	10	7	15	1534.294451
231	1.4	10	9	7	12486.51786
232	1.4	10	9	9	10916.60755
233	1.4	10	9	11	2818.777151
234	1.4	10	9	13	1442.270426
235	1.4	10	9	15	963.6258006
236	1.4	10	11	7	15703.18932
237	1.4	10	11	9	2944.28862
238	1.4	10	11	11	1432.165975
239	1.4	10	11	13	930.2772621
240	1.4	10	11	15	686.8934448
241	1.4	10	13	7	3327.150507
242	1.4	10	13	9	1423.66741
243	1.4	10	13	11	908.2734812
244	1.4	10	13	13	662.1672702
245	1.4	10	13	15	505.4806707
246	1.4	10	15	7	1543.185252
247	1.4	10	15	9	910.9173802
248	1.4	10	15	11	657.1457437
249	1.4	10	15	13	496.7220752
250	1.4	10	15	15	374.0711132
251	1.5	6	7	7	33.08073182
252	1.5	6	7	9	34.51504508
253	1.5	6	7	11	36.58016454
254	1.5	6	7	13	39.07337324
255	1.5	6	7	15	42.68861041
256	1.5	6	9	7	29.94794906
257	1.5	6	9	9	30.59995162
258	1.5	6	9	11	31.71699121
259	1.5	6	9	13	33.2785869
260	1.5	6	9	15	35.51993005
261	1.5	6	11	7	27.83802848
262	1.5	6	11	9	28.02336217
263	1.5	6	11	11	28.55865267
264	1.5	6	11	13	29.48397401
265	1.5	6	11	15	30.9125642
266	1.5	6	13	7	26.36061102
267	1.5	6	13	9	26.25849543
268	1.5	6	13	11	26.44452233
269	1.5	6	13	13	26.92830006
270	1.5	6	13	15	27.85218305
271	1.5	6	15	7	25.0928785
272	1.5	6	15	9	25.0928785
273	1.5	6	15	11	24.74960588
274	1.5	6	15	13	24.74960588
275	1.5	6	15	15	25.55874547
276	1.5	7	7	7	37.31230209
277	1.5	7	7	9	36.45421941
278	1.5	7	7	11	36.28519216
279	1.5	7	7	13	36.64965403
280	1.5	7	7	15	37.54947525
281	1.5	7	9	7	34.76351208
282	1.5	7	9	9	33.67511193
283	1.5	7	9	11	33.20864151
284	1.5	7	9	13	33.2140822
285	1.5	7	9	15	33.60678711
286	1.5	7	11	7	32.9402633
287	1.5	7	11	9	31.68719946
288	1.5	7	11	11	31.09800489
289	1.5	7	11	13	30.85629086
290	1.5	7	11	15	30.87539615
291	1.5	7	13	7	31.45760546
292	1.5	7	13	9	30.26191281
293	1.5	7	13	11	29.57993907
294	1.5	7	13	13	29.18155496
295	1.5	7	13	15	28.98608286
296	1.5	7	15	7	30.10525186
297	1.5	7	15	9	28.96170725
298	1.5	7	15	11	28.26983414
299	1.5	7	15	13	28.03320145
300	1.5	7	15	15	27.64943439

TABLE C-4

CANDIDATES NUMBER FROM 301 TO 400

No.	d	AR	$h_{rt,t}$	$h_{rt,b}$	t_d
301	1.5	8	7	7	49.96622042
302	1.5	8	7	9	45.84532142
303	1.5	8	7	11	42.96474348
304	1.5	8	7	13	41.18850121
305	1.5	8	7	15	40.04907373
306	1.5	8	9	7	46.02511545
307	1.5	8	9	9	42.35884588
308	1.5	8	9	11	39.81672214
309	1.5	8	9	13	38.18719612
310	1.5	8	9	15	37.08331258
311	1.5	8	11	7	43.00793883
312	1.5	8	11	9	39.70943388
313	1.5	8	11	11	37.36781341
314	1.5	8	11	13	35.78393101
315	1.5	8	11	15	34.85530122
316	1.5	8	13	7	40.36830788
317	1.5	8	13	9	37.75230124
318	1.5	8	13	11	35.58240581
319	1.5	8	13	13	34.10557598
320	1.5	8	13	15	33.06757379
321	1.5	8	15	7	38.40844624
322	1.5	8	15	9	35.79754012
323	1.5	8	15	11	33.94044892
324	1.5	8	15	13	32.65064394
325	1.5	8	15	15	31.83314355
326	1.5	9	7	7	86.90659028
327	1.5	9	7	9	71.61822916
328	1.5	9	7	11	62.51721747
329	1.5	9	7	13	55.95113998
330	1.5	9	7	15	51.65539825
331	1.5	9	9	7	74.16434953
332	1.5	9	9	9	62.94589544
333	1.5	9	9	11	55.64546348
334	1.5	9	9	13	50.62241743
335	1.5	9	9	15	47.0684056
336	1.5	9	11	7	65.53146078
337	1.5	9	11	9	56.67663654
338	1.5	9	11	11	50.88269386
339	1.5	9	11	13	46.60421266
340	1.5	9	11	15	43.60485192
341	1.5	9	13	7	58.6974959
342	1.5	9	13	9	51.63819717
343	1.5	9	13	11	46.83019394
344	1.5	9	13	13	43.51887211
345	1.5	9	13	15	40.94054171
346	1.5	9	15	7	53.52606206
347	1.5	9	15	9	47.99955425
348	1.5	9	15	11	43.7166044
349	1.5	9	15	13	40.77873342
350	1.5	9	15	15	38.71056398
351	1.5	10	7	7	278.1968424
352	1.5	10	7	9	190.642889
353	1.5	10	7	11	140.3137183
354	1.5	10	7	13	108.035315
355	1.5	10	7	15	88.3347304
356	1.5	10	9	7	199.5672572
357	1.5	10	9	9	141.5485897
358	1.5	10	9	11	107.7713467
359	1.5	10	9	13	87.01544151
360	1.5	10	9	15	74.18806653
361	1.5	10	11	7	150.429613
362	1.5	10	11	9	109.9649778
363	1.5	10	11	11	88.09961127
364	1.5	10	11	13	73.90126306
365	1.5	10	11	15	64.26408263
366	1.5	10	13	7	115.1292714
367	1.5	10	13	9	89.31776463
368	1.5	10	13	11	73.91953686
369	1.5	10	13	13	64.1325735
370	1.5	10	13	15	57.12720329
371	1.5	10	15	7	94.35083412
372	1.5	10	15	9	75.39008159
373	1.5	10	15	11	64.33519983
374	1.5	10	15	13	57.25704168
375	1.5	10	15	15	51.75930988
376	1.6	6	7	7	36.72331296
377	1.6	6	7	9	42.24567506
378	1.6	6	7	11	50.22238708
379	1.6	6	7	13	61.82680124
380	1.6	6	7	15	76.99578166
381	1.6	6	9	7	30.61627666
382	1.6	6	9	9	34.0091612
383	1.6	6	9	11	38.96216667
384	1.6	6	9	13	45.54636072
385	1.6	6	9	15	54.00970947
386	1.6	6	11	7	26.67913096
387	1.6	6	11	9	28.72937591
388	1.6	6	11	11	32.05129701
389	1.6	6	11	13	36.22499478
390	1.6	6	11	15	41.51152834
391	1.6	6	13	7	24.36797354
392	1.6	6	13	9	25.58343679
393	1.6	6	13	11	27.54194536
394	1.6	6	13	13	30.22410048
395	1.6	6	13	15	34.01861573
396	1.6	6	15	7	22.85188639
397	1.6	6	15	9	23.71167625
398	1.6	6	15	11	24.7965132
399	1.6	6	15	13	26.61870706
400	1.6	6	15	15	28.99538462

TABLE C-5

CANDIDATES NUMBER FROM 401 TO 500

No.	d	AR	$h_{rt,t}$	$h_{rt,b}$	t_d
401	1.6	7	7	7	34.00448582
402	1.6	7	7	9	36.52286155
403	1.6	7	7	11	40.04887173
404	1.6	7	7	13	45.08231745
405	1.6	7	7	15	52.13951045
406	1.6	7	9	7	30.33047556
407	1.6	7	9	9	31.58338287
408	1.6	7	9	11	33.57050311
409	1.6	7	9	13	36.49392835
410	1.6	7	9	15	40.47786994
411	1.6	7	11	7	28.05246358
412	1.6	7	11	9	28.57802242
413	1.6	7	11	11	29.66784105
414	1.6	7	11	13	31.44635026
415	1.6	7	11	15	33.93165686
416	1.6	7	13	7	26.53288172
417	1.6	7	13	9	26.67725373
418	1.6	7	13	11	27.22949838
419	1.6	7	13	13	28.21749817
420	1.6	7	13	15	29.7836744
421	1.6	7	15	7	25.46858547
422	1.6	7	15	9	25.20851758
423	1.6	7	15	11	25.43179895
424	1.6	7	15	13	26.02937571
425	1.6	7	15	15	27.02618908
426	1.6	8	7	7	35.52523228
427	1.6	8	7	9	35.97884228
428	1.6	8	7	11	37.2325363
429	1.6	8	7	13	38.82195075
430	1.6	8	7	15	41.50965103
431	1.6	8	9	7	33.08085078
432	1.6	8	9	9	32.90071577
433	1.6	8	9	11	33.32557578
434	1.6	8	9	13	34.1431918
435	1.6	8	9	15	35.41179195
436	1.6	8	11	7	31.30312776
437	1.6	8	11	9	30.77432147
438	1.6	8	11	11	30.74932674
439	1.6	8	11	13	31.04282209
440	1.6	8	11	15	31.75326075
441	1.6	8	13	7	30.11217458
442	1.6	8	13	9	29.42672098
443	1.6	8	13	11	29.15677432
444	1.6	8	13	13	29.1458314
445	1.6	8	13	15	29.46676251
446	1.6	8	15	7	28.94033587
447	1.6	8	15	9	28.2603365
448	1.6	8	15	11	28.03763929
449	1.6	8	15	13	27.85124816
450	1.6	8	15	15	27.94261711

No.	d	AR	$h_{rt,t}$	$h_{rt,b}$	t_d
451	1.6	9	7	7	41.04889309
452	1.6	9	7	9	39.40743381
453	1.6	9	7	11	38.61774458
454	1.6	9	7	13	38.55257646
455	1.6	9	7	15	39.03337013
456	1.6	9	9	7	38.65298282
457	1.6	9	9	9	36.88870359
458	1.6	9	9	11	35.95250944
459	1.6	9	9	13	35.56319459
460	1.6	9	9	15	35.59611262
461	1.6	9	11	7	36.85562641
462	1.6	9	11	9	35.111787
463	1.6	9	11	11	34.13471643
464	1.6	9	11	13	33.54215146
465	1.6	9	11	15	33.29378626
467	1.6	9	13	7	35.41686796
468	1.6	9	13	9	33.7530327
469	1.6	9	13	11	32.69737586
470	1.6	9	13	13	32.01045993
471	1.6	9	13	15	31.5987287
472	1.6	9	15	7	34.07641205
473	1.6	9	15	9	32.48670093
473	1.6	9	15	11	31.69481464
474	1.6	9	15	13	30.96392565
475	1.6	9	15	15	30.48495694
476	1.6	10	7	7	52.43257979
477	1.6	10	7	9	48.04893809
478	1.6	10	7	11	45.12549992
479	1.6	10	7	13	43.14860368
480	1.6	10	7	15	41.94397275
481	1.6	10	9	7	48.6898018
482	1.6	10	9	9	44.78601222
483	1.6	10	9	11	42.08502858
484	1.6	10	9	13	40.24897978
485	1.6	10	9	15	39.09732911
486	1.6	10	11	7	45.91791431
487	1.6	10	11	9	42.33545519
488	1.6	10	11	11	39.8767972
489	1.6	10	11	13	38.18336087
490	1.6	10	11	15	37.01220228
491	1.6	10	13	7	43.34860181
492	1.6	10	13	9	40.36269813
493	1.6	10	13	11	38.17128177
494	1.6	10	13	13	36.53559446
495	1.6	10	13	15	35.46933711
496	1.6	10	15	7	41.26419841
497	1.6	10	15	9	38.53160648
498	1.6	10	15	11	36.55346516
499	1.6	10	15	13	35.36459212
500	1.6	10	15	15	34.32029608

TABLE C-6

CANDIDATES NUMBER FROM 501 TO 600

No.	d	AR	$h_{rt,t}$	$h_{rt,b}$	t_d
501	1.7	6	7	7	50.29793736
502	1.7	6	7	9	65.16466721
503	1.7	6	7	11	86.86156437
504	1.7	6	7	13	118.1168847
505	1.7	6	7	15	160.5608643
506	1.7	6	9	7	37.57811637
507	1.7	6	9	9	46.26536517
508	1.7	6	9	11	58.0207732
509	1.7	6	9	13	73.67891051
510	1.7	6	9	15	94.60247872
511	1.7	6	11	7	30.04883588
512	1.7	6	11	9	35.68760961
513	1.7	6	11	11	42.93491894
514	1.7	6	11	13	52.32814009
515	1.7	6	11	15	64.05670897
516	1.7	6	13	7	25.89964367
517	1.7	6	13	9	29.16422848
518	1.7	6	13	11	33.8833429
519	1.7	6	13	13	40.29812655
520	1.7	6	13	15	47.9245268
521	1.7	6	15	7	23.14181159
522	1.7	6	15	9	25.36724483
523	1.7	6	15	11	28.49365165
524	1.7	6	15	13	32.6572217
525	1.7	6	15	15	37.85931534
526	1.7	7	7	7	40.53696052
527	1.7	7	7	9	49.11071147
528	1.7	7	7	11	61.35956436
529	1.7	7	7	13	77.75944065
530	1.7	7	7	15	99.73409423
531	1.7	7	9	7	32.66391542
532	1.7	7	9	9	37.54730049
533	1.7	7	9	11	44.41715672
534	1.7	7	9	13	53.35102209
535	1.7	7	9	15	65.16500819
536	1.7	7	11	7	28.06518113
537	1.7	7	11	9	30.83801017
538	1.7	7	11	11	35.28839196
539	1.7	7	11	13	40.88102056
540	1.7	7	11	15	47.88844886
541	1.7	7	13	7	25.53855388
542	1.7	7	13	9	27.14595293
543	1.7	7	13	11	29.69886329
544	1.7	7	13	13	33.28065262
545	1.7	7	13	15	38.16307548
546	1.7	7	15	7	23.9500586
547	1.7	7	15	9	25.03917021
548	1.7	7	15	11	26.49837413
549	1.7	7	15	13	28.82890275
550	1.7	7	15	15	31.92967857
551	1.7	8	7	7	36.60484792
552	1.7	8	7	9	40.93112917
553	1.7	8	7	11	47.3528606
554	1.7	8	7	13	56.52086809
555	1.7	8	7	15	69.02124217
556	1.7	8	9	7	31.79373568
557	1.7	8	9	9	33.97776969
558	1.7	8	9	11	37.59363802
559	1.7	8	9	13	42.51317591
560	1.7	8	9	15	48.91533772
561	1.7	8	11	7	28.95759862
562	1.7	8	11	9	30.01528543
563	1.7	8	11	11	32.04274427
564	1.7	8	11	13	34.959623
565	1.7	8	11	15	38.90975798
566	1.7	8	13	7	27.33868025
567	1.7	8	13	9	27.77952651
568	1.7	8	13	11	28.88414051
569	1.7	8	13	13	30.66030408
570	1.7	8	13	15	33.14388787
571	1.7	8	15	7	26.10599429
572	1.7	8	15	9	26.34420113
573	1.7	8	15	11	26.90689286
574	1.7	8	15	13	27.78648131
575	1.7	8	15	15	29.37168092
576	1.7	9	7	7	36.2898211
577	1.7	9	7	9	38.10312688
578	1.7	9	7	11	40.80775619
579	1.7	9	7	13	45.00124792
580	1.7	9	7	15	50.86590182
581	1.7	9	9	7	33.26240263
582	1.7	9	9	9	33.85588932
583	1.7	9	9	11	35.13488148
584	1.7	9	9	13	37.32952856
585	1.7	9	9	15	40.46112715
586	1.7	9	11	7	31.41059549
587	1.7	9	11	9	31.4090828
588	1.7	9	11	11	31.9269241
589	1.7	9	11	13	33.02563355
590	1.7	9	11	15	34.83899325
591	1.7	9	13	7	30.0895132
592	1.7	9	13	9	29.77937131
593	1.7	9	13	11	29.86584264
594	1.7	9	13	13	30.41203813
595	1.7	9	13	15	31.45326732
596	1.7	9	15	7	29.24152111
597	1.7	9	15	9	28.72857876
598	1.7	9	15	11	28.57878701
599	1.7	9	15	13	28.79414643
600	1.7	9	15	15	29.39158033

TABLE C-7

CANDIDATES NUMBER FROM 601 TO 625

No.	d	AR	$h_{rt,t}$	$h_{rt,b}$	t_d
601	1.7	10	7	7	38.95698403
602	1.7	10	7	9	38.81398627
603	1.7	10	7	11	39.59615191
604	1.7	10	7	13	40.98563604
605	1.7	10	7	15	43.08854856
606	1.7	10	9	7	36.63950052
607	1.7	10	9	9	35.87737711
608	1.7	10	9	11	35.85030716
609	1.7	10	9	13	36.32848995
610	1.7	10	9	15	37.41119989
611	1.7	10	11	7	35.05278729
612	1.7	10	11	9	34.08608176
613	1.7	10	11	11	33.70868855
614	1.7	10	11	13	33.73455322
615	1.7	10	11	15	34.14349172
616	1.7	10	13	7	33.83499536
617	1.7	10	13	9	32.75723417
618	1.7	10	13	11	32.20248352
619	1.7	10	13	13	31.964196
620	1.7	10	13	15	32.06229813
621	1.7	10	15	7	32.93103838
622	1.7	10	15	9	31.86114263
623	1.7	10	15	11	31.18764417
624	1.7	10	15	13	30.84112453
625	1.7	10	15	15	30.71426154

Note that the results are obtained by simulating a total of 625 design candidates using CFD. In this design space, the input domains are the diameter, aspect ratio, top heater height, and bottom heater height, and the output domain is the doubling time.

(This page is intentionally left blank)

APPENDIX E. ANN-ASSISTED OPTIMIZATION CODES

The codes are developed using MATLAB to implement training surrogate models and optimization. The flowchart is adopted based on the process established in Chapter 6.6.

<surroRun.m>

```
%% Initialization
clc
clear
close all

% parpool(4)

% Surrogate function Creation: 0 - no, 1 - yes
fc = 1;
% Reference doubling time for data elimination
tc = 200;
% Number of neurons per layer
nNodes = [4 8 12 16];
% Number of hidden layers
nHL = 2;

%% Load Data
load('DataTdbNew.mat');
% load('DataTdbnew7.mat');

%% Chop Data
CC = [DataTdb(:,1:2),DataTdb(:,4:6)];
[~, CC_elim, ~, ~, c] = chopdata2(CC, tc, 5);

inputs = CC_elim(:,1:4)';
output = CC_elim(:,5)';

%% Build Surrogate Model
tol1 = 5;
tol2 = .99;
wp =.18;
hp =.18*4;
woffset = wp*1.4;
firstloc = [.05 .15 wp hp];

n = 0; m = 0; brk = 0;
while (1)
    % Number of retraining set
    n = n + 1;

    for i = 1:length(nNodes)
        m = m + 1;

        % Network Training Function
        [net{m},tr{m},r(m),output,y{m},a(m),b(m)] =
surroModel(inputs,output,nHL,nNodes(i)); hold on
```

```
        % Performance
        P(m) = tr{m}.best_perf;
        PE(m) = abs(tr{m}.best_perf-P(m))+abs(tr{m}.best_tperf-P(m));

        if (fc == 1)
            fnc =
['NN',num2str(tc),'_',num2str(c),'_nHL',num2str(nHL),'_nND',num2str(nNodes(i
)')];
            genFunction(net{m},fnc,'MatrixOnly','yes');
            obj = str2func(fnc);
        end

        % Upper/Lower bounds
        xlb = [1.3,6,7,7];
        xub = [1.7,10,15,15];

        % Optimization Options
        option = optimset('display','iter');
        option.FunctionTolerance = 1e-6;
        options.ConstraintTolerance = 1e-6;
        option.PopulationSize=200;

        % Hybrid Algorithm
        [x_ga, f_ga] = ga(@(x) obj(x'), 4,
[],[],[],[],xlb,xub,@constraints,option);
        [xopt, fopt] = fmincon(@(x) obj(x'), x_ga,
[],[],[],[],xlb,xub,@constraints,option);

        % Calculate Reactor Volume
        vol = volumePCR(xopt);

        Height = xopt(1)*xopt(2);

        if fopt < 22
            brk = 1;
            break
        end

    end

    if brk == 1
        break
    end

end


%% Plot
figure('pos',[500 500 400 400],'Name',['# of Retraining: ', num2str(n-
1)],'NumberTitle','off')
% regPlot(output,y{idx},r(idx),a(idx),b(idx), nNodes(i))
regPlot(output,y{m},r(m),a(m),b(m), nNodes(i))

figure
plotperform(tr{m})
```

<surroModel.m>

```
function [net,tr,r,output,y,a,b] = surroModel(inputs,output,nHL,nNodes)

%% Neural Network Setting
net = feedforwardnet;
net.numLayers = nHL+1;
net.trainParam.showWindow = true;
net.trainFcn = 'trainbr';%'trainbfg';%'traincgf';%'trainbfg';%'trainbr';
net.layerConnect = zeros(net.numLayers);
net.divideParam.trainRatio = 80/100;
net.divideParam.valRatio = 10/100;
net.divideParam.testRatio = 10/100;
net.trainParam.epochs = 1000;
net.performFcn = 'mse';
net.trainParam.max_fail = 1000;
net.trainParam.goal = 2e-5;

be = [1 1 1];
net.layerConnect(3,1) = 0;

%% Hidden Layers
for j = 1: net.numLayers -1
    if (j ~= 1)
        net.layerConnect(j,j-1) = 1;
    end
    net.layers{j}.size = nNodes;                          % Neuron Size (# of
Nodes)
    net.layers{j}.name = ['Hidden Layer ',num2str(j)];  % Layer Name
    net.layers{j}.transferFcn =
'tansig';%'elliotsig';%'tansig';                          % Transfer Function
Type
    net.layers{j}.initFcn = 'initnw';
    net.biasConnect(j,1) = be(j);
    if (j == 1)
        net.inputConnect(j,1) = 1;
    else
        net.inputConnect(j,1) = 0;
    end
    net.outputConnect(j) = 0;
end

%% Output Layer
net.layerConnect(end,end-1) = 1;
net.layers[75].name = 'Output Layer';
net.layers[75].size = 1;
net.layers[75].transferFcn = 'purelin';
net.layers[75].initFcn = 'initwb'; %'initnw';
net.outputConnect(end) = 1;
net.biasConnect(end,1) = 0;

net = configure(net, inputs, output);
[net, tr] = train(net,inputs,output,'useParallel','yes');
y = net(inputs);
[r,a,b] = regression(output,y);
end
```

<regPlot.m>

```
function regPlot(Output,y,r,a,b, nNodes)

plot(Output,y,'Ok')
hold on
plot([min(Output):max(Output)],[min(Output):max(Output)],':k','LineWidth',1)
hold on
plot([min(Output),max(Output)],a*([min(Output),max(Output)]) + b,'-
b','LineWidth',2)
axis square
axis([min(Output) max(Output) min(Output) max(Output)])
xlabel ('Target: Doubling Time [s]', 'FontWeight','bold')
ylabel (['Output~=',num2str(a),'*Target+',num2str(b)], 'FontWeight','bold');
title (['R^2: ',num2str(r), ', ',' # Neurons: ', num2str(nNodes)],
'FontWeight','bold')
legend('Data','Fit','T=Y','location','northwest')

end
```

VITA

EDUCATION

Ph.D., Aerospace Engineering, Old Dominion University, USA, Aug 2019
Concentrations: Computational Fluid Dynamics; Optimization; Neural Network
Projects: Convective PCR Reactor Design Optimization; Multiphase Flow for Collagen Threads

M.S., Aerospace Engineering, Konkuk University, South Korea, Feb 2014
Concentrations: Multidisciplinary Design Optimization; Aerodynamics; CAE Automation
Projects: UAV resizing optimization; Helicopter Rotor Design; Space Launch Vehicle Design
Thesis: Uncertainty-based Logical Mission Design Method for Space Launch Vehicles

B.S., Aerospace Engineering, Inha University, South Korea, Feb 2011
Area of Interest: Aerodynamics; Aircraft Design

PUBLICATIONS

[1] Qiu, X., **Shu, J**., Baysal, O., Wu, J., Qian, S., Ge, S., Li, K., Ye, X., Xia, N., and Yu, D., "Real-Time Capillary Convective PCR based on Horizontal Thermal Convection", Microfluidics Nanofluidics, Vol. 23, No. 3, p.39, 2019 (https://doi.org/10.1007/s10404-019-2207-0, IF 2.437)

[2] **Shu**, **J.**, Baysal, O., Qian, S., Fuhao, W., and Qiu, X., "Performance of Convective Polymerase Chain Reaction by Doubling Time", International Journal of Heat and Mass Transfer, Vol 133, pp. 1230-1239, 2019 (https://doi.org/10.1016/j.ijheatmasstransfer.2018.12.179, IF 4.346)

[3] **Shu**, **J.**, Kim, J., Lee, J., and Kim, S., "Multidisciplinary Design Optimization for Space Launch Vehicles based on Sequential Design Process", Proceedings of the Institution of Mechanical Engineers, Part G: Journal of Aerospace Engineering, Vol 203, No. 1, pp. 3-18, 2016 (https://doi.org/10.1177/0954410015586858, IF 1.104)

[4] Vu, N. A., Lee, J., and **Shu**, **J.**, "Aerodynamic Design Optimization of Helicopter Rotor Blades including Airfoil Shape for Hover Performance", Chinese Journal of Aeronautics, Vol 26, No. 1, pp. 1-8, 2013 (https://doi.org/10.1016/j.cja.2012.12.008, IF 2.095)

[5] Kim, J., Van, N. N., **Shu**, **J.**, Maxim, T., Lee, J., and Kim, S., "UAV Performance Improvement Using Integrated Analysis and Design Optimization Technology", Journal of the Korean Society for Aviation & Aeronautics, Vol. 21, No. 1, pp. 30-38, 2013 (In Korean). (http://dx.doi.org/10.12985/ksaa.2013.21.1.030, IF 0.173)

[6] **Shu**, **J.**, Baysal, O., Qian, S., and Qiu, X., "Computational Design of a Single Heater Convective-PCR for Point-of-Care", Journal of Medical Devices, August 2019 **(Accepted)**

[7] Kote, V., **Shu**, **J.**, and Baysal, O., "Unsupervised-Learning Assisted Artificial Neural Network for Convective PCR Device Optimization", SN Computer Science, April 2019 **(Under Review)**

[8] **Shu**, **J.**, "Multi-Stage Liquid Rocket Weight Estimation and Optimization for Early Stage of Design", Proceedings of the institution of Mechanical Engineers, Part G: Journal of Aerospace Engineering, April 2019 **(Under Review)**